



Thesis Thesis for Master of Science in Applied Physics

Albert-Ludwigs-Universität Freiburg

Faculty of Physics

Single Shot electron velocity imaging and ion Time of flight measuments of He and Ne clusters under strong Mid-Infrared laser field.

Presented by Cristian Enrique Medina Hernandez

Date 12. Augost 2019

Referent Prof. Dr. Marcel Mudrich and Prof. Dr. Frank Stinkermeier

Abstract

In this thesis a new data acquisition method is explained for correlate single shot VMI-TOF measurements on doped Helium and Neon droplets ionized by a MIR femtosecond laser. Until now, VMI images have been always treated in a statistical way. With our method we analyzed electron velocity map images for single coulomb explosion of He and Ne clusters under strong MIR fields. We analyzed the maximal kinetic energy distribution that shows a strong dependency to the collected number of electrons and at certain conditions it can be modeled as a homogeneously charge spherical electronic cloud, where the electron in the perimeter of the sphere will determine the maximal kinetic energy in the explosion. This thesis, present the measurements and comparison of different noble gases under Mid and near-Infrared laser pulses doped with Xe, non, Calcium, Argon and water.

We demonstrate that exist a laser intensity threshold necessary to start an optimal coulomb explosion. Moreover, the efficiency of the plasma formation present a strong relation to the cluster size and the doping level. On one hand, the smallest droplets were more difficult to ignite, On the other hand, there exist an optimum doping level to efficiently start the plasma formation independent of the dopant element. Furthermore, the laser pulse duration on contrary to the laser intensity, shows an important role in the ignition of the smaller droplets, while the total intensity decrease with the pulses length, at more duration it increase the signal counts autonomously the power, meaning that the number of cycles interacting with the the ionized electrons at the beginning of the process are fundamental to the plasma formation. The cluster element didn't show to have an important function in the plasma creation other than characterize the cluster size, same for the clusters doped with just one single dopant element. On contrary, when we used a combination on Xenon and Calcium, it was clear that exist an optimum mix of atoms where the replacement of a few Xe atom for Ca improve the signal count up to the double.

Contents

0.1	Introduction	6
1	Theoretical Background	8
1.1	Helium Nanodroplets	8
1.1.1	General properties of Helium	9
1.1.1.1	Helium Droplets	9
1.1.1.2	Composite Clusters	14
1.1.1.3	Composite Clusters	14
1.2	Neon Nanodroplets	16
1.3	Cluster-Intense Fields Interaction	17
1.3.1	PhotoIonization for single atoms	18
1.3.2	Multiphoton and Tunneling Ionization	20
1.3.3	Keldish Theory	22
1.3.4	Ponderomotive energy	23
1.3.5	Cluster Ionization	24
1.3.5.1	Cluster expansion	26
1.4	VMI spectrometer	28
1.4.1	Velocity distribution in VMI	28
2	Experimental setup	31
2.1	Source chamber	31
2.2	Doping chamber	33
2.3	Detection chamber	35
2.3.1	Velocity map imaging VMI	35
2.4	Time of flight spectrometer	36
2.5	Lt detector	38
3	Acquisition and calibration methods.	39
3.1	Camera and trigger protocol	39
3.2	Calibration methods	42
3.2.1	VMI calibration	42

3.2.2	Laser intensity calibration	44
3.3	Data Analysis	45
3.3.1	Event Recognition	45
3.4	Coulomb Explosion Model	49
3.4.1	The Islam et al. Model	49
4	Results and Discussion	52
4.1	Helium nanplasma under NIR Fields	53
4.1.1	NIR. He Droplet Intensity scan.	55
4.1.2	NIR. He Droplet size dependant.	57
4.2	Helium nanplasma under MIR Fields	59
4.2.1	MIR. Helium Droplet size dependence.	60
4.2.2	MIR. Helium-Argon doped.	63
4.2.3	MIR. Helium-Water scan.	64
4.2.4	MIR. Helium-Water Intensity scan.	66
4.2.5	MIR. Helium Pulse duration dependency	69
4.2.6	MIR. Helium-Xenon-Calcium doping scan	70
4.3	Neon nanplasma under Mid-Infrared	75
4.3.1	MIR. Neon-Xenon doping scan	76
4.3.2	MIR. Neon cluster size scan	78
4.3.3	MIR. Neon pulse scan	80
5	Bibliography	87

List of abbreviations

ATI	above threshold ionization
BSI	barrier suppression ionization
CCD	Charge-coupled Device
CPA	Chirp Pulse Amplification
CWL	Central wavelength
EM	Electro Mechanics
LASER	Light Amplification by Stimulated Emission of Radiation
LT	Langmuir-Taylor
MCP	Micro Channel Plate
NIR	Near Infrared
pBASEX	polar Basis Set Expansion
PID	Proportional – Integral – Derivative
TBR	Three Body Recombination
TOF	Time of flight
VMI	Velocity Map Imaging
VUV	vacuum ultra violet
XUV	Extreme ultraviolet

0.1 Introduction

Physicists always have been fascinated to explain and resolve dynamic processes in short leaps of time of times and to characterize in a time scale fast processes with highly physical interest. Describing these systems requires to acquire data in brief time windows, for example, a film is only a consecutive sequence of photographs that recreate a large time laps in a smaller time scale. For atomic physics, we are talking about a micro-cosmos that can go down to attoseconds. Experiments in attoscience have given up to Nobel prizes, for example Ahmed Zewail in 1999, who demonstrated that femtosecond pulses allow a temporally resolved observation of ion movements in molecules [78].

The duration of the dynamics of a system is related directly to its energy and its quantum states, in other words, to its size. For example, to explore ion dynamics in molecules, times can fluctuate between femtoseconds to nanoseconds [28] and energies up to several electron volt eV. Furthermore, for smallest system as the relaxation of an inner shell vacancy [16] or the process of tunneling ionization [71] occur in attosecond regime, with energies that varies typically on the milielectronvolt scale (meV) for its energy levels. And further, for processes as nuclear fission and quasifission are predicted to unfold even faster, typically on a zeptosecond time scale [57].

To study ultra-short-dynamics, physicist have been challenged to create detector systems based on the interaction light-matter. Along the last decades, experimental schemes have been devised developing new light sources, as for example the laser, to interact with the microcosms. Nowadays, laser pulses can reach up to extreme non-linear optical processes, producing single isolated pulse of ultraviolet(UV) waves as short as 67 as [79]. Such fast pulses open up the possibility of time resolved measurements for short processes like nuclear dynamics, the generation of high energetic electrons and ions in the KeV-regime [22], as well as intensive XUV and attosecond pulse experiments [63]. Not just the pulse duration has been improved within the years, but also the energies that the pulse can deliver, laser pulses with intensities up to 10^{21} W/cm² are available commercially [51].

Femtosecond and attosecond lasers pulses are a milestone in the control and ignition of atomic processes. These advances have enabled the development of new research areas, as well as the investigation of ultrafast dynamics of highly excited matter on a nanometer scale. In particular, many studies have been published in recent years on atomic and molecular clusters that investigate their interaction with NIR, UV or XUV pulses [63]. These are motivated by a broad spectrum of possible applications such as the generation of energetic electrons and ions in the keV

regime [22].

In this thesis, we focus our efforts on the ionization processes by Near-Infrared (NIR) and Mid Infrared (MIR) femtosecond pulse in doped noble gases clusters. The interaction of the dopant with the laser field results in an energy transfer to the cluster that starts an ionization process, known as a nanoplasma. The oscillation of the electrons driven by the laser field inside the clusters creates an energy transfer that ionize the cluster atoms [22]. This process, caused predominantly by electron impact ionization, makes an avalanche-like ionization of the atoms in the cluster, leading to a heating of the plasma and, as a result, a hydrodynamic expansion and Coulomb explosion. Here, we studied the electrons and ion's resulting from the coulomb explosion using a velocity map imaging and a Time of flight spectrometer set in parallel to acquire the data and reconstruct the initial energy configuration of the plasma.

In the First chapter, we will present a brief introduction to the Helium and Neon cluster generation, a short explanation of the ionization process and the basic background for the plasma formation and coulomb explosion process. In the second chapter, we show a detailed explanation of the setup used, explaining from the creation of the Helium droplets process to its detection, describing as well the doping and ignition process. Finally, a detailed explanation of the correlation method for the VMI-TOF measurements is done, showing the set-up of the data acquisition and its advantages. In the third chapter, we discuss the acquisition method and the calibration methods used in the experiment as well as a brief explanation of the analytical model for the coulomb explosion, followed by the description of the data analysis method. Finally on the four chapter, we present the results and its analysis followed by a summary and outcome of the experiments as well as the inputs for future works to improve the results.

1 Theoretical Background

In this chapter we will present all the theoretical background necessary for the development of this project, from the creation and behavior of the Helium and Neon droplets to the theory of the plasma formation and the coulomb explosion processes. In order to guide the reader in an organized way, the sections are organized in the same order the experiment is performed.

1.1 Helium Nanodroplets

The combination of cryogenic matrix isolation, discovered in 1954 [74], and the now well-defined properties of helium (He), especially its superfluidity phase discovered in 1937 by *Kapitza et al* [37], gives as a consequence, an excellent molecular matrix like the helium nanodroplets. Helium has unique properties that make it a perfect source for the nanophysics experiments. For example, it has any optical transitions in the entire infrared and visible regime. In addition, helium clusters are able to pick up atoms and molecules that form different complexes of the species embedded in the interior or the surfaces of the droplet, acting as an ideal matrix for spectroscopy of atoms and molecules. [64] [70].

The size of a Helium cluster can be up to 10^8 atoms, and reach the ultra-cold temperature regime (close to 0.37 K [69]) [18]. Two main advantages of this cooling properties arise. First, dopants in the helium nanodroplet are set to their absolute vibronic ground states, avoiding other possible spectra and establishing the cluster in a specific state. Second, the fast cooling helps in the formation of isomers that are difficult or impossible to generate with other methods [52]. Third, because the superfluid phase of the helium [26], the bond between dopants and helium is weak. Therefore, in contrast to spectroscopy in other matrices with higher temperatures, the optical transitions of many dopants are barely influenced by the helium matrix [70]. The theory of He super fluidity will not be part of this section, this information is well documented in other sources, and here we are based on ref. [18] where all theory is well presented to the reader. In the next section we will dedicate a bigger effort to explain the theoretical and technical background of the helium nanodroplets

creation as well as the physical and technical process to dope it.

1.1.1 General properties of Helium

At room temperature, helium is a light inert gas. It is odorless, colorless, tasteless, and after hydrogen, the second most abundant element in the universe. [18]. It has a simple 2 atoms structure, exhibiting numerous exotic phenomena whose theoretical descriptions are rather complex in many cases, i.e it characteristics of a quantum fluid. From helium exist two stable isotopes 3He and 4He . 4He has two electrons, two protons and two neutrons, no nuclear spin and no total spin, pertaining to the bosonic family, while 3He with only one neutron has a spin of $I = 1/2$ and belongs to the fermions [4].

The bosonic state 4He is especially of interest, at temperature $T \leq 2.8K$ and under normal pressure has a phase transition from "normal liquid" $He - I$ to super liquid $He - II$ [66], in which the helium can be described by a Bose-Einstein condensation. Even the fermionic 3He exhibits this phase transition at $T \leq 0.03K$ [31].

The superfluidity of helium two (He-II), at temperatures close to absolute zero, brings with it some unique features. The essential Properties for this include an almost disappearing viscosity in the superfluid phase, weak interaction, very efficient cooling, and the transparency for electromagnetic radiation up to wavelengths in vacuum ultraviolet (VUV) Spectral range [18]. Helium has therefore in the complete visible spectrum no transitions from the ground state. Through the noble gas configuration, helium has a spherically symmetrical electron distribution [45], it can hardly be polarized and is the least reactive of all the elements.

1.1.1.1 Helium Droplets

The production of Helium droplets had to overcome first one principal problem, its condensation. At the end of the 19th century, many noble gases were liquefied for the first time by applying pressure at room temperature. However, for helium and hydrogen, this method was not successful. In 1922 Kamerlingh Onnes reached temperatures below 1 K by reducing the vapor pressure above liquid helium to about $2 * 10^{-5}$ bar with a series of pumps [13]. The Joule–Thomson effect [73] was the responsible for Onnes experiment to reach this low temperature. The basic idea is that under suitable conditions an expanding gas performs work against its internal forces, for example, when a gas is expanded through a small nozzle thermally isolated from its surroundings. The expansion under these conditions takes place at constant enthalpy, since the expansion nozzle performs none work. It follows the next relation.

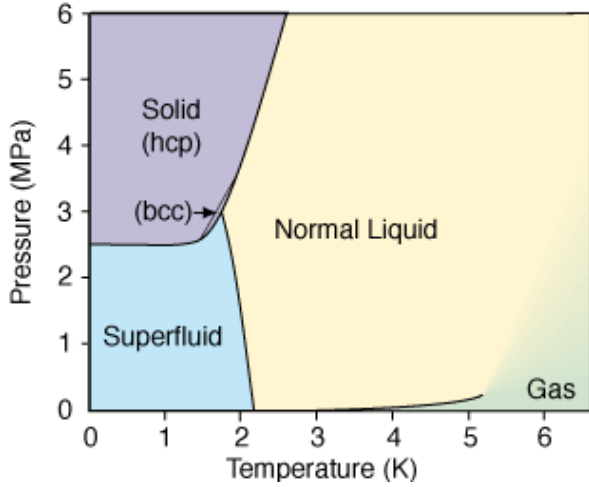


Figure 1.1: 4He Phase transition at Ultra cold temperatures. 4He is the more common isotope of helium. It remains liquid at zero temperature if the pressure is below 2.5 MPa . The liquid has a phase transition to a superfluid phase, also known as Helium-II, at the temperature of 2.17 K (at vapor pressure). Taken from [1]

$$W = H_1 - H_2 = (U_1 + p_1 V_1) - (U_2 + p_2 V_2) \quad (1.1)$$

Where H is the enthalpy before and after, $U = \frac{3}{2}Nk_bT$ is the internal energy, and follows the ideal gases law $pV = Nk_bT$ [18]. Under Joule–Thomson effect conditions, $W = 0$ so $H_1 = H_2$, this expansion leads to a cooling or a warming, bank on the conditions it becomes supersaturated. As a result, condensation takes place and a beam of clusters is formed.

Helium nanodroplets are typically produced by a continuous or pulsed adiabatic expansion of pre cooled gas through a small aperture from a reservoir into a vacuum [64]. In this process a droplet jet is formed, and its characteristics (blasting speeds and size distribution) can be changed due to the manipulation of the setup. For example, pressure differential between the reservoir and the vacuum chamber (usually in the range of a few to 10 MPa), the nozzle temperature (from a few K to $T \leq 40\text{ K}$) or the nozzle size (with pinholes of diameter rounding $5 - 20\mu\text{m}$).

When the Helium expands after the nozzle, its potential energy alters to kinetic energy in a supersonic flow field. After the expansion into the vacuum, the gas becomes supersaturated and condensation occurs, creating the beam cluster. These clusters are made of atoms or molecules, held together by Van der Waals forces, in this case He-He interaction, that share the same kinetic vector. This means that, the two particles travel as close and parallel to each other so bonding is possible as shown in Fig 1.3. From the reference frame of the cluster, each of its molecules is

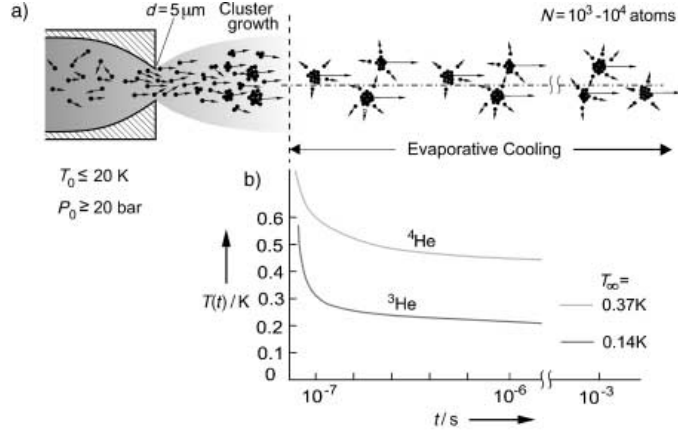


Figure 1.2: a) Schematic representation of the processes leading to the formation and subsequent cooling of Helium droplets in a gas expansion. b) Calculated dependence of the droplet temperature on time for ${}^4\text{He}$ and ${}^3\text{He}$ droplets after they have left the cluster, taken from [7]

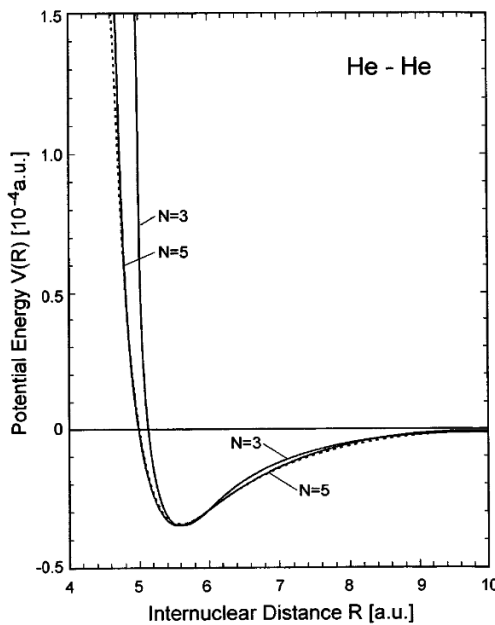


Figure 1.3: Van der Waals potential for He-He interaction. Taken from [7]

close to zero movements, in Helium this enhance the conditions to be liquid and in consequence, superfluidity is achieved [29].

Depending on the buffer gas used, the mechanisms for cluster formation in the supersonic expansion range as a condensation either from the gas phase or the liquid phase. In case the expansion is isentropic (adiabatic and reversible), the expansion is represented by a vertical line in this diagram. Clusters formed by condensation from the gas phase occur when the expansion crosses into the two-phase region on the right-hand side of the critical point. Clusters formed by fragmentation of the liquid

phase occur when the expansion crosses into the two-phase region on the left hand side of the critical point. The diagram is an example of three gases, He, Ar and H₂ at different pressures ($p' = P/P_{critical}$) [40]. The curves represent the regions where the supersonic expansion is possible and the temperatures (in Fig dimensionless) that each gas should have in order to achieve clustering and cooling [40].

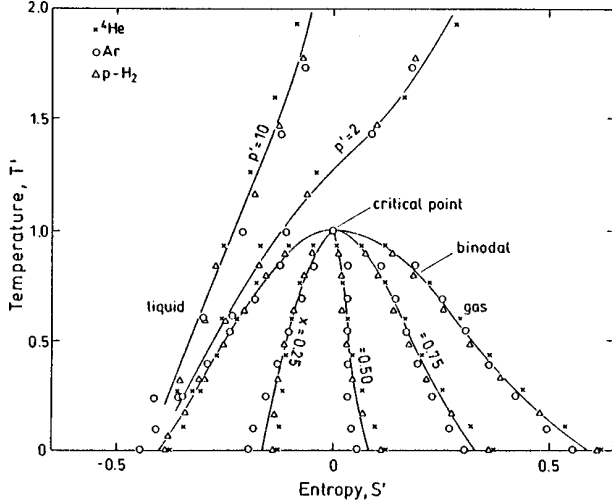


Figure 1.4: Dimensionless phase diagram for He, H₂ and Ar. Where T is dimensionless $T' = (T - T_{tp})/(T_{cr} - T_{tp})$, same as entropy $S' = (S - S_{cr})/\Delta S_{tp}$ and x is the fraction of the fluid in the gaseous phase, where the subscripts *cr* and *tp* refer to the critical point and triple point respectively, and ΔS is the entropy change for vaporization. The curves are drawn as guides to the eye, not exact measurements, taken from [40].

There is no mathematical approach of the physics behind this supersonic expansion but usually, Raleigh scattering measurements in combination with an empirical scaling law [29] are used to estimate the mean cluster size, assuming a certain degree of control over the cluster size distribution by adjusting the nozzle width and the source pressure. The droplet size distribution during supersonic expansion in the follows a log-normal distribution of the form [32].

$$p(N) = \frac{1}{\sqrt{2\pi}N\sigma} \exp\left[-\frac{(\ln(N/N_0))^2}{2\sigma^2}\right] \quad (1.2)$$

Where N is the number of atom in the cluster, σ is the distribution width and N_0 is the most likely numbers of atoms. Following it give a mean value.

$$\bar{N} = \exp\left(\mu + \frac{\sigma^2}{2}\right) \quad (1.3)$$

With a half width maxima of [32]

$$\sigma N_{\frac{1}{2}} = \exp \left(\mu - \sigma^2 + \sigma \sqrt{2 \ln(2)} \right) - \exp \left(\mu - \sigma^2 - \sigma \sqrt{2 \ln(2)} \right) \quad (1.4)$$

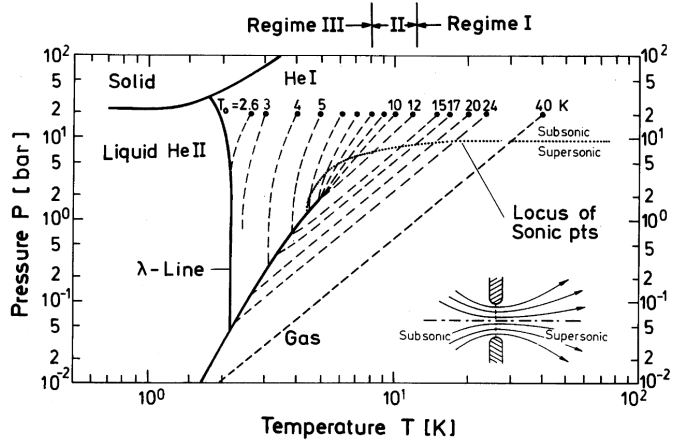


Figure 1.5: Expansion regimes. ${}^4\text{He}$ Pressure-Temperature phase diagram for Nozzle beam expansions starting at a backing pressure of 20 bar and a temperature. As discussed, qualitatively different behaviors are shown for the regime I-II and II where starting in the gas phase, near the phase transition respectively. Taken from [9].

As shown in Figure ??, the initial gas conditions (pressure, temperature and nozzle size) in the free expansion phase will determine the characteristics of the final helium beam. From here, three main regimes can be defined.

Regime I or sub-critical expansion, begins in the gas phase and leads to droplet formation via condensation. This is the case of most expansions since the pressure is located below the critical pressure P_c . Regime II, also called as critical expansion, is a long-winded regime that includes all trajectories which are near the critical point, leading to random expansion and difficult control of the beam due to the large fluctuations in density. Regime III, the super-critical expansion, starts at low temperatures where the helium stops behaving as an ideal gas, expecting flashing or cavitation breaking up the liquid drops jet. [9]

super-critical and sub-critical regimes have been studied in the last several years and are clearly identified in the resulting size distributions. Figure ?? shows that super-critical expansion forms large droplets (usually between 20–100 nm diameter) while a sub-critical expansion is suited to generate small droplets (around 5–10 nm). A simple relation that can be done to calculate the size or number of atoms in a Custer is using.

$$r = N_{1/3} * \rho A \quad (1.5)$$

Where r is the radius of the beam, and ρ its density, in this case, for helium $\rho = 0.0022 \text{ g/cm}^3$ [65], but this approximation is not exact due the variation in He density at this temperature. As expected in both regimens, for creating larger helium nano droplets, higher He pressure and lower nozzle temperature are used. For our experiment a $5\mu\text{m}$ nozzle was used at temperatures oscillating between $11 - 20\text{K}$, and backing pressures of 30, 45 and 50 bar.

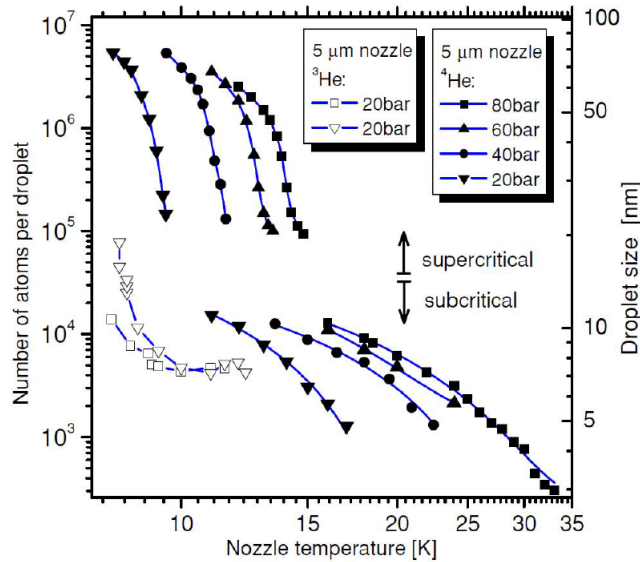


Figure 1.6: Sizes of the ${}^4\text{He}$ droplets as a function of nozzle temperature T and pressures, based on [69], using a $5\mu\text{m}$ nozzle. The sub and super critical regimes are clearly differentiated. Taken from [64]

1.1.1.2 Composite Clusters

1.1.1.3 Composite Clusters

We can define a composite cluster or doped cluster, as an atomic lump that contains one or more different atomic elements. The main interesting properties in non-doped clusters are usually set as a function of its size, but for doped clusters, the interaction between the elements creates new degrees of freedom that makes more complex its behavior. For example, the new composite will have different structural properties due the spatial distribution of the species. Hence, composite clusters exhibit a more diverse behavior and offer more opportunities to study different characteristics of the material.

The difficult problem to overcome in composite cluster is how to create them. Two techniques can be used. The first one, is the co-expansion of a previously

mixed gas [67]. The second one is to produce a first cluster and then cross it with an atomic beam of the doping species.

The first technique involves several technical problems, depends on possible interactions between the elements, the condensation ranges of the bulks and even in the affinity of the materials. One of the most used techniques, and the one used in this study is the one called pick-up technique [25]. The idea is simple, as well as a snowball on its way downhill collects or pick-up more snow. The helium cluster, after being directional selected through a skimmer, passes through a doping cell full of a dopant gas at low densities ($10 - 2\text{Pa}$) [64]. As a result, the gas atoms that are along the droplet cross sections will be captured by the beam and travel with it. The probability for Helium droplets to collect k atoms or molecules via inelastic collisions depends on the length of the oven cell l , the cross section of the droplets σ , and the particle density inside the cell n . As l and σ remains constant, varying the density in the doping cell can regulate the abundance of k , following Poissonian statistics.

$$P_k(l, n, \sigma) = \frac{(ln\sigma)^k}{k!} e^{(-ln\sigma)} \quad (1.6)$$

Two important properties of these relations can be deduced. First, the maxima of different cluster sizes are equidistant, $n_{max} = \frac{k}{l\sigma}$ and second, the exponential function in the equation becomes nearly one for small particle densities [8].

Every pick-up process leads to an energy transfer to the droplets. As the dopant rapidly cools down, that means an energy transfer to the Helium, causes an evaporation of some He atoms to keep the temperature unchanged in the cluster. This Helium evaporation or "shrinkage", leads to a decrease in the cross section of the droplet and the probability to collect further particle. At a certain energy entry, the complete droplet evaporates if to many dopants access to it. With the average kinetic energy E_{kin} , and E_{in} the internal. The involved energy is composed of the following contributions [8].

$$E = \langle E_{kin} \rangle + E_{in} + E_{binding} + E_{cluster} \quad (1.7)$$

Where

$$\langle E_{kin} \rangle \approx \frac{3}{2}k_bT + \frac{1}{2}mv^2 \quad (1.8)$$

Is the final kinetic energy of the droplet depending on it mass, velocity and temperature in the gas cell.

Several studies have focused on the $E_{binding}$ with ${}^4\text{He}$, so the energy binding for a

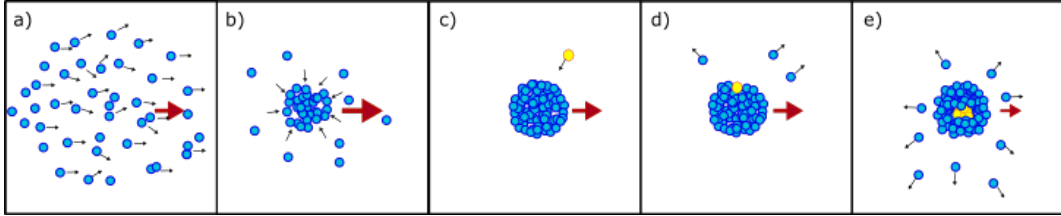


Figure 1.7: Animation of the Helium creation, doping and evaporation. From left to right, we see the Helium droplet production; after being released by the supersonic jet, the Cluster formation, the pickup process of the dopant and finally the Helium shrinking process.

broad number of materials is known. It is also important to take into account that the binding energy includes the cluster-dopant binding as well as the dopant-dopant relation. [69]. The energy bounding for example of Xe-He is around 26.9 meV [44], or He-H₂O is about 0.1 eV [45].

1.2 Neon Nanodroplets

Neon (Ne) is the second lightest inert gas with atomic number 10, it has 3 stable isotopes in nature, the ²⁰Ne with more than 90% of abundance, followed by ²¹Ne and ²²Ne [49]. At extreme temperature, Neon is solid as shown in the graphic 1.8 and its triple point is around $T_p = 24\text{K}$ [77]. Neon is a noble gas, it shares most of the properties already mentioned from Helium, except for its superfluidity. It has a quite large ionization potential for its first electron at $I_p = 21.56\text{ eV}$, what makes quite suitable to use it as a matrix with strong fields lasers, because at low intensities, it will not interact with the light source, so dopants can be carried out in a non-interactive way.

Ne cluster has been proved to provide an ideal medium for chemical reactions as solvation effect and heterogeneous chemistry at a microscopic level [25]. With a properly regulated pick-up system the reactants are deposited in a controlled way in the cluster and it becomes a nanoreactor equivalent [24].

The conditions for creating Neon clusters are quite similar to the ones explained above, also well explained in the famous Haga law [30]. Several studies have been realized on the characterization of Ne clusters, for example by *R. Von Pietrowski et al* [53] who studied the Electronic excitations of Xe atoms and Xe₂ molecules embedded in free Ne clusters. On contrary to helium, is important to work with neon clusters at temperatures and pressures far from its solidification point. At extreme low temperatures, small differences in pressure leads to big size changes on the clusters, the higher the pressure in the nozzle the bigger the droplets. As an

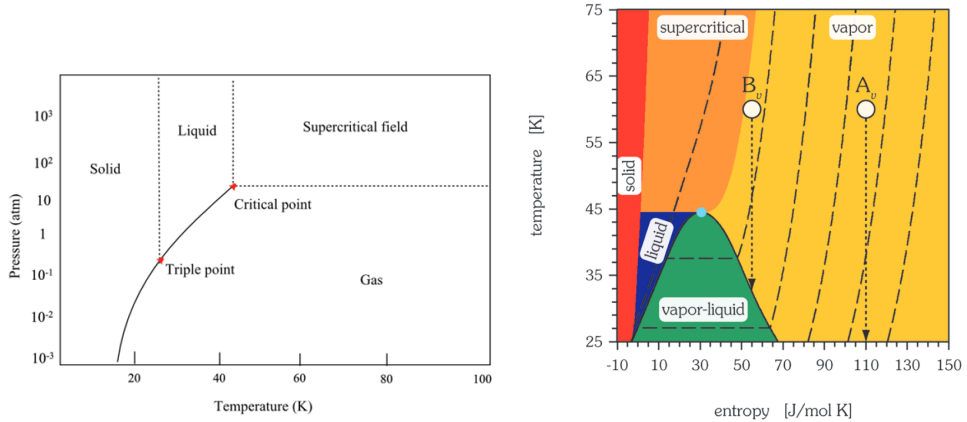


Figure 1.8: On the left, Neon phase diagram. taken from [77], on the right, $T - S$ phase diagram of Ne. The critical point is located at $T_c = 44.49$ K and a molar entropy of $S_c = 30.76$ J/(mol K). The dashed lines represent regions. Taken from [10]

example, in *Pietrowski* work, it was shown that small droplets, $N = 300$, where N is the number of atoms in the cluster, are in a "liquid" state but for bigger droplets solidification starts to be present. In addition, the location of the dopant will be affected drastically by these sizes changes. When the droplet is in a liquid state the dopant atoms are free to move to the center contrary to denser droplets, where the dopant will stay at the surface.

The T-S representation of Helium, Fig 1.8 shows the isentropic processes as simple vertical trajectories. One advantage in this color plot is the visibility of the two-phase region where condensation may take place. The dashed lines represent isobaric lines at $p = 100, 1000, 10000, 100000$ Pa from left to right respectively. On one hand, supersonic expansions which originate in the vapor phase, at a very low source pressure equivalent to a comparatively large stagnation entropy s_0 , will not reach this region. On the other hand, for negative entropies the solid state is always reached although for lower temperatures and a relative small entropy, the liquid state is the predominant. [10]

1.3 Cluster-Intense Fields Interaction

The understanding of the interaction atom-fields has been study broadly in physics since Einstein Photoionization Theory [17], who gave a base on all the quantum electrodynamics theory. The basic idea supporting this theory is the behavior of light as an electromagnetic field, where the electron, as a bounded charge in the atom, can be affected. This quantum dynamic theory is well understood since

1957 for small atoms, with one, two or few electrons [3], but still big molecules and atoms have been challenging scientist for years. In this chapter we will give a brief introduction to the atomic photo ionization process, explaining at the same time multi-photoionization and tunneling processes, so we can finish with a more detailed presentation of strong field interaction with clusters and the Keldish theory.

1.3.1 Photolonization for single atoms

The photoionization process describes the withdraw of an electron from a bound state into the continuum by interaction with electromagnetic field radiation [6]. The atomic bounded electrons while going through an electromagnetic field, in our case the laser beam, can absorb enough energy to get excited and fly away from the nucleus. A bound electron only can escape from an atom by absorbing photons its energy exceeds the binding energy [17]. When the photon energy of the laser is smaller than the ionization potential of the target, the electron can absorb two or more photos in the ionization process, this is called Multi photon ionization (MPI). Another possible process is called, tunneling ionization, where due the quantum mechanical properties of the electrons under certain conditions absorbs enough energy enough to be in an above threshold regime, due it quantum dynamic properties it can escape from its bonds via tunneling.

There is a variety of theoretical approaches to describe the interaction of laser fields with atoms. The Hamiltonian of the system of N particles (ions and electrons) with pairwise Coulomb interactions under the action of an external time-dependent electric field has the form:

$$H = \sum_{1 \leq i \leq N} \frac{P_i}{2m_i} + \sum_{1 \leq i < j \leq N} \frac{q_i q_j}{|r_i - r_j|} + \sum_{1 \leq i \leq N} q_i r_i \varepsilon(t) \quad (1.9)$$

where r_{i,p_i} and q_i are the coordinates, momenta and charge of the particles, including the interaction between the classical electric field and $\varepsilon(t)$ where [50]

$$\varepsilon(t) = \varepsilon_0 e_z \cos(\omega t + \varphi) \quad (1.10)$$

The process that drives ionization can be divided on two regimes, a quantum electrical regime and a classical one [38]. Equation 1.9 use the non-relativistic approximation and neglect contributions from magnetic fields. The classical description of the laser field is a good approximation for intense pulses, otherwise, quantum electrodynamics description is necessary.

An electron in the initial level with energy E_i can absorb a photon with energy

$\hbar\omega$ leading to final transition where $E_f - E_i = \hbar\omega$, when the energy of the photon is larger than the bounding energy, or the Ionization barrier the electron is free with a the remaining kinetic energy $E_{kin} = \hbar\omega - I_{pot}$ [2]. In classical mechanics the probability of the energy transition depends directly on the cross section (σ) of the electron and the field. However, in quantum mechanics, the photoionization cross section is related to its transition probability between the initial and the final state given by Fermi's golden rule

$$W_{|i\rangle \rightarrow |f\rangle} = \frac{2\pi}{\hbar\hbar} |\langle f | H | i \rangle|^2 \delta(E_i - E_f - \hbar\omega) \quad (1.11)$$

$$\sigma(\hbar\omega) = \frac{2\pi}{3} \alpha a_0^2 \hbar\omega |\langle f | r_n | i \rangle|^2 \quad (1.12)$$

When Eq. 1.11 is the transition probability of one electron to jump from initial state i to final state f , where H is the Hamiltonian operator. Eq. 1.12 is the consequent cross section considering only the dipole part of the interaction Hamiltonian, where α is the fine structure coefficient, r_n is the position operator of the electron n [23].

The energy photon needed to ionize an atom, is directly proportional to the energetic distance between the electronic states and the ionization threshold. For states closer to the ionization potential a UV photon can be enough to free an electron but for inner electrons higher photon energies are required, varying from few eV to the order of several of keV, needing radiation sources at shorter wavelengths such as XUV to X-rays. [2]

After photoionization is complete, the electronic structure of the atom needs to rearrange due to the vacancy left by the ejected electron. Relaxation processes can happen during this time. An electron from the outer shell will decay and replace the freed one, therefore the energy difference of the needs to be released in the form of a fluorescence photon or Auger electron. On one hand, in case of a fluorescence decay the ionic state of the target does not change, since no additional electron is released. On the other hand, the Auger decay is a non-radiative relaxation process, where a second electron is released from the Coulomb potential of the ion [56].

In example. As shown in fig 1.9, if a photon with energy $\hbar\omega > E_{bin}$ ionized an electron, this will leave the atom lifting a gap. An electron in the higher levels will replace the outer one, leaving an excess of energy. The outcome will be a fluorescence process with $E_{flu} = E_{in} - E_{out}$ or , the Auger $e-$, if $E_{in} - E_{out} > E_{bond}$ and this electron can also escape the atomic Coulomb potential [61].

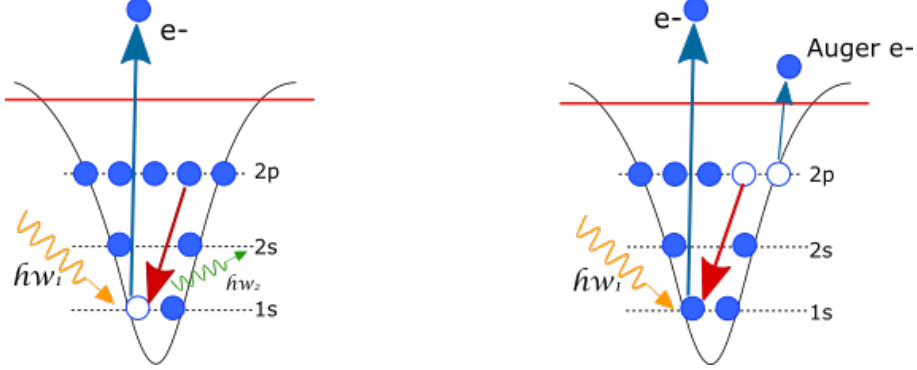


Figure 1.9: Two examples on the relaxation processes. On the left, A photon ionized an electron and the Electron E_{in} replaced, expelling a fluorescent photon in the process. On the right, the energy released by the replacement electron is enough to make another electron in the outer shell to also go to the continuum, Auger electron. Taken from [56]

1.3.2 Multiphoton and Tunneling Ionization

Ionization is also possible, even when the photon energy is lower than the binding potential. Laser Fields with intensities below $I \leq 10^{14} \text{ W/cm}^2$ are not strong enough to change the binding potential of an atom significantly [59] and it is when multiphoton Ionization takes place (MPI). MPI is the simultaneous absorption of several photons to overcome the ionization barrier. The way MPI occurs depends on the laser frequency and intensity. When the intensity is much lower than the characteristic atomic resonance, MPI occurs via transitions through virtual states. Ionization by several photons at low laser intensities can be realized by the so-called resonance enhanced multiphoton ionization (REMPI) [47]. Ionization by a REMPI process takes place in two steps. First, a resonant excitation by one or more photons occur on an electron state of the atom. In the second step, this electron state is transformed into a virtual state, to an upper state until the electron is excited by spontaneous decay. So for example, the total energy absorbed by an electron until it gets ionized is $n * \hbar\omega > I_{pot}$ where n is the number of photons absorbed until it actually have enough energy to overcome the potential I_{pot}

For Laser intensities $I > 10^{14} \text{ W/cm}^2$, with higher intensities and lower frequencies, tunneling ionization (TI) is more likely to occur. In this case, the binding potential of the atomic state is strongly affected by the electric field of the laser. Around the peak of the electric field the potential gets narrower, and the electron in the outer states gets closer to the bidding barrier, allowing the electron to tunneling through the confining potential to the continuum [27]. TI is inherently a quantum process. The bending of the Coulomb potential becomes by the superposition of the coulomb potential and the laser field. Therefore TI must occur when the time of the

ionization is shorter than a laser oscillation cycle [6]. Based on the same principle, when the laser field becomes so strong to lower the binding potential that separates the highest electron level, then the electrons in this state become free electrons. This process is called barrier suppression ionization or BSI [42].

In Fig. 1.10, we present a sketch of the 3 possible ionization processes explained above. On the left, a simple ionization process where a photon with energy $E_{phot} = \hbar\omega$ is higher than the potential barrier I_p . In the center, a MPI process is shown, n photons excite the inner-shell electron, exiting it through a virtual level until it finally has enough energy to be free to the continuum. Finally on the right, a TI happens. Here the coulomb potential barrier is affected by the laser files bending, the outer shell electron gets closest to it until it tunnels [56].

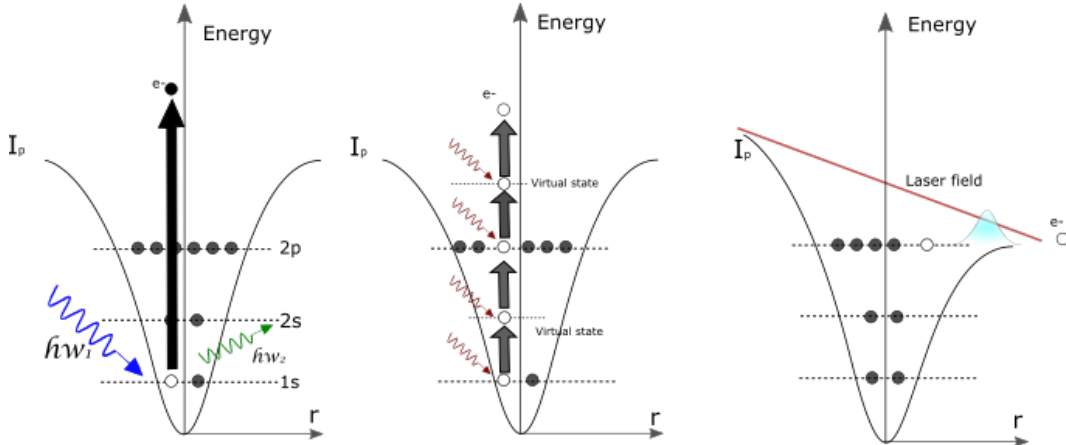


Figure 1.10: On the left is the sketch of a single photon ionization process, where a photon with energy $E_{phot} = \hbar\omega$ is higher than the potential barrier I_p . On the center the MPI process, inner-shell electron absorbs n photons, getting excited through the electronic levels (reals or virtual) until it reaches the continuum. On the right the BSI Process, the coulomb potential barrier bends by the laser fields, been lower than the outer shell electron state, the electrons can scape easilly. Based on [56].

As explained the Intensity of the external field plays an important role in the ionization process. A rather easy way to differentiate when each process needs to be taken into account is provided by the Keldysh parameter [39].

$$\gamma_k = \sqrt{\frac{I_p}{2U_p}} \quad (1.13)$$

Where γ_k is the Keldish parameter, I_p is the atoms ionization potential and U_p is the ponderomotive potential defined as:

$$U_p = \frac{e^2 E_0^2}{4m_e \omega_0^2} \propto I \lambda^2 \quad (1.14)$$

Where m_e is the mass of the electron, ω_0 , λ , I and E_0 are the frequency, wavelength, intensity and the peak of the electric field of the laser pulse. On one hand, when the Keldish parameter is higher, $\gamma_k \gg 1$ MPI regime is considered. On the other hand, the $\gamma_k \ll 1$ describes the TI interaction.

1.3.3 Keldish Theory

In this section we will give a brief introduction to the keldysh theory based on the work of Keldy et al, [39], and the papers review of the theory by [54] and [38]. For a deeply explanation we recommend the reader to reference this works.

The keldysh Theory, also known as the Keldysh–Faisal–Reiss theory (KFR), is well used for the description of quantum process induced by intense laser radiation. The applications and advantages of Keldysh formulation in many-body theory among several, can overcome from, treatment of systems away from thermal equilibrium, solutions in super symmetry methods of systems with quenched disorder or to the calculation of the full counting statistics of a quantum observable [36].

According to the Keldysh Ansatz, the transition probability amplitude between an atomic bound state and the continuum by the value of the photoelectron momentum p measured at the detector is given by [54].

$$M_k(p) = -\frac{i}{\hbar} \int_{\text{inf}}^{+\text{inf}} \langle \Phi_p | V_{\text{int}}(t) | \Phi_0 \rangle dt \quad (1.15)$$

Where M_k denotes the Keldysh transition probability, Φ_0 is the bond state wave function unperturbed and Φ_p is the canonical momentum, equal to p , also known as the Volkov function, and V_{int} is the electron field interaction operator. If the amplitude of ionization $M_k(p)$ is known, the differential probability to find the photo-electron in the elementary volume near the momentum p is given by the momentum distribution of the photoelectrons

$$dW(p) = | M(p) |^2 d^3 p \quad (1.16)$$

Giving a total probability of

$$W = \int | M(p) |^2 d^3 p \quad (1.17)$$

Meaning that, for enough long pulses, containing a large number of optical periods

so that its electromagnetic field is close to a periodical function of time close to the initial, it is physically more appropriate to use probabilities per time unit (rates) instead of time-integrated values.

1.3.4 Ponderomotive energy

As soon as an electron is released into the continuum, it starts to be under the influence of the external laser field. A description of the energy that it acquires during this interaction is given by the ponderomotive energy (PE).

$$U_p = \frac{e_2 E_a^2}{4m\omega^2} \quad (1.18)$$

Where m and e is the electron mass and charge, E_a and ω_0 amplitude and frequency of the electric field respectively. The formula of the ponderomotive force can be easily derived as shown in [55] [11]. Let's consider a polarized electric field (in a.u.).

$$E = \hat{z}E_a \sin(\omega_0 t) \quad (1.19)$$

Considering only the \hat{z} -components so we can avoid the vector sign. By classical mechanics we have.

$$p(t) = - \int_{t_0}^t E(t') dt' = \frac{E_0}{\omega} (\cos(\omega_0 t) - \cos(\omega_0 t_0)) \quad (1.20)$$

The term on the left of the parenthesis is known as the time varying Quiver terms, and on the one on the right, refers to the drift motion. Expressing the fields in terms of vector potential we will have

$$E(t) = \frac{\delta A(t)}{\delta t} \quad (1.21)$$

$$p(\infty) = A(t_0) = - \int_{-\infty}^t E(t) dt = \frac{E_0}{w} \cos(\omega_0 t_0) \quad (1.22)$$

in the case where the pulse duration is big $t \rightarrow \infty$ the $p + A(t) = 0$. This means that the momentum acquired by the electron will depend on the phase it is realized wt . Since the electron can be unbound in any phase of the laser pulse, will have an average kinetic energy described by

$$U_p = \frac{1}{2\pi} \int \left(-\frac{E}{w} \cos(wt) \right)^2 d(wt) = \frac{E_0^2}{4w_0^2} = \frac{p_{max}^2}{2} \quad (1.23)$$

The ponderomotive energy also gives the maximum momentum that an electron can acquire (eq. 1.22), given at the maxima. The ωt phase relation, defines what it called *the three step model* showed in figure 1.11 . The first step corresponds to $\omega t < \pi/2$ where the laser field is suppressed, and as explained above, TI or BSI can take place. The second step, is where $\omega t > 3\pi/2$, on contrary step 1 the potential barrier is enhanced, electrons in the continuum that was winning kinetic energy are caught by the potential again, being driven back to the atom. Finally the step 3 at phase $\omega t = n * \pi$, for $n=1, 2, 3, \dots$. At $n = 2$ it is called "recollision process" of the electron. Where the electron can be caught by the potential again, and the excess of energy release another bound electrons, depending on the kinetic energy necessary [41]

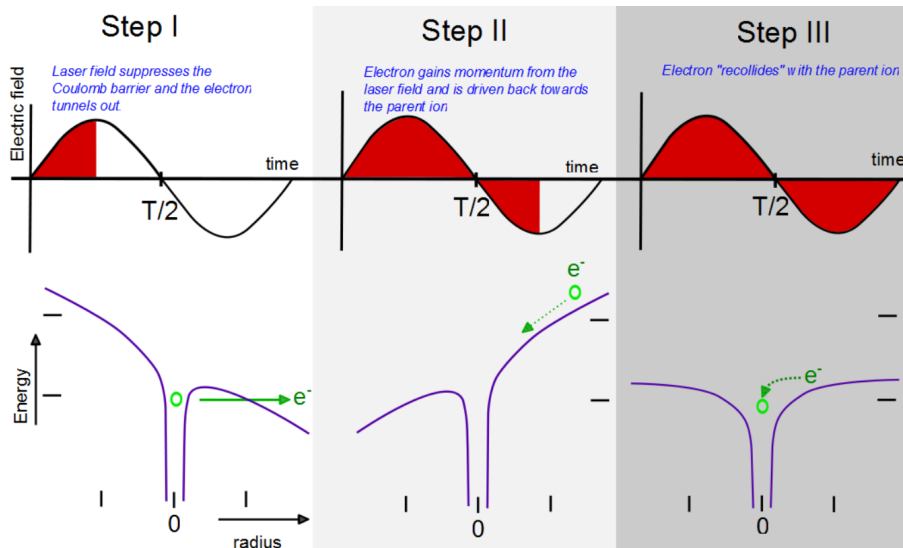


Figure 1.11: Recollision process at the three step model. Taken from [42]

If we transform the eq. 1.23 to laser intensities we will have $U_p = 9,33 * 10^{-14} I [W * cm^{-2}] \lambda^2 [\mu m]$. For a MIR-pulse with intensities $\sim 10^{14} W/cm^2$ and $\lambda \sim 3200 nm$ we have electron energies between one and a hundred of eV.

1.3.5 Cluster Ionization

Until now, we have described the most known ionization processes for single atom. But on cluster ionization, the dynamics are more complex and involve more parameters. Clusters are combinations of atoms or molecules which, depending on their species, are held together by Van der Waals forces, ionic bonds or metallic bonds. In this explanation we refer from now on only to He cluster, which mainly are just affected by Van der Walls attraction [64] and its interaction with the Laser Fields, specifically pulsed laser with a wavelength smaller than the cluster size, meaning

that all the atoms in the cluster are equally affected by the pulse, in other words the Field penetrates all over the cluster.

The first challenge to overcome when working with Helium, is its Ip. Being a rare gas, its ionization potential is higher than many of its doping molecules used. For example, under MIR lasers helium clusters need $I > 10^{15}$ W/cm², so TI or BSI is not the main process at the beginning of the plasma generation. Other interactions have to be explained in order to describe the process properly. This section we will be based on *Saalaman et. al* work [60] and *Grüner et. al* [28], for this purpose, we will divide the process in three phases or stages.

In the first stage called “*atomic ionization*”, the doping atoms are ionized independently of each other by the electric field at the leading edge of the laser pulse, it occurs mainly through inner ionization, especially on TI or BSI. The resulting free electrons acquire positive kinetic energy and have two options, leaving the cluster or they stay inside the cluster attracted to its positive ion core. After the first stage, the cluster becomes into an “ignited” nanoplasma, consisting of ions and quasi-free electrons, electrons that are free to travel inside the cluster volume but still not into the continuum [43].

The second stage is the *nanoplasma expansion*. During this stage the cluster is still interacting with the laser field, acquiring, by a large number of processes, energy by its atoms and electrons. Ions are further created by a combined force of the laser and other ions, the *ionization ignition* [28]. Quasi-free electrons oscillate, driven by the laser pulse and are heated to high temperatures. The heating becomes extremely efficient when the collective oscillations of quasi-free electrons become resonant with the laser pulse, Triggering a cascade reaction to more outer ionizations, freeing the remaining electrons in the cluster, this process is called *plasma resonance* [60].

After the laser pulse is over, the last stage starts. The ions continue to expand, in consequence, the radius rises as same as the cluster potential becomes smoother. So, it is easier for the highly energetic quasi-free electrons to leave the cluster, forming a coulomb explosion that destroys the cluster in a ions-electrons cascade. This process was first described by *Ditmire et. al* [15] combining high energetic collisions with cluster resonance absorption.

The graphic 1.12 shows on the left how the cluster potential is composed by the Van der Walls potential and atomic forces of the different atoms that compose the cluster. On the central images, additional to the atomic biddings, the electrical force due the ions in the cluster increase the potential, the laser pulse is still on and the quasi-free electron will gain energy while they are in this. Finally, on the right the laser field is off, the electrons have fled away and the cluster ion have been repelling

each other so the potential is reduced to the minimum(just atomic interactions.)

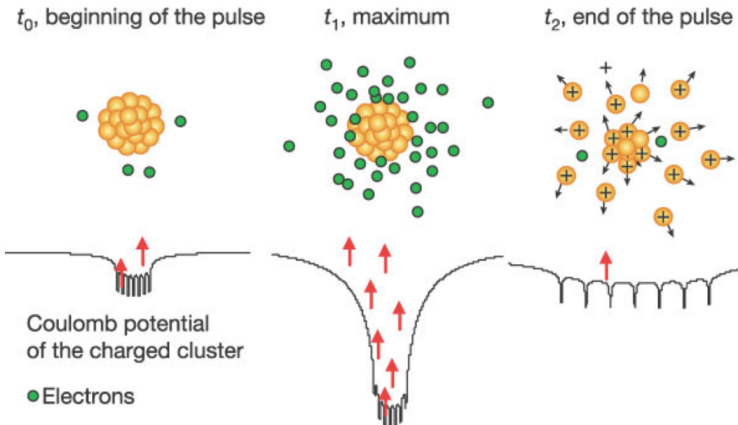


Figure 1.12: Cluster potential regimes. On the left, the atomic ionization starts the plasma formation. On the center, the quasi-free electrons auto-ionize the cluster, increasing the potential barrier and gaining energy due the laser field so a coulomb explosion can take place. On the right, The Coulomb explosion is finished, the potential is driven to it minimum and all the electrons and ions are ejected. Taken from [72]

1.3.5.1 Cluster expansion

Depending on the droplet size and the laser intensity, the Cluster can expand in two different ways. If the laser intensity is rather high and the droplet is small, a Coulomb explosion can occur. On the contrary, if the laser is not intense enough or the droplet is too big, a nanoplasma can be generated, therefore a hydrodynamic expansion will take place. Two forces are really important during the cluster expansion. Both act on the cluster during the phase two and three (during and after the laser pulse). The first, is the force associated with the free electrons with high kinetic energy. These hot electrons expand and pull the low energetic electrons and heavy ions on its pad [15]. The other force acting on the cluster is due to the inner cluster charge itself. The hottest electrons in the cluster will have a mean free path large enough so they can free stream directly out of the cluster, and, if the electron's energy is large enough to overcome the space-charge buildup on the cluster, they will leave the cluster altogether. If the charge buildup is sufficiently large, the cluster will undergo a Coulomb explosion [33]. According to Madison et all, a time scale for the laser pulse duration where the coulomb explosion can take place should be closer or lower to the femtosecond regime, depending on the element composing the cluster. [46]. Based on the laser power available on modern laser pulses, the same studies present

that electron after a coulomb explosion can get kinetic energy up to 6KeV.

When the intensity is not enough to make the atomic bonds to break, the electrons remain in the cluster forming a hydrodynamic expansion as a result of a conversion of electron-thermal energy to direct kinetic energy [20]. The effects that the expansion has on the electron temperature can be calculated by equating the rate of change of radial kinetic energy from the thermal contribution with the rate of change of thermal energy within the cluster. When this condition is fulfilled. The electron can present a resonance condition in the cluster, traveling in the space-charged forces formed by the plasma, winning enough kinetic energy until all the system collapse.

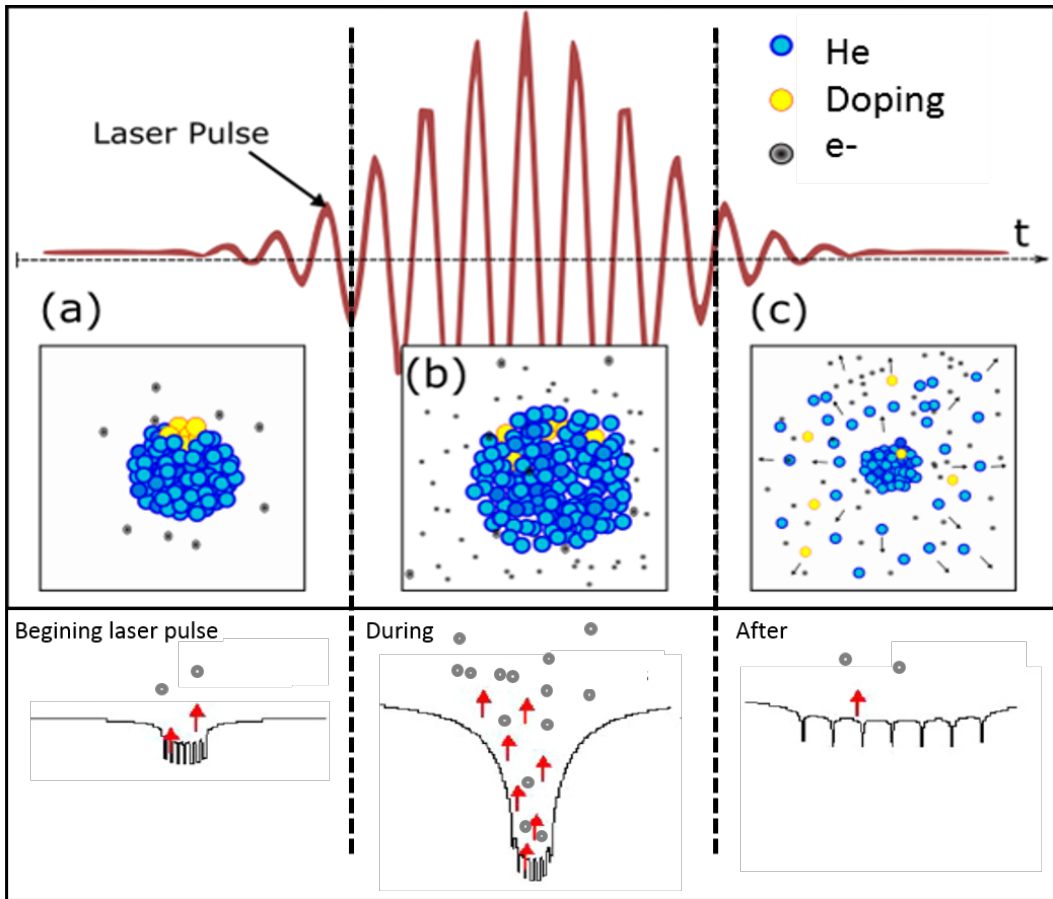


Figure 1.13: sketch of the Coulomb explosion for a doped cluster due the excitation of a pulsed laser field. At the beginning of the process the laser ionized the droplet, until some femtoseconds (up to 500fs) after, the system collapse and result into a coulomb explosion.

Although the two models are different in each regime, for example, at low kinetic energy or the beginning of the pulse, the Coulomb explosion produces less ions for low energies compared to the product on hydrodynamic explosions. Further, the number of high energy ion the coulomb explosion can create (although in less quantity) tent to be hotter ions too. We have to take into account that even the two

processes are described for different laser regimes. Both processes can happen in parallel, but at certain energies is clear, that one or the other will be the responsible at the end, for the collapse of the system.

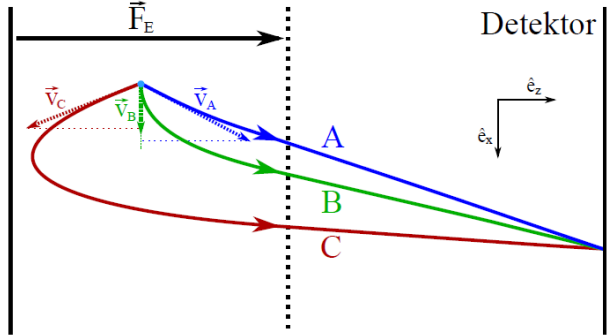
1.4 VMI spectrometer

Velocity map imaging (VMI) is a widely used technique in areas such as atomic and molecular physics and physical chemistry. It is used to investigate velocity distributions of charged particles, which are generated in a defined volume, typically by photoionization. A laser pulse generates charged particles by photoionization in the interaction region, which are accelerated by an electric field created by two electrodes. The VMI used in this experiment is a modification on the original design by Eppink-Parker [19]. Its is made by a lower electrode called Repeller followed by the extractor, ground electrodes which generated the electric filed that drives the particles to a detection system consisting of an Microchannel plate or MCP and a Phosphor screen, which is observed by means of a CCD camera on top. All electrodes have a circular layout and are about 1mm thick. The extractor and ground electrodes have a concentric hole where the particles pass through. Once the Electron or Ions, guided by the electrodes, arrive to the MCP an electronic avalanche occurs, increasing the signal of each individual particle. The electronic avalanche hit the Phosphoscreen producing photons that can be detected with the camera focused on top.

1.4.1 Velocity distribution in VMI

In order to describe the velocity distribution detected by the VMI, we assume that the charged particles come from a point in space emitted between the Repeller and the extractor. Furthermore, we presume that the initial kinetic energy of the particles obtained during the ionization process is small, in comparison to the energy supplied by the electric field. The initial conditions of the charged particles are determined by the ionization volume and the initial velocity vectors $v_i = (v_x; v_y)$, whose distributions are of interest. The particles are drive by the Electric field in the direction v_z to the spectrometer axis. If one starts from an isotropic initial distribution for the velocities, particles with differing initial velocity vectors can finish in the same point on the detector, as shown in fig 1.14. This results in a loss of information, its is expected because we are trying to 3D information from a 2D projection.

Figure 1.14: Representation of particle trajectories A, B and C of the ionization volume to the detector plane, which, in spite of initially different velocity the finish on the same point of the detector plane. Withdrawn from [21]



Assuming a cylindrically symmetric distribution $f(r, y)$ along the y -axis. If an infinitely far away observant look at the distribution F along the z -direction. With a basic axis conversion it can be shown that along the Z direction, the projection of the distribution F of the integrated signal respond to.

$$F(x, y) = 2 \int_{|x|}^{\infty} \frac{f(r, y)r}{\sqrt{r^2 - x^2}} * dr \quad (1.24)$$

Been F in cylindrical coordinates and $r^2 = x^2 + z^2$. Also called *Abel-transform*. But in order to resolve our signal we need the opposite procedure, turn this 2d distribution into the 3d spherical distribution that we assume in the beginning. For this process is called *Inverse Abel-transform*, and it can be shown as.

$$F(r, y) = \frac{1}{\pi} \int_{|x|}^{\infty} \frac{dF(x, y)}{dx} \frac{1 * dx}{\sqrt{r^2 - x^2}} \quad (1.25)$$

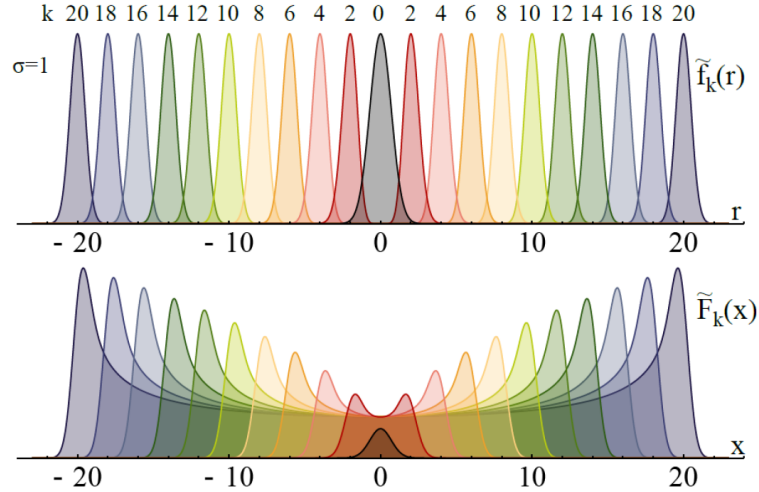
The main problem that carries this transformation is that is not resolvable to a non-continues distribution that is the case of the Images recorded by the camera. So a numerical method needs to be used. Fortunately, a Software PbaseX, is available to solve this integral. The idea is to have a basis function f_k (in this case Lagrange polynomial) in the space of distributions f . Their projections F_k onto the detector are well known, and the Able transform will be set as:

$$F_k(x) = 2\sigma\rho_k(x) \left\{ 1 + \sum_1^{k^2} \left\{ (x/\sigma)^{-2l} \prod_{m=1}^l \left(\frac{(k2+1-m)(m-1/2)}{m} \right) \right\} \right\} \quad (1.26)$$

If every measured image can be expressed on this basis, then the reconstruction of the F distribution when $k \rightarrow \infty$ can be obtained. A graphical example of this

transformation is given in fig ?? where each color represents a f_k projection, where all f are in the same basis, the sum of all the different f will set the final reconstructed F_K .

Figure 1.15: At the top of the graphic some basic functions f_k in different colors, which can be used for the Inverse-Abel transform in the Basex method. On the bottom, the corresponding Abel-transformed functions \tilde{F}_k . Taken from [21]



2 Experimental setup

In this chapter, we will present the experimental setup, giving special attention to the Nanodroplets generations, the doping process and the data acquisition system. A subchapter is also dedicated to the single shot correlation data acquisition system tested specifically for this Master's project. The apparatus we worked with, is part of the group of Molecule and Nanophysics at the University of Freiburg, Germany, and was calibrated and used for the experiments in [62] and [34].

In figure?? a sketch of the apparatus is shown. From left to right, the source chamber where the ultra-cold molecular beams are produced. The central chamber or "doping chamber", where the beam gas is doped via pick up process using a gas doping cell or a diffuse oven for alkalioids, where gases or thermally vaporized solids are used as dopants. The last chamber or "detection chamber", combines a VMI-TOF detection system and a Langmuir Taylor (LT) detector. To generate the nano plasmas, the apparatus was used in two different institutions, at the Max Plank Institute for Nuclear Physics in Heidelberg and the Extreme light institute (ELI) in Szeged, Hungary, because of the special laser systems that can be provided in there.

The following sections describe the essential components of the apparatus and the new Triggering systems implemented to correlate the VMI and TOF signals. The structure is compacted to a length of about 240 cm long, each chamber has attached to its own turbo pumps with pre-vacuum scroll pumps and separated by valves and skimmers. On one hand, this enables to manipulate the vacuum in an independent way and control the targets in the "detection chamber". On the other hand, allows an optimum adaptation of the suction power of the pumps to the gas load of the individual chambers, as well as, to ventilate and open without having to disturb the entire system.

2.1 Source chamber

The Source chamber consists of a 6-way CF vacuum chamber, with a 2-stage cryostat which powers a cold-head that can be cooled down to 9K. It is located at the entrance of the chamber, parallel to the floor with an attached conical nozzle for the gas

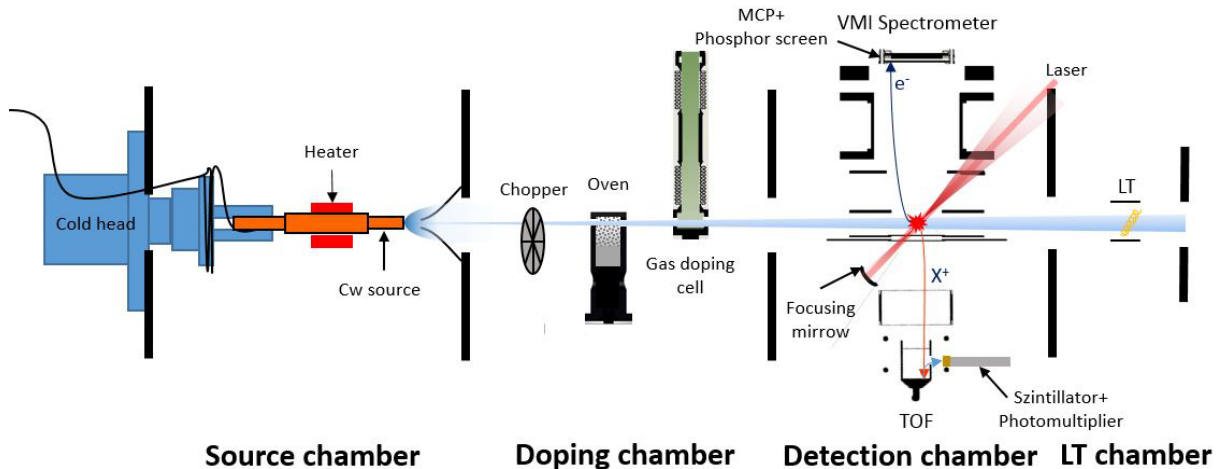


Figure 2.1: Sketch of the vacuum chambers, including the main parts of the setup

expansion process. The cooling capacity of the cryostat consists of a copper tube, into which pre-cooled helium is introduced. It can be adjusted by operating two heating resistors in combination with a sensor diode for temperature measurement and a PID controller. Controlling the resistor current the temperature at the end of the nozzle can be kept stable. The conical nozzle used to generate the atomic beam is the standard used in the research group on Nanoplasm research directed by Prof. Frank Steankeirmeyer at Freiburg University. It is made of copper and has a platinum plate in front with a hole of $5\mu m$ of diameter for He experiments and $15\mu m$ for Ne gas clusters. The diameters were chosen in order to follow the size dependence of the *Hagenas* law, which together with the adjustable gas pressure and the nozzle temperature regulates the flow. The cold head-nozzle arrangement are connected to the chamber via a self-made x-y manipulator, with a thermally insulating rubber ring, which allows a beam adjustment in relation to the other components in the setup without breaking the vacuum. At the bottom of the chamber an Agilent turbo pump of $1800L/s$ capacity is attached to a pre-vacuum scroll pump as exhaust. A skimmer with a diameter of $400\mu m$ is located in front of the effusive jet, sorting the gas beam not just by size but also by its velocity vectors, allowing just those beams with direction along Z. To adjust the nozzle optimally to the skimmer, it is connected to an x-y displacement unit and can be aligned from outside the vacuum chamber. To prevent the small opening of the nozzle from clogging over time, high-purity helium 6.0 (99.9999% purity) and Ne 5.0 (99.999% purity) are used, this clean gas ensures a constant gas flow through the nozzle. At this extreme temperature any impurity in the gas bottle can condense, blocking the nozzle or changing the conditions of the clusters formation.

2.2 Doping chamber

As explained, the doping process takes place by inelastic impacts with atoms from the gas phase, referenced as the pick-up technique. In this experiment we doped with both metals and noble gases, and two different methods of doping are used: Metals are heated in evaporated phase in the oven, while gas dopant yield in a Gas doping cell entered the vacuum chamber through a needle valve. On the next section, we will explain the elements of the doping chamber and its most important characteristics used.

The oven chamber is connected after to the Source chamber via the skimmer, it is also a 6-way CF vacuum chamber, with a turbo pump on the bottom, connected to its own pre-vacuum scroll pump. On the sides the flanks allow a cold trap not used in this experiment, on the other side the flank that permit connection to the oven and the vacuum sensor. The Skimmer is made of Nickel, a very thin metal easy to bend, so in order to prevent strong pressure differences in the chamber that can modify the skimmer, a bypass is connected between the two chambers using a stainless steel flexible hose. An internal stand is welded to the front of the chamber and aligned with the skimmer. This stand supports the Chopper, the gas doping cell and the oven. In the front the rail the choppers is located. It is a steel disk with three notches uniformed located, two photocells around the bottom of the disk reads the position of the bottom notches so the upper one can be positioned right in front the skimmer. In this way, when the disk rotates the beam can pass or its block by the disk in a controlled way.

After the chopper, there is the Gas Doping cell, a circular flat metal base with a self-modified KF hose. The base of the cell has a matching pattern so the hose can be easily put and remove without losing the alignment. The stainless steel flexible hose has two 5mm hole (one in front and one opposite to it, some cm up the base) aligned to the skimmer so the gas bean can go though. The hose is fixed to the base and goes to the top of the chamber where it is connected to a "swagelok" needle valve that allows to control the gas flux for doping the beam. A Pfeiffer CMR375 Capacitive sensor is located after the needle valve so a better control of the pressures and the number of dopant in the cluster. The bendable construction allows, not just to remove the doping cell without difficulty, but also to fit it on the top without depending on a fix way to locate the top plank, in this way there is room for maneuvering and the installation is faster.

Finally, at the end of the rail lies the Oven. As shown in fig 2.2 the oven consists of a patterned base (similar to the gas cell) that can move a few mm on $x - y$ plane. Over it, a metal cylinder with 4 heating cartridges holds a movable crucible in the

center that contains the dopant sample, this movable container is set down by a rod that comes from the top of the chamber after a valve. Both, the stove and crucible have holes (a conical entrance of 40mm diameter and 3mm diameter respectively) that allows the pass of the gas beam and are aligned to the beam pad, in this way the passing Atomic beam takes dopants via collisions with the vaporized sample material.

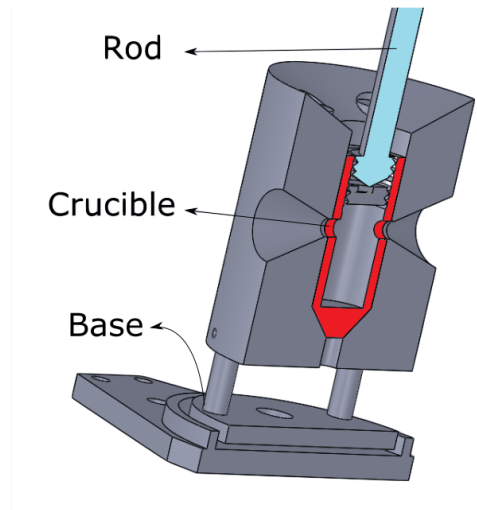


Figure 2.2: Cut of the Oven design, including part of the rod and the crucible.

One important advantage of this new oven design done by *Dominic Schomas*, is that the dopant can be change without braking the vacuum, it was tested in this experiment and prove to be useful in saving time and effort. To control the temperature of the oven a temp sensor is fixed in the stove, and the resistors current is manage by a PID controller allowing a stable temperature during the experiment. The maximal temperature reached was 450°C , enough to create the gas phase for the potassium K and calcium Ca used in this experiment. Finally, there is an extra skimmer of diameter 2mm, fixed to a valve between the connection of the doping chamber and the detection chamber that helps to avoid the disperse beams or an overflow from one chamber to the other.

In addition to the doped gas nano droplets, effusive gas is also released from the dopant chamber into the detector chambers through the needle valve and can be ionized and detected there. This disperse gas was pouring in directly on the chamber or filtered by diffused atoms going out of the oven and passing across the second skimmer once the choppers is close. This atomic gases were added for calibration of the detectors and background reduction allowing just one gas at a time.

VMI	Repeler	Extractor	Lens
X1	-2430	-1940	3500
X3	-7290	5820	10500
Ion	2430	1940	0

2.3 Detection chamber

As mentioned, the detector chamber is connected to the Oven chamber through a valve and a skimmer. The detector chamber contains a newly developed Velocity-Map-Imaging Spectrometer on top, a time-of-flight mass spectrometer on bottom and a LT detector in front. In this section we will give a brief presentation of the VMI and the TOF used for this experiment, taking special interest in the new Triggering process that allows to detect single nanoplasma explosions.

2.3.1 Velocity map imaging VMI

The VMI detector used in this experiment is detailed in [62], this construction basically follows the standard geometry of Eppink and Parker [19]. It is composed by three electro lenses (Repeller, lens and extractor) that focuses the ions or electrons on a 86,6mm (effective area) diameter Micro channel plates (MCP) arrange. This detector set is basically two MCP's superposed, rotated to each other and a phosphoscreen (PS) layer of same diameter facing the top plank of the chamber with a Ca-fluoride glass of 1mm thick. An external CCD camera is focused to the PS.

The voltages applied to the MCP and PS determine the brightness of the final pictures of the ions, so in general just one set of voltages has been used, around 1400V for the MCP and 4000V for the Ps. The achievable energy acceptance for this stack is 34eV for a the VMI setting 1 and 270eV for the X3 settings. The VMNI have a resolution of $\Delta E/E \leq 4\%$ [62]. The camera used in the experiment was a Basler acA1920-155um focused on the PS.

On fig ?? we present a view of the model of the VMI used in this experiment, From bottom to top, the structure of the electrodes consists of two Repeller electrodes separated by a few millimeters with circular openings on which a fine mesh copper grid is applied, an aperture electrode as Extractor, another aperture electrode which is held at ground potential and then from the extended lens electrode with the following second ground electrode. At the top, the MCP-PS arrange (on black the MCP and on gray the PS) facing the center of the window installed in the top plank of the chamber. Around the window there are three connections that allow the voltages for the electrodes and the cables are carefully arranged around the structure to avoid discharges or even disturb the uniform electric field.

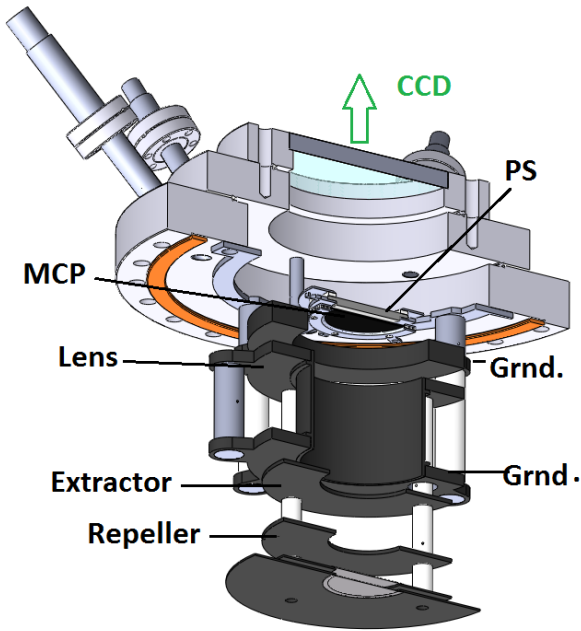


Figure 2.3: Sectional cut view of the CAD model of the spectrometer setup. On black, the electrodes and the white the Polyether ketone (PEEK) isolators. On orange, the cooper ring and on blue the top window facing the CCD camera

The openings of the Repeller (at the bottom in bluish color) electrodes allow the use of these electrodes as well as extractor electrodes for a TOF spectrometer. In simultaneous operation of the VMI and the TOF spectrometer, the glued grids prevent mutual field effects of the two spectrometers. The Repeller and extractor are grade 2 titanium and the lens is stainless.

2.4 Time of flight spectrometer

The Time of flight (TOF) spectrometer used was based on the design by Wiley and McLaren [75]. As its name refers, the TOF mass spectrometer relates the time that a particle at an electric field requires to reach certain distance with its mass, when atoms and molecules are photoionized, they pass through an electrostatic acceleration field and are registered in a detector after crossing a field-free flight path. Based on the flight time the ratio m/q of a particle can be determined as:

$$t - t_0 = a \sqrt{\frac{m}{q}} \quad (2.1)$$

Where a is an experimental factor depending of the flight distance, electric fields and material of the setup, m/q is the relation mass - charge, t_0 is the time ionization

time (given by the laser) and t is the time of flight.

The ions creation takes place in the aperture between the Repeller and extractor electrodes. Behind the extractor electrode there is a further aperture electrode, which is held at zero potential and thus generates a pre establish flight route with a defined field, grids are glued to the openings of the electrodes to prevent the propagation of the fields through the orifices in the electrodes. The Repeller electrode is set to a positive potential and the extractor to a negative potential. The resulting electric field accelerates the ions through the openings in the flight tube, on which grids mount on both sides keep the drift path free of field. Once the coulomb explosion takes place, the ions are accelerated by the electric field of the Repeller and then fly through a field-free drift path to the detector. This allows a complete mass spectrum to be recorded within a few microseconds in a single measuring step [48].

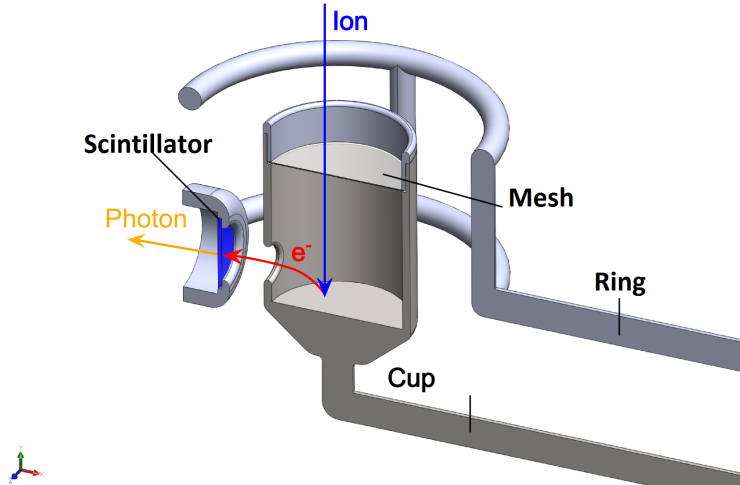


Figure 2.4: Illustration of the functional principle of a Daly detector.

The flying Ions finally are detected by a Daly detector [12]. It consists of a cup, a grid and a ring. The cup lies on negative high voltage while the ring for positive. The ions from the Repeller pass through the field free tube corrected by a drift electrode. Since in the direction of the hole the potential for electrons drops sharply, the ring electrode generates an electric field, which directs the ions into the cup. The ions that pass the grid at high speed hits on the bottom of the cup, they generate some electrons, which are transmitted through a small hole in the bottom and then in a scintillator Eljen thechniloy (EJ-204) flashes some photons in the process. These light is detected in a Hammamatzu r-647 photomultiplier (PM). The voltage output of the PM is controlled by a fast analogue-to-digital converter, and it is used at 900V voltage. The cup and the drift-scintillator tube was set at high voltages, $-17000V$ and -4000 respectively.

2.5 Lt detector

The Langmuir-Taylor detector (LT detector) chamber consists of a small CF40-6-way chamber. The detector consists essentially of an annealing filament, which is located between two planar round electrodes. The Operating Principle of an LT-Detector is based on surface ionization by the tunnel effect [14]. For the annealing filament is typically used rhenium, platinum or tungsten, as this is the most common due its comparatively high electron work function. With high voltages, the wire reaches high temperatures, as a consequence, a passing neutral atom is ionized, releasing an electron into the wire. The resulting ions are attracted by the negative electrodes around the wire generating a current. The ionic current generated at the electrodes is proportional to the number of ionized atoms and is measured using a Picoammeter. The LT chamber is connected to the VMI chamber via an orifice plate and is used mainly as a beam dump and to align the detector. The most current generated in the chamber the most atoms are passing through the hole, so we can be sure that the beam pad is in the detection area.

3 Acquisition and calibration methods.

In order to use the above setup with the MIR and NIR laser parameters, the methods used in this experiment are explained in this section, from the VMI calibration techniques to the data analysis process. All experimental techniques were used to investigate either helium or neon clusters.

In our experiment, in contrast to other spectroscopic techniques, the Photoelectric spectra (PES) of the $e-$ VMI looks different for each signal because of the size distribution of the clusters production and the different focus intensities each cluster is exposed to. Nevertheless, the images and therefore the PES look rather similar in shape, small circular blops in the middle of the detector with a clear edges and a brightness higher than the background. For larger clusters ($\langle N \rangle = 10^6$) small deformation in the circles shows up. For example, some images show small-medium uniformly bright circles while others signal, shows high intensities in the edges and lower in the center, like a "donut" shape, as we will refer from now.

Taking advantage of the setup and the possibility to record individual signal in the TOF and the VMI spectrometer, we develop a method in which the data of both techniques are correlated to describe a single coulomb explosion, described in the following section. One disadvantage of our setup is that the maximum acquisition rate is 30Hz, the minimum exposure time of the camera. Depending on the hard drive that is used, the acquisition rate can drop to 10Hz. Furthermore, the single shot method needs low event rates of less than 10%. It results in an event rate of less than 1Hz. Nevertheless the results section shows that the technique was suitable enough to the laser specifications used for all the experiments and none further changes were needed.

3.1 Camera and trigger protocol

One of the main objectives of this project, is to record individual data for single shots nanoplasma explosion in the VMI and TOF. The advantage is the ability of

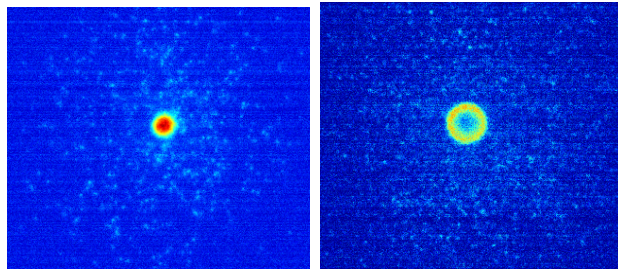


Figure 3.1: Example images of MIR VMI signal. On the left, a uniform bloop, on the right a "donut" shape signal with high density signal on the borders of the edges.

the threat the data in a separate way to reduce the background and know the energy distribution information that is lost when data is averaged.

Two methods were developed. A first approach was done using a software triggering for the CCD camera and the oscilloscope, an Acqiris Card CC103, for the TOF. Using Lab View, an external clock (a RaspberryPi 3) was triggered by the laser, the beginning of the explosion, at the same time, it software-trigger the camera and oscilloscope programs to start the acquisition. Having all the data acquired in the same software would allow to sort the data online and reduce the storage needed for the experiment. The Lab view program was tested unsuccessfully for the data acquisition rate needed in ELI 100 KHz, the main problem was that when a software-triggering scheme is used, extra delays are applied due to the operating system and the communication protocols, so even the data were acquired at the same time the delays at saving the information in the hard drive made impossible to correlate the signals.

Based on that same idea, a second approach was used. As alternative of the software triggering, a hardware triggering was used. The laser triggers a delay generator that at the same time triggers the oscilloscope, a *R.S* RTO2000 with bandwidth of 600MHZ to 6GHz, and the camera. Two facts need to be taken into account, first, the minimal exposure time of the camera is $34 \mu\text{s}$. Second, the timing between the camera receiving the trigger signal and the real start of the acquisition is not negligible as it is for the oscilloscope. The camera took 5-6 μs to start after the trigger was sent. To solve this problem the triggering scheme in Fig. 3.2.

A delay generator (Stanford Research Systems MD DG335) receives the laser trigger (100KHz), channel B and C were connected to the oscilloscope's channel 1 and 2, channel A was connected to the pin 1 (trigger) of the camera. Due the limitation in the exposure time of the camera, we cannot identify a single laser shot with it. Table 3.1 shows the delays used in the experiment, where T is the original laser trigger and A, B and C are the channels in the delay generator. The

List delays

Channel	Set to:
A	$T + 0$
B	$T + 1\mu s$
C	B or $B+6 \mu s$

Table 3.1: Trigger Channel delays

oscilloscope can identify each individual laser shots but the camera will see at least 3 shots. Fortunately, not all laser shots generates signal, the signal rate oscillates between 3 to 10% of the total images, this mean that most of the pictures will have no signal, rare cases will have two or more, but the majority of the pictures with signal will contain just one explosion in the VMI that can be correlated to its individual TOF signal.

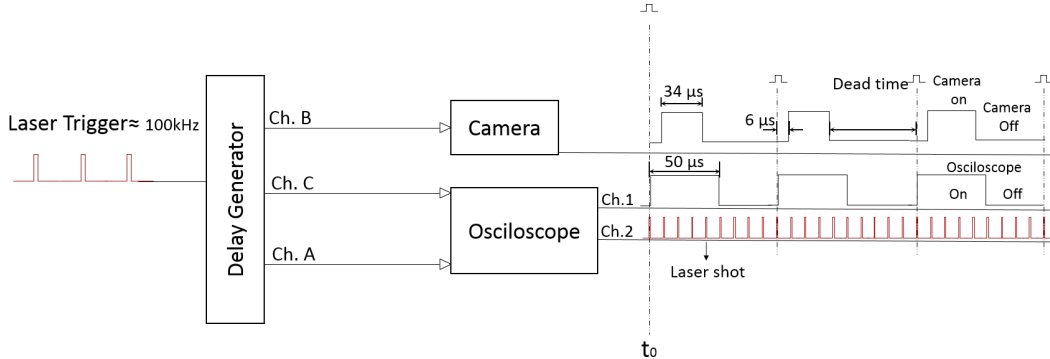


Figure 3.2: Scheme of the trigger system used.

In Fig 3.2, we show the Trigger scheme used in the experiment. The oscilloscope and camera are triggered by the delayed channel B. The oscilloscope is set to $50\mu s$ and the camera to the minimal exposure time. So the camera and oscilloscope sees the same trigger, the oscilloscope will record at least 5 laser shots, but the camera because starts later just can see three as shown. The pictures are saved in the memory RAM of the computer so the dead time after the camera is off is mandatory to give the operating system enough time to save the data on disk and don't get out of ram. A small improvement in this system can be done if we trigger the camera with B and the oscilloscope with C, so both apparatus can start almost at the same time and no corrections need to be done. Each of the data set is save with a unique label to correlate the signals after. Once an explosion is found in the VMI pictures, we check in its corresponding TOF that to proof there exist just one explosion in all five laser shots, so we can be sure that picture correspond to a single coulomb explosion, in case more than one signal is found, this picture is discarded.

Fig 3.3 shows an example of some electron-VMI pictures to its corresponding TOF, where just one peak in time shows the single explosion during the exposure time of the camera.

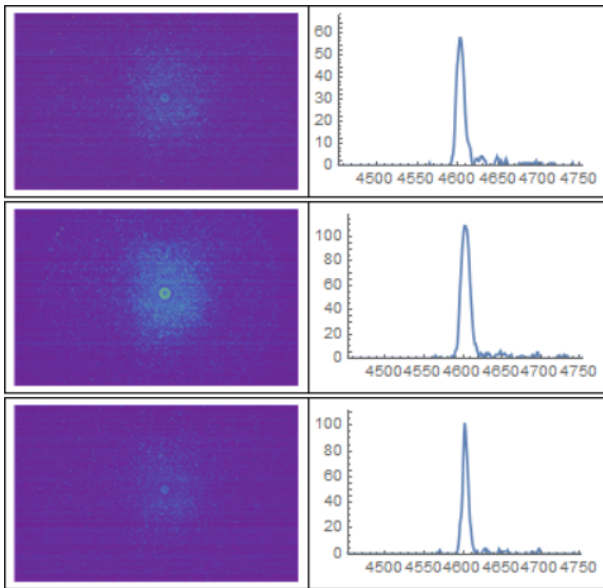


Figure 3.3: Example of VMI-TOF correlation signals for He droplets, in the left some Electronic VMI pictures and on the left the Ion yield, time for the X-axis in μs and on the Y-axis the signal strength in a.u

3.2 Calibration methods

3.2.1 VMI calibration

To calibrate the VMI spectrometer, two different methods were used. A quadratic calibration function $E = \alpha \cdot r^2$ is used, where E is the kinetic energy of the particles and r is the measured radius. This function is chosen because $E_{kin} = 1/2 \cdot mv^2$. In order to keep the simplicity, stray fields, third order or linear terms are not included, as long as the calibration curves fit well with the measured.

On one hand, the most independent method is the trajectory simulation, because it does not rely on any laser system or physical process. These simulations were done by Dominik Shomas with SIMION 8.1. For the starting conditions for the electrons we chose a small interaction volume comparable to the estimated experimental conditions and the emission direction perpendicular to the spectrometer axis. For those electrons the projected energy on the detector screen is equivalent to the real kinetic energy, with this the inverse Abel transformation can be avoided. It is necessary to simulate different kinetic energies for the electrons, at different velocity vectors.

After extracting the radii, where the electrons hit the detector plane, a calibration from pixels to mm for the camera is needed, because SIMION gives the radii of the electrons in mm. To do so, known distance in the camera image is needed, for example the inner diameter of the phosphor screen, making possible to generate the fit curve. The disadvantage of this method is, that it is very difficult to include any magnetic or electric stray fields into the simulations or other external parameter that can be in reality.

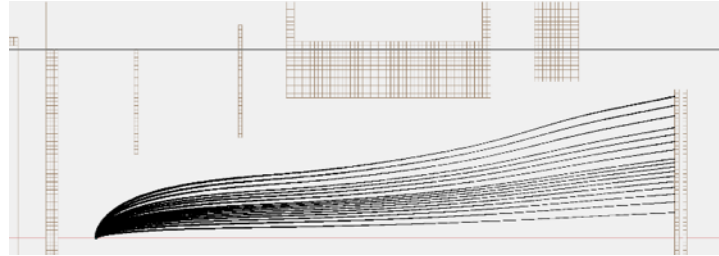


Figure 3.4: energy calibration of the VMI spectrometer with SIMION. Electrons with discrete kinetic energy are emitted perpendicular to the spectrometer axis.

On the other hand, in order to contrast the simulation, a physical process is used, creating electrons with a well-known energy, then above threshold ionization (ATI) of rare gas atoms is a suitable method to calibrate the spectrometer. The result of the ATI mechanism are several rings in the VMI along the laser polarization axis that are energetically spaced by the energy of one photon. With at least 2 rings visible it is possible to do the calibration with the following formula

$$\Delta E = \alpha(r_2^2 - r_1^2)$$

where ΔE is the photon energy, r_i are the peak positions of the Abel inverted rings and α the calibration factor. Best results are achieved by using as low peak intensities as possible, so tunnel ionization is suppressed.

Another method to calibrate a VMI spectrometer is the use of a narrowband laser in combination with resonant processes. A very useful scheme is published by Wituscheck *et al.* [76]. The scheme uses continuous 404 nm laser light to excite either the $5p_{3/2}$ or the $5p_{1/2}$ state in potassium. From this state, relaxation in four other states and the ground state is possible. The 404nm light can also ionize electrons from the resonant 5p state, the 5s, the 3d and the 4p states. The resulting electrons carry a very well defined kinetic energy $E_{kin} = E_{Photon} + E_{state} - E_{ionization}$. Since all energies on the right side of the equation are well known, the kinetic energy is also well known. This allows the calibration of the spectrometer with three points

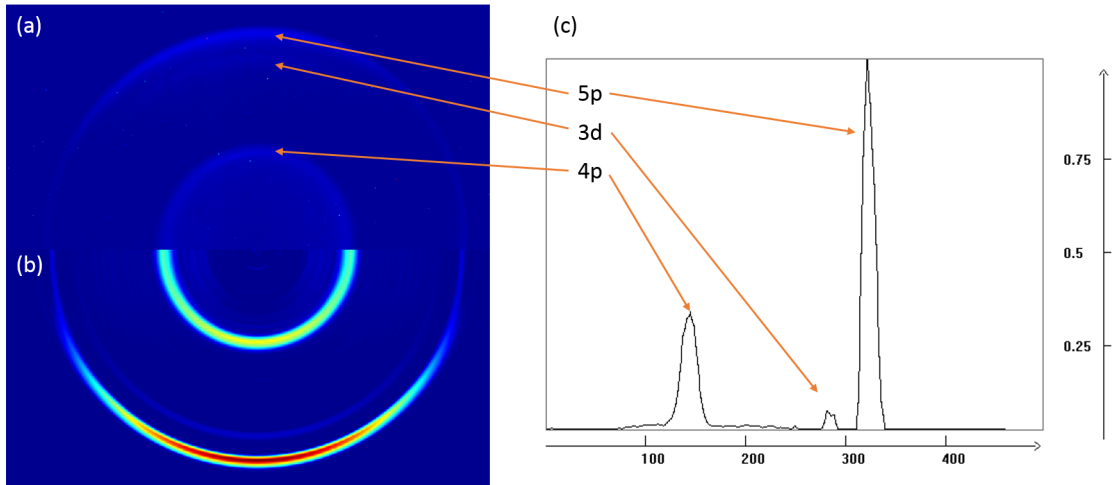


Figure 3.5: (a) Photoelectron image of potassium excited and ionized by linear polarized 404nm light, (b) Abel inverted image and (c) corresponding photoelectron spectrum, not yet calibrated on the energy

(the cross section of the 5s state is too small to see it) in the low energy range.

3.2.2 Laser intensity calibration

When using a focused MIR and NIR laser, it is essential to know the peak intensity in the focus of the laser field. Most of the time calculations give wrong results, because they assume a perfectly Gaussian shape and do not account losses in optics after the power measurement or an imperfect focus. So it would be desirable to avoid calculations and measure the peak intensity directly. In this thesis two different schemes are used, the $2U_P$ cutoff energy of electrons in a laser field [?], [2] and the ratios of charge states of ions produced in the laser field [5].

Assuming that the laser is a perfect Gaussian beam we can calculate with linear optics the Focused intensity. In cylindrical coordinates with the origin in the focus of the beam where z is the direction of propagation and r the distance from the z -axis one can use following equations to describe the intensity distribution of the beam:

$$w_0 = \frac{f\lambda}{\pi\omega} \quad (3.1)$$

where w_0 is the calculated focus depending on the focal length of the focused mirror f , the wavelength of the laser λ and the radius of the collimated beam before it is focused. the intensity will red as

$$I_0 = \frac{2P}{\pi\omega_o^2 R\tau} \quad (3.2)$$

where P is the power of the laser, R is the repetition rate and τ is the laser pulse duration.

3.3 Data Analysis

Due the complexity of the coulomb explosion, few analytical models exist in literature. the variables and parameter in which the nanoplasma depends are several and its analysis can be quite complicated. As shown above the individual signal tends to have a well defined circular shape that can be advantageous to our analysis, Fig. XXX show a picture of the normalized sum of one thousand signals of nanoplasma of helium at 10.6 K. On the left, the corresponding kinetic energy distribution after doing the inverse Abel transform in PbaseX software. As see, there exist a large combination of energy available along the plasma production and can be comparable to the most recent work of *Kelbr et al* XXX, where the electron spectra show similar values.

This large range of spectra for the averaged data and the defined circularity of the individual signal make us suspect that exist a energy dependence. Fig. 3.6 show a raw picture of single event and its Abel transform. The sharp peak in the electron spectra show a strong electron energy preference that change in each explosion. The peak in the energy distribution define the radius of the signal. To avoid doing the Inverse Abel transform for each individual picture, we create a event finder algorithm to identify and analyse each signal in the data sets. In this way we will detect and analyse the max energy distribution in the nanoplasma for the single explosion, and correlated to the electron yield given by the intensity of the signal.

In other words, Our result will be based in the finding and analysis of the Max radius and brightness of each individual bloop signal. The next section shows the event recognition scheme and the radius finder algorithm.

3.3.1 Event Recognition

The low event rate of the nanoplasma explosion results in a lot of empty VMI images. On average 10000 pictures were taken for each set of data where less than 10% of them contain signal. To separate empty images from signals, the central bright bloop is used. A center is selected manually and all pixels within a region around the center are summed up. If the sum is above a certain threshold value

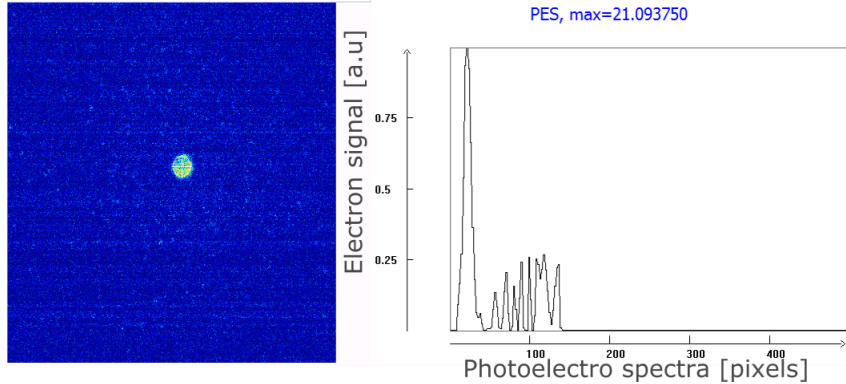


Figure 3.6: Example of the Inverse Abel transform for a single shot image. The photo electron spectra show the energy distribution of the signal with a peak in 21 pixels

the image contains a signal. To analyse the central feature in more detail the size and the brightness of this feature is of importance. To determine the radius and the brightness, two methods were compared, one using the Mathematica 10.1 (wolfram inc.) algorithms and the other using a binning processing.

First, the ImageMeasurements and Componentmeasurements algorithms in Mathematica act, over binarized images, works with arbitrary 2D and 3D images and computes multiple properties, finding components bases on a specific matrix. For this special case, a circular matrix with the specifications of minimum radius and no share edges were given as parameters. The efficient of this process was demonstrated to depend strongly on the initial image and the signal-noise rate, hence, a recursive function were develop to change the binarized threshold recursively until the algorithm find just one object that matches the signal. The threshold was changed progressively and modifiable steps in order to get the most precise fit. Once the object is found, the radius and center are saved, and sum the total intensity inside the radius, so a Radius-Brightness measurement is complete for each individual image.

The second method was based on a circular binning of the signal. A center for each data set is manually place after summed all signal pictures and find the center of the signal bloop, set to be in the same position within one measurement. Three circles are defined around this center, the first one with radius r (in pixels), which is variable, the second one with $r_{in} = r - \Delta r$ and the last one with $r_{out} = r + \Delta r$, where Δr has to be picked out from the dataset. The three circles define two areas A_{in} and A_{out} , see Fig 3.7. An average pixel value ρ for both areas is defined via

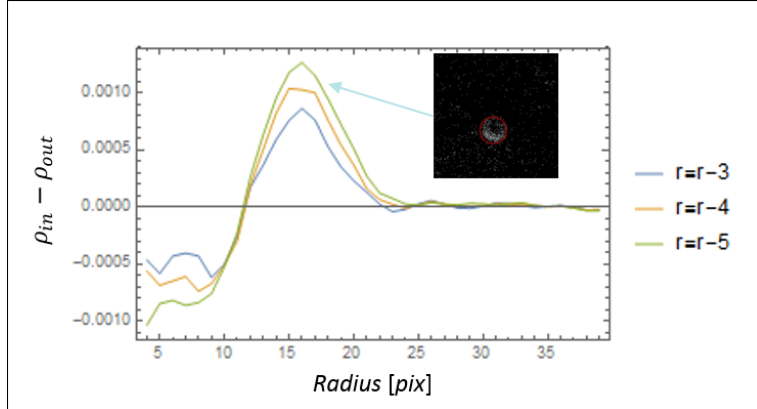


Figure 3.7: Difference of mean pixel values to determine the radius of the central feature in the VMI images

$$\rho_{in} = \frac{1}{N_{in}} \sum_{px \in A_{in}} \text{value}(px) - bg \quad (3.3)$$

$$\rho_{out} = \frac{1}{N_{out}} \sum_{px \in A_{out}} \text{value}(px) - bg \quad (3.4)$$

$$(3.5)$$

Where N is the number of pixels in the respective area and bg is a background taken far from the central features. The normalization on the area is important, because the areas are of different size. To finally find out the radius of the central circle, the difference $\rho_{in} - \rho_{out}$ is maximized, this is the case for the orange box in figure 3.7. For the green and the purple boxes $\rho_{in} = \rho_{out}$, which gives zero for the difference. Real signals do not have a perfect cutoff or a constant radial profile, which leads to noisy curves, when Δr is chosen too small, which makes the determination of r difficult. An example of a single shot image, where the radius is determined for $\Delta r = 3, 4, 5$ in pixels, is shown in figure 3.7. The VMI image in this figure has a donut shape, if the inner radius is of interest the same curve can be used to determine the inner radius as well if the minimum of the function is taken.

As shown in 3.7, the density difference have a summit in two cases, one when the inner our outer density changes signs. The lower peak, when exists, refers to the change from a low density change to a high one, besides the higher peak, describe the change from a high density to a lower, setting the radius where the edge of the bloop is pointing out that not all signals have the donut shape so this case was just added when needed. Finally, as in the last procedure, the inner pixels in the circle with radius r are summed and the radius-Brightness is save for all signal. In the case, as

the example, where the second inner circle is clearly identified, the sum of all the pixel discard the inner are, and at the same time, adds the inner radius-brightness measurements to it. Fig 3.8 shows a raw image where the inverse Abel transform and the Binned Finder algorithms where compare. The signal shows a clear edge where the peak electron signal (PES) of the Abel transform is at 58.6 pixels, while a similar curve is described by the density binned plot of the Finder algorithm at 60 pix, given a good agreement between the two techniques. Figure 3.9 shows a set of well fitted radius for each signal, proving the good efficiency of the algorithms.

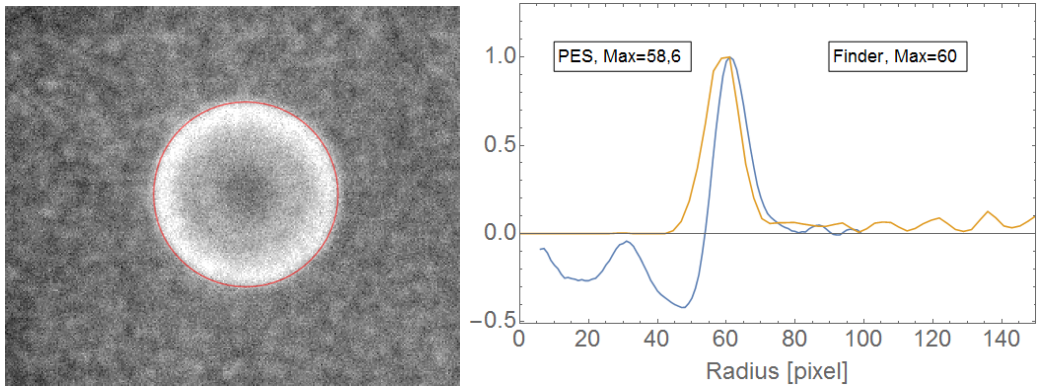
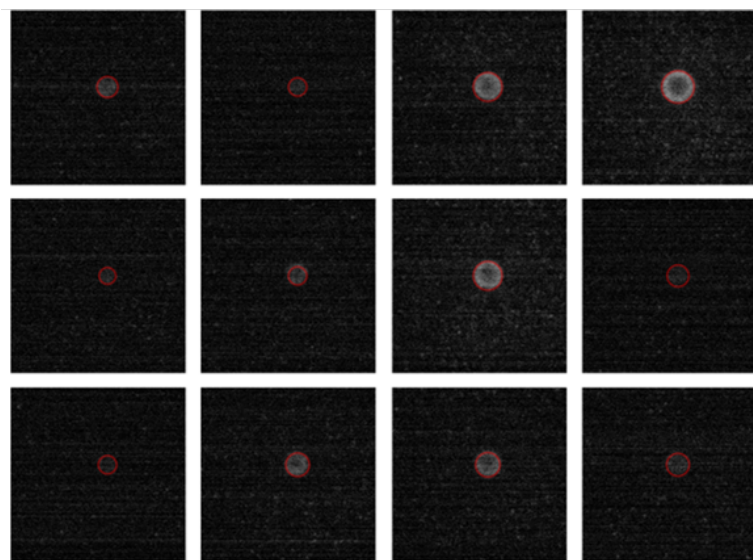


Figure 3.8: On the Left, example images of MIR VMI signal. On the right, the correspond Inverse Abel transform PES (orange) and the Bloop finder density plot (blue). Both algorithms show a peak at radius of the circular signal, highlighted in red. The density plot also shows a second depletion close to 45 pixel that give extra information as the radius of the inner less brighter ring.

Figure 3.9: Example of random signal images fitted to its corresponding radius.



Last, once the radius-brightness data is recorded, and the calibrations are set,

the system can be compare to the model explained above, where radius can be converted into maximal kinetic energy, $r \rightarrow k_{energy}$, and brightness to number of electrons, $b \rightarrow N_{e-}$.

3.4 Coulomb Explosion Model

As seen in the the previous section, the electron energy distribution may have a big dependence on the maximal energy reached in the coulomb explosion. In order to give an analytical background, the next section explain a simple model based on the work of *Ranaul Islam et al.* [35], Where describes a ions energy distribution based on the ions laying in a ion uniform charge spherical cloud.

3.4.1 The Islam et al. Model

Once the ionization process started, an electronic cloud of quazifree electrons will be created around the remaining cluster. This is a complex physical process due its chaotic system determined by the individual velocity vectors of the particles and their interaction between the Electric field, the cluster and each other. Various theoretical approaches ranging from phenomenological models [15] to large-scale microscopic calculations [60] have been done but far for been interpreted to clusters and system with more than a few thousand of particles, with out taking into account that almost always, considered theoretical scenario of a single well-characterized cluster, irradiated by a laser pulse of a given intensity is usually far from the real experimental situation. As an analytical solution is far from been formulated, we work joint to the theoretician Andreas Hidenreck to make computational simulations. This are demanding simulations that takes a large of computational power even for small cluster, but as show in its group, the results can recreated reasonably the experimental system and so give a better background to the understanding of the plasma formation.

Another, more simple and intuitive approach is done by *Ranaul Islam et al.*, in [35]they try to express the kinetic energy distribution for an ion cloud and we will adapt to electrons to relate them to the VMI images. Two important assumptions are made for this model. First, we assume a uniformly charge distributed spherical cloud with radius R and density $\rho = N/vol$ where N is the number of particles inside the sphere, furthermore all the particle lays with zero kinetic energy. Second, The basic mechanism underlying the kinetic energy distribution in clusters is their Coulomb explosion, it converts the potential energy E_{coul} of a partially ionized cluster atom

at a distance r from the cluster center into kinetic energy E . The probability dP/dr to find an atom at a distance 4 from the cluster center is then given by [35]

$$\frac{dP}{dr} = \frac{3r^2}{R^3} \Theta(R - r) \quad (3.6)$$

where, $\frac{dP}{dr}$ is the probability to find an electron at radius r and Θ is the step function for the particles inside the radius of the sphere, with homogeneous charged density, we have N particles with a charge of q and just after the are ionizes they have not moved yet, then the potential Coulomb energy of an particle inside the cluster is given by

$$E_{coul}(r) = Ne^2 \frac{r^2}{R^3} \quad (3.7)$$

for $r \leq R$. N is the number of electrons in the sphere and e is the elementary charge of an electron. A charged sphere like this will immediately coulomb explode and for $t \rightarrow \infty$ all coulomb energy is converted to kinetic energy, which can be measured experimentally with the VMI. It is possible to retrieve the energy distribution out of the spatial distribution 3.6 with 3.7 as the substitution formula.

$$dr = \frac{R^3}{2Nq^2r} dE \quad (3.8)$$

Furthermore, we define the maximum coulomb energy

$$E(R) := E_R = Nq^2 \frac{1}{R} \quad (3.9)$$

with all this follows the energy distribution of the electrons

$$\frac{dP}{dE} = \frac{3}{2} \sqrt{\frac{1}{E_R}} \frac{1}{E_R} \sqrt{E} \cdot \Theta(1 - \frac{E}{E_R}) \quad (3.10)$$

it can be seen, that the energy distribution is fully characterized by E_R , so it is enough to know the maximum kinetic energy, which is just the radius of the central feature in our VMI images. With this even the inverse Abel transformation can be bypassed, because the edge of a sphere is invariant for projecting the sphere on a plane.

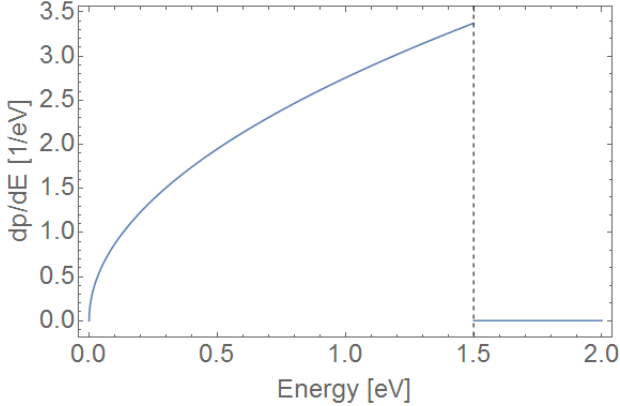


Figure 3.10: Energy distribution for a coulomb explosion of a full sphere of electrons according to formula 3.10. The dashed line marks cutoff energy E_R

With the formula for the homogeneous density in a sphere

$$R = \left(\frac{N}{\frac{4}{3}\pi\rho} \right)^{1/3} \quad (3.11)$$

and formula 3.9 the charge density in the beginning in the process can be derived to

$$E_{max}(N) = \underbrace{\frac{e^2}{4\pi\epsilon_0} \left(\frac{4}{3}\pi\rho \right)^{1/3}}_{=:B} N^{2/3} \quad (3.12)$$

and with this the charge density reads

$$\rho = 48\pi^2 \frac{\epsilon_0^3}{e^6} B^3 \quad (3.13)$$

In summary, the charge density can be calculated with the fit parameter B or B-factor as we will named from now on. B can be retrieved by plotting the maximum kinetic energy E_R as a function of the number of electrons N . Both can be extracted out of the VMI images, E_R from the radius and N from the brightness of the central feature.

4 Results and Discussion

As mentioned, this experiment was performed in two laser facilities. At The Extreme light Infrastructure beamlines ELI-ALPS in Szeged, Hungary, and at the Max Plank institute for nuclear physics in Heidelberg, Germany. In this chapter we will present the results of different experiments in an individual way, finalizing with a comparison of HE cluster in the two different laser fields (MIR and NIR) and Ne and He at the MIR laser. As above, all data were selected and treated as single nanplasma explosions signals, with independent calibrations.

In the first part of the chapter we will present the results for Helium cluster under NIR field. The Experiment was done in Heidelberg with a Ti-Sr 800nm wavelength laser. An intensity scan, Droplet size dependence and Xe doping dependence are introduced. The second section will show the results of Helium clusters under a 3200 nm wavelength (MIR) in Szeged, where we make measurements of cluster size dependence, Xe-Ca doping scans, Ar doping scan, water doping scan and pulse duration scan. Finally we present the results at the second beam time in ELI, similar experiments were performed with the same laser but with Neon as cluster source. Measurements of Cluster size dependence, Pulse duration Scan and Xe doping scan were also performed. For additional information about the laser system used in each of the Beam lines, we recommended to the reader to find the detailed characteristics in the next links, [68].

Fig. 4.1 shows an example of some background subtracted electron-VMI raw signal. From now on, we will refer electron-VMI just as VMI. On fig. 4.1 d. shows one of the outline founded in the bigger explosion where the He signal presents few electrons with low energy, given it a ring shape that we will denominate "Donut" shape. The helium and neon signals present quite similarities, except for the donut shape. The signal radius along a data set changes constantly and each individual signal need to be analyzed independently. In general parameters as the voltage in the system and the wear and tear of the detector also needs to be taken into account. Non Abel transform is necessary because we will deal with the maximum energy distribution only, and just to detect the radius in the signal is suitable. The distribution of radius and brightness in the images will be translated to an Energy-

Numb Electrons distribution, in order to get some information about the density and reachable energy in the coulomb explosion, as show in the next sections.

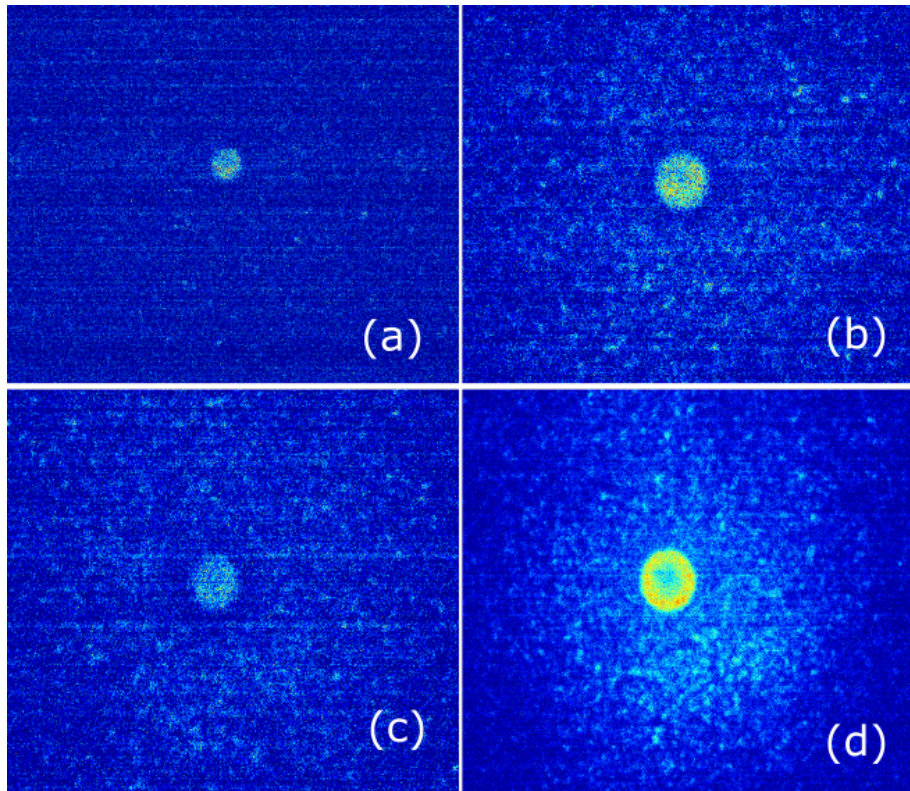


Figure 4.1: Example raw images of VMI for the droplet size scan from one data set. Images a, b and c present different size and intensities but a uniform circular shape while figure d, presents a "donut" shape.

4.1 Helium nanoplasma under NIR Fields

As presented on the experimental setup, we can modify several parameters to perform different experiments in order to understand better the nanoplasma process. The cluster can be created, at different nozzle temperatures, given different droplet sizes. He can be doped with one or two dopant at different densities varying the pressures of the dopant gas or the temperature of the oven. Finally the cluster will be ignited in a coulomb explosion due the femtosecond laser pulse and the electrons will be detected by the VMI and the Ions will be detected by the TOF.

In the next sections, special attention will be taken on the VMI results due the amount of information it can deliver. The TOF data, is analyzed in an independent way, but will not be part of the main results. The data done in Heidelberg were already analyzed in the master thesis of Nicolas Rendler and the information can be

Power[mW]	Laserintensity[W/Cm ²]
11	6,27E13
25	1,425E14
55	3,135E14
80	4,56E14
115	6,555E14

Table 4.1: Laser focused intensities calculated for different Powers

found in [58]. The main purpose to re-evaluate this information is to compare the experiments with similar parameters to the ones used in ELI-AlPS.

Using the "Xenon ion charge" intensity calibration, on the NIR laser they obtained table 4.1with the corresponding to the focused intensities depending on the power. The laser power was measured just before the beam enters to the detection chamber and was compared also to the theoretical calculations for the optical system mounted as shown in Fig. 4.2. As we could observe, the signal rate in each data set depends on the intensity at the focus, for the nano plasma a minimum field energy is needed to start the ionization on the dopant and hence, start the coulomb explosion. In order to have the best results and high data acquisition, we worked at maximum intensity near 55mW, so we can ensure the good quality of the ignition process and hence its efficiency.

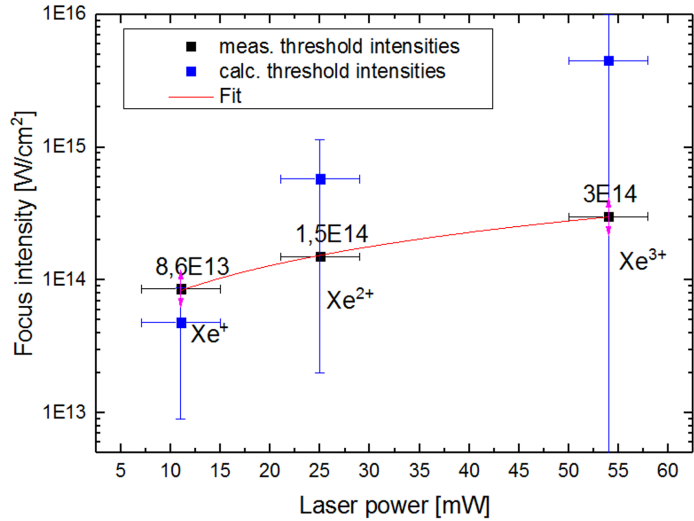


Figure 4.2: Xenon ion charge calibration for NIR laser at three different power. On Blues the calculated threshold intensities and on black the experimental results for the power measured before the laser beam enter to the detection chamber.

4.1.1 NIR. He Droplet Intensity scan.

The laser system used at the Max plank instituted is a NIR laser at 800nm wavelength and a rate of 10Hz and a $d_{pulse} = 23\text{ fs}$ pulse duration. Helium clusters at the same nozzle temperature $T_{nozzle} = 12.2\text{ K}$ and backing pressure of $P_0 = 45\text{ mbar}$, were doped with Xenon at a fix doping level, with the a constant pressure measured in the oven chamber of $P_{oven} = 2E - 6\text{ mbar}$. This measurement where taken with a slightly smaller MCP-PHS arrangement of $d = 42.2\text{mm}$ diameter of active area. At this nozzle temperature the Helium droplet have proximate $N = 397390$ atoms before going through the oven chamber and its doped with $Xe_{dop} = 134$ atoms, given a final number of He number of $N = 386596$ atoms. The VMI voltages where set to VMIx2 and the MCP and PHS to 1250 V and 4000 V respectively. The camera was stablish to exposure time of $t_{exp} = 1\text{ ms}$. 50000 pictures were taken for 7 different laser power, at $55, 80, 115, 140, 185, 210$ and 240 mW .

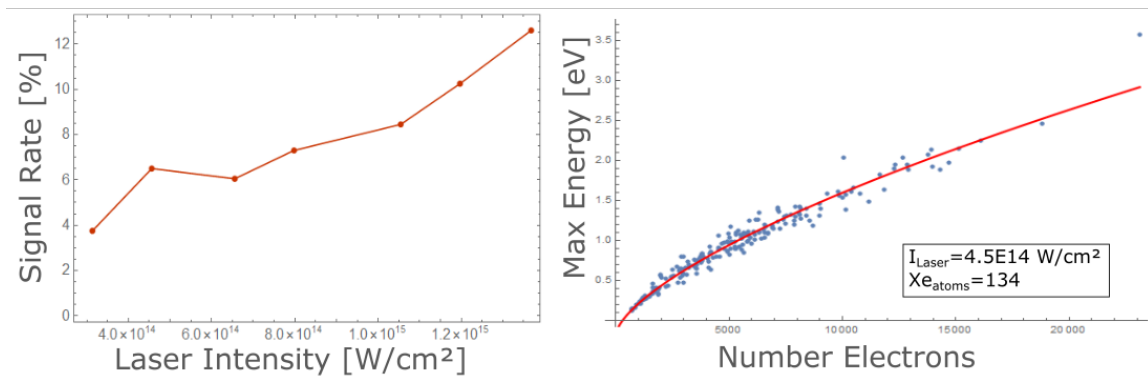


Figure 4.3: On left, signal rate for Helium droplets at different focus laser intensities. On the right the energy distribution of the droplet at 80 mW Laser power.

As show on Fig. 4.3, the signal rate depends strongly on the laser intensity, but even at lower intensities some coulomb explosion can be found. Although the percentage of pictures with signal decrease remarkably, we never find zero signal, it means that we have enough initial ionization to start the coulomb explosion. Despite the changing signal rate, we compare the Energy distribution depending on the number of electrons, a clear distribution on all signals is shown. In fig 4.3, each blue point represents a individual picture, where the radius and brightness of each signal bloop is identified. Once all signal are analyzed, the distribution is plotted and fitted. The red line, is a fit based on $E_{max} = B \cdot n^{2/3}$, Eq. 3.12 where B is the B-Factor named on Eq. 3.13 and n is the number of electrons, the $2/3$ factor is fix. The same process is done for each of the data sets at different laser intensities. All fits have the same tendency regardless the laser intensities, changing slightly on the B-factor. This in an important outcome meaning that the data fits quite well

to our simple spherical electronic cloud model. As the B-factor is directly related to the density of the electronic cloud using Eq. 3.11 is possible to delimit the radii of the electronic sphere. In other words, according to this model, if we know the total number of electrons it's possible to calculate the maximal energy that we can detect.

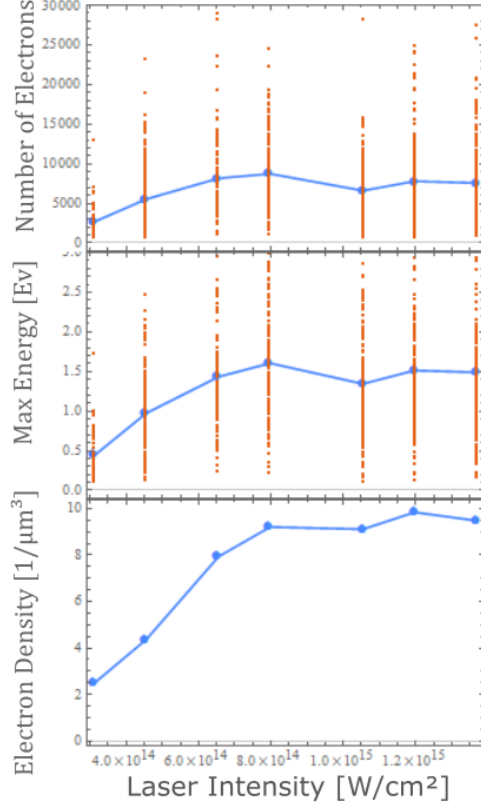


Figure 4.4: On top, Mean number of electron for each of the data set at different laser intensities, on blue the mean values and in orange the individual results. On the center, mean value of the Max energy for different laser intensities. At bottom, the density (calculated from the B-coefficient) for the fit done in each of the data set.

According to fig 4.4, the mean number of electrons and the mean E_{max} , reach a maximum after $I = 8.5 \times 10^{14} \text{ W/cm}^2$ and keeps comparably constant for the following intensities. This result is not surprising because we don't expect large differences on the energies reached after the system is fully ignited, suggesting that after the beginning of the process, the coulomb explosion keeps a constant behavior. Fig 4.4, bottom plot, shows the density of the electronic cloud, it is calculated from the B-factor of each fit function. It concur with our previous assumption, it exhibit that there is a limit density that is not affected after certain intensity. Two assumptions can be done. First, the laser intensity play a fundamental role in given the starting

NIR Helium Cluster Size (Ref)			
$T_{Nozzle}[K]$	$N_{He\text{dop}}$	$N_{Xe\text{atoms}}$	$N_{He}[\text{atoms}]$
20	32671	66	27362
16	108424	199	92432
14	222264	189	207173
13	331040	149	319084
12	509035	160	495949

Table 4.2: NIR Helium Cluster Size

condition to the nanoplasma formation but after a threshold, the laser does not influence in the final coulomb explosion any more. Second, a clear density limit is shown, it is possible that it is influence by this limitation of the laser on the process, but mostly it can be limited by the droplet size that was used in the experiment, as consequence, the biggest droplets are all expanding so in order to find bigger energy and densities we should use lower nozzle temperatures.

4.1.2 NIR. He Droplet size dependant.

For this data set, helium clusters at different nozzle temperatures, were doped with Xenon, with a doping pressure $2E-6$ mbar measured in the doping chamber. The VMI were set to VMIx1 voltages and the MCP and PHS to 1250 V and 3400 V respectively. The camera was set to $\tau_{exp} = 1$ ms exposure time. 50000 pictures were taken for 5 different temperatures, at 12.5 K, 13 K, 14 K, 16 K and 20 K. The data were analyzed using the data processing mentioned in chapter 3 to convert the bloop radius and its inner brightness to Maximal energy E_{max} and Number of electrons $\#e-$. Using the Hagena scale [29], we can calculate a prediction of the total number of atoms before and after the doping. Table 4.2 shows the mean number of atom per cluster to at the different nozzle temperatures and also its corresponding number of dopant.

Fig. 4.5 shows the corresponding signal rate depending on the nozzle temperature. As shown, the biggest droplets contain the highest percent of signal compared to the small droplets. We need to take into account that the difference in size helps to the ignition of the process due the cross section for the interaction with the laser field also increase, so the ionization is easy. Furthermore, the larger the number of atom in the cluster the most electrons available to be detected. Once identified the radius and brightness of all the pictures, a Energy distribution is plotted. Fig 4.5 right, shows the energy distribution for the droplets sizes at 12.2 K. Each blue point represented a single picture, with the bloop radius and brightness transformed

to energy and electrons. The red line, is a fit based on Eq. 3.12 where B is the B-Factor named Eq. 3.13 and n is the number of electrons, the $2/3$ factor is fix to the fitting. The same process is done for the other nozzle temperatures, the fits have the same tendency for different droplet sizes and don't differ much between each other. For the B-factor at 12.5 K the corresponding electronic cloud density is around $\rho = 2.2[1/\mu\text{m}^3]$, what leads to a electronic cloud radius of $4.3 \mu\text{m}$.

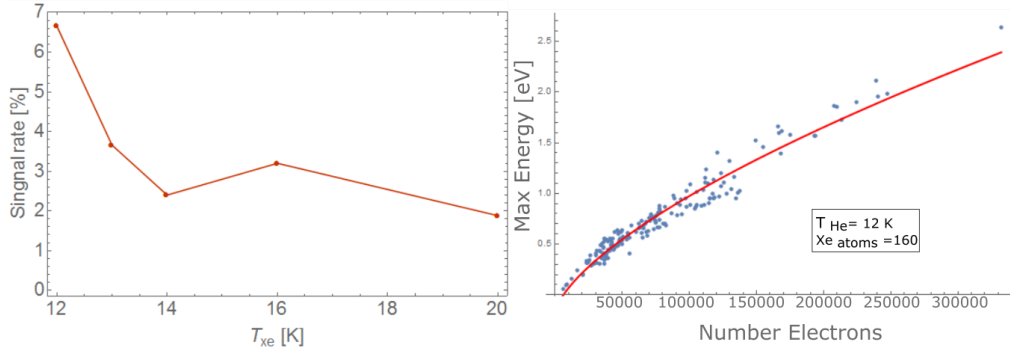


Figure 4.5: Signal rate and Energy Distribution for Helium droplet size scan. On the left, the signal rate for the different nozzle temperatures and on the right, an example of the energy distribution of the data set and its corresponding fit line.

Figures 4.6. Shows the Mean #e- and E_{max} values for each size with their corresponding histograms. Hence, for example at 12 K, the energy histogram shows that exist counts for high energetic explosion, up to 4 eV, but the mean value of all the data is not higher than 2 eV. This behavior is also present for the other nozzle temperatures, where there exist a broad distribution for 13, 14 and 12 K, and presents a clear peak in the beginning of the plot for the higher energies. Moreover, the number of electrons in the system also rise with the size, for $T = 12.2$ K the mean number is close to 160000 electrons, almost 10 times bigger than the smallest droplets. Similar as above, the 3 lower temperatures have a broad distribution than the smallest droplet, who show a peak at 10000 and 30000 electrons respectively. These results not just show that effectively, we are reaching different droplet sizes, but also that at these laser intensities the Coulomb explosion is possible regardless the droplet size. At the same time, showed that there are different droplet sizes and they form nanoplasma, so there is no doubt that their densities do depend on the Coulomb explosion and the B-factor keep relatively constant, so the Energy for this NIR laser can be described by the density on it.

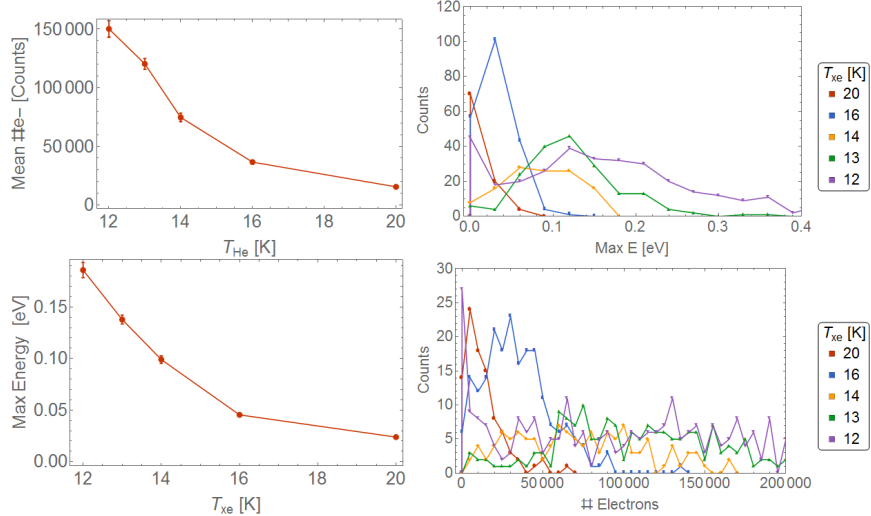


Figure 4.6: Mean Values and histogram for the droplet Size scan, on left the mean values for the different nozzle temperatures and on right, the respective Histograms counts for the binned data.

4.2 Helium nanoplasma under MIR Fields

Similar as the section before, Helium nano droplets doped with different alkalioids are described. Helium was expanded from a nozzle of $5\mu m$ opening at a backing pressure of $P_0 = 30bar$, using different nozzle temperatures to produce a jet of helium nano droplets. This beam is doped by a Xenon gas, when passing through a gas doping cell in the doping chamber or Calcium atom when it pass through the oven. Therefore, the mean dopant cluster size is determined by the xenon pressure in of the gas doping cell, which is controlled by a high-precision needle valve and the oven temperature. The flight distance through the gas doping cell is $30mm$. The MIR laser pulses are orthogonal to the cluster beam through a vacuum window into the chamber and focused into the cluster beam by a focusing mirror. The laser intensity in the focus during the measurements was in average $2.5E14 W/cm^2$ at a maximum power of $P \sim 9 W$, it had a minimum pulse duration of $t_{pulse} = 45 fs$ and a rate of 10 KHz. The laser power depends on the pulse duration because the total pulse energy needs to be distributed on time, in each specific case we will denote the power when it changes. The polarization of the laser field was orthogonal to the spectrometer axis. The electronic signals were recorded with the Basler CCD camera at a minimal exposure time $t_{Exptime} = 45\mu s$ triggered with the TOF as explained in chapter 3, this process grants the single shot signal. The camera is focused on the MCP-PHS arrange that makes the electron signal visible.

Because, in general, not all laser shot hits a cluster or generates a plasma explosion, most of the data sets presented next have a low signal rate, in order to have

representative statistics, in each experiment were taken 10000 pictures, from those, about less than 10% had signal. Most of the VMI signal had the expected circular aspect except for the larger size droplets, with the donut shape.

The data identification and process follows chapter 3, and in case of the donut shape pictures, this data were analyzed independently. In each signal picture the maximum blob radius and its respective inner brightness are identified and transformed into number of electrons and max energy. Each set of data is different, so once we analyses all the pictures a distribution function can be plotted.

4.2.1 MIR. Helium Droplet size dependence.

For this data set, He clusters at different nozzle temperatures, were doped with Xenon at a pressure of 0.0060 mbar measured in the gas doping cell. The voltages were set to VMIX1 and the MCP and PHS to 1600 V and 4000 V respectively. The camera was set to minimum exposure time and the trigger system was used. 100000 pictures were taken for 4 different temperatures, at 10.6 K, 11 K, 12 K and 12.5 K. The data where evaluated once more as last section, demonstrating that the Trigger system worked efficiently. As result, it was shown that even for this high repetition laser rate, single shot signals can be achieved. The TOF signal work as a reference to identify the single explosion, and then each individual VMI picture is treated as follows. Fig 4.7 shows a mean TOF for the measurement at 10.6 K. As we can see, there is a large amount of water and a small peak for hydrogen still in the vacuum chamber, this remain gases affect especially for the background. It is shown that Helium is effectively ionized due the peak at He^+ but on contrast no He^{2+} signal was identify.

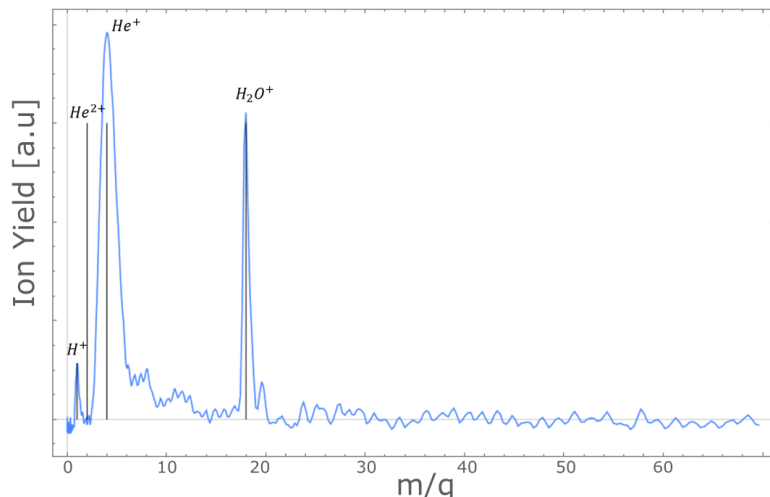


Figure 4.7: Mean TOF spectra for He at 10.6 K

Cluster Size reference		
T_{Nozzle} [K]	$N_{Xeatoms}$	$\langle N \rangle_{Heatoms}$
10.6	220	2.80E5
11	192	2.29E5
12	138	1.42E5
12.5	119	1.13E5

Table 4.3: cluster size reference

Using the Hagena scale [29], we can calculate a prediction of the total number of atoms before and after the doping. Table 4.3 shows the mean number of atom per cluster to at different nozzle temperatures and also its corresponding number of dopants. As reference for the cluster size scaling law, we used data at $P_0 = 50$ bar and temperatures similar to the experiment.

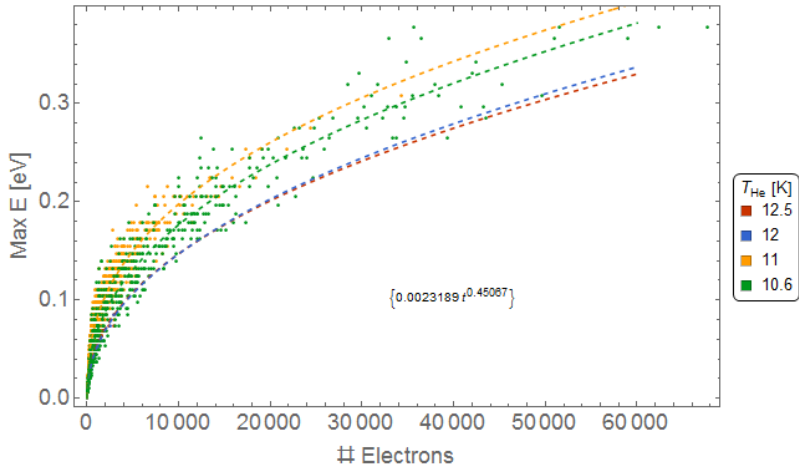


Figure 4.8: Maximal Energy distribution on the number of electrons. On colors the different nozzle temperatures, the smallest droplets (12 K,12.5K) presents few signal images and can be seen behind the yellow and green points in the left-bottom of the graphic. The dash line are the fit curves.

Fig 4.8 shows the energy distribution versus the number of electrons. As we can see, most of the data point lay on the bottom-left of the graph at lower energies, but the distribution also show signals with energies up to 0.4 eV and 50000 electrons collected, this signals comes from the most energetic coulomb explosions, and we can clearly see that the bigger the droplet the brightness we can get. Due the few signal for the 2 higher temperature we discard the 2 fit lines, moreover, for the others, its fit lines are in a relatively good concordance to the data using Eq. 3,13 as a guide, we find a B-factor $B = 0.00305103$ and a factor $k = 2/5$.

On one hand, the first big different with the experiments with the NIR laser, is this non correlation to the uniformly charged Cloud model, especially in the

exponent k , that changes from $1/3$ to $2/5$. There is no theoretical background that can predict this behaviour but as the exponent is closely linked to the geometry of the cloud, we can assume the fits does not agree because the big droplets are not perfectly spherical, so for example, as they are liquid, the droplets could turn in an ellipsoidal. This new exponent is persistent in all the fit for the MIR experiments in helium. On the other hand, as explained, the B-factor is directly related to the density and in consequence to the radius of the electronic cloud. Given B, we obtain approximately $R_{cloud} = 85 \mu\text{m}$, a radius three order of magnitude bigger than the initial cluster, that for example at 11 K have $R_{cluster} = 13 \text{ nm}$.

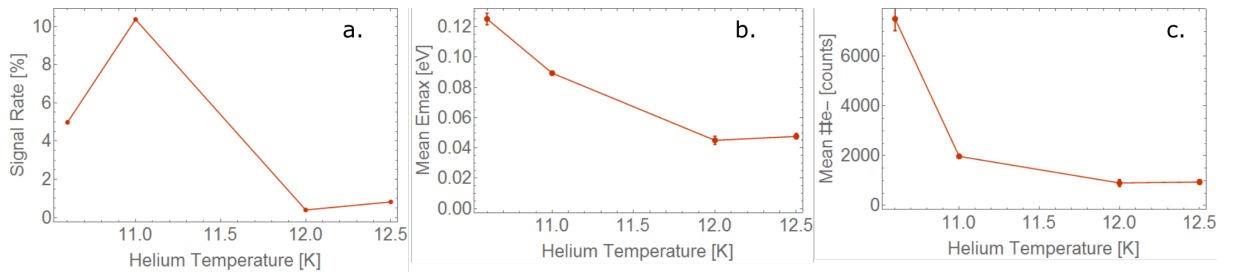


Figure 4.9: Figures a, shows the signal rate in percentage of the pictures with signal depending on the nozzle temperature, B and c. show the mean of the number of electrons and the Max energy for each point respectively.

Fig 4.9 presents the Signal rate and the Mean values for the number of electrons and max energy depending on the temperature of the nozzle. As shown the figure, for the biggest droplet (points to the left) we got the largest signal rate at 10.6 K and 11 K and immediately for the smaller droplet the rate decrease drastically, same tendency is show b and c making clear that plasma is easier to ignite at lower temperatures. Therefore, as more electrons and energy are detected while the signal rate increase, we assume that the nanoplasma formation is more efficient for larger droplets. The drop on the signal rate at 10.6 K compared to the 11 K can evidence a loss of efficiency for the laser to ionized even bigger droplets. In other words, After certain droplet size, is more difficult to ignite the plasma. Unfortunately, no other measurement where taken at lower temperature to confirm if this is a statistical event or a real tendency.

Fig 4.10 shows the histogram of the E_{max} and $\#e-$ for the different temperature. On one hand, in the E_{max} , the first peaks describe that most of the droplets achieve energies between 0.05 and 0.1 eV, decreasing rapidly after that. On contrary, the biggest droplets have a more broaden distribution that the higher temperatures. One interesting feature is that there exist an offset from zero energy for all temperatures which can be related to a minimal energy needed to ignite of the plasma autonomous of the cluster size. Furthermore in the $\#e-$, a broader distribution is show, a huge

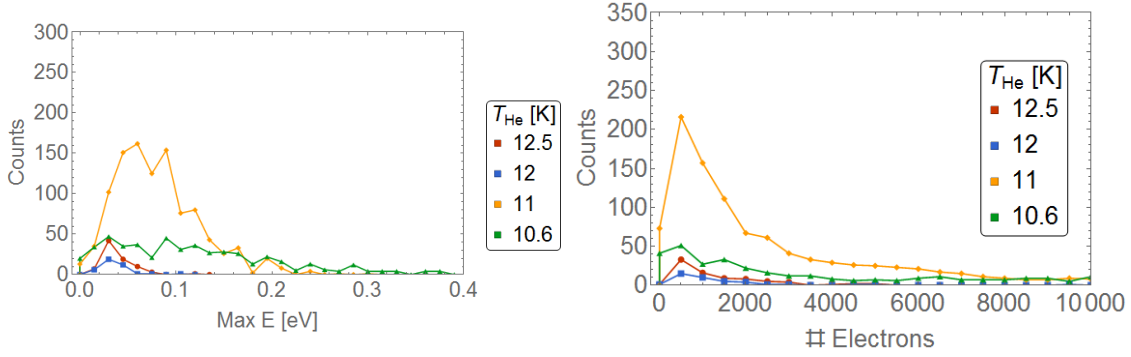


Figure 4.10: On the left, The histogram for max energy and on right, the histogram for number of electrons.

density is found for droplets with less than 2000 electrons, having a drastic decrease. It shows a clearly distribution where the main average size of the droplet is small, but without discarding that some individual points at a huge number up to 80000 e^- , this shows that at bigger droplet also the high chance to have more populated electronic clouds.

4.2.2 MIR. Helium-Argon doped.

In this data set, He clusters were doped with Argon at different gas doping pressures. Helium was produced at a nozzle temperature $T_{nozzle} = 11$ K and ignited by the MIR laser pulse, the VMI were set to VMIx1 voltages and the MCP and PHS to 1700 V and 4000 V respectively. The camera was set to $t_{exp}=50 \mu s$ exposure time what means the data was not correlated with the same trigger. The exposure time was modified due the low signal rate, nevertheless the information will be still evaluate in the same way as before, taking into account that signal rate was so low that is possible to have single shot. 100000 pictures were taken for 3 different doping pressures, at $2E - 4, 6E - 4$ and $12E - 4$ mbar measured in the gas doping cell.

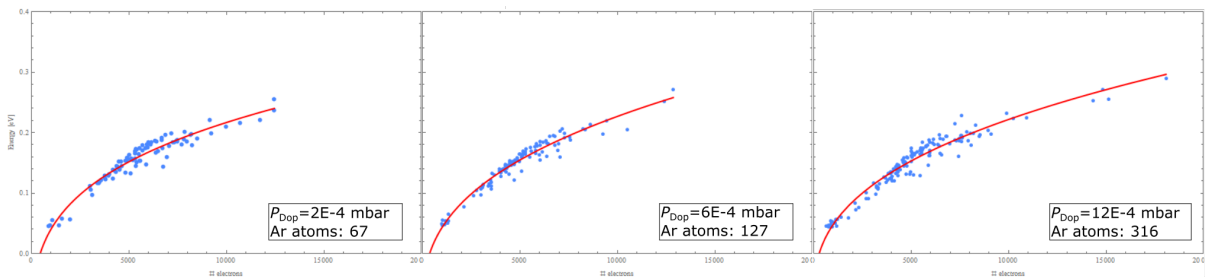


Figure 4.11: Energy distribution for He cluster at different Argon doping levels

Fig 4.11 shows the maximal energy distribution for three different pressures and its corresponding number of dopant. As mentioned, the signal rate for this data

set was quite low showing that the efficiency for this doping is lower than for Xe. In red the fit done with the same fitting parameters than above with a B factor $B = 0.09714$ what gives us a mean radius for the electronic cloud of $R_{cloud} = 92.4 \mu\text{m}$, quite proximately in the same order of magnitude to the data set above. For the Exponent, it was set as a free parameter given in general $k = 2/5$ as well.

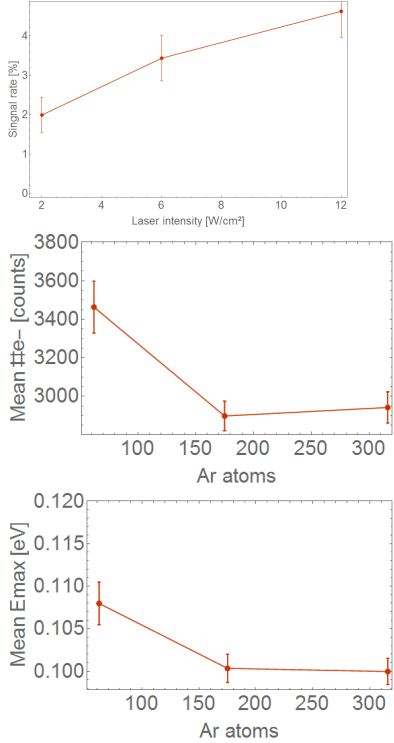


Figure 4.12: On the left, the signal rate for the He-Ar doping. Center and right, are the mean values for the number of electrons and max energy respectively

Fig ?? shows the signal rate and Mean values for the data. On the signal rate is clear that the amount of dopant increase the efficiency of the plasma, going from a low rate up to 5%. Combined to the Mean values results, we can deduce that the efficiency for small droplets ignition also improve at higher doping. As seen before, the mean values for number of electrons and energy decrease while the signal rate increase, evidencing that there are more small droplets explosion detected.

4.2.3 MIR. Helium-Water scan.

The Nanoplasma explosion process starts when the dopant gives electrons to the cluster in order to ignite the plasma. One of the most commune and available dopant is water, not just because it's easy to get in the lab but also because it's also difficult to remove from the vacuum chamber. Even in our best vacuum, experiments usually

contained few traces of water. In addition, at Mid-Infrared, water have a special resonance that could be advantageous because it will withstand a faster ionization and in consequence, a better creation of the plasma. This data set was taken with He droplets at $T_{nozzle} = 11$ K doped with water. A small drop of water were located into the entrance of the needle valve, to achieve a controlled doping. The pressure at the gas doping cell was varied in order to perform several doping levels. The camera was set to $t_{exp} = 120$ ms so single shot was not enable. The voltages were set to VMIx1 and the MCP and PHS to 1750 V and 4000 V respectively. 100000 pictures were taken for 5 different doping pressures, at $1E-4$, $2E-4$, $3E-4$, $6E-4$ and $12.5E-4$ mbar.

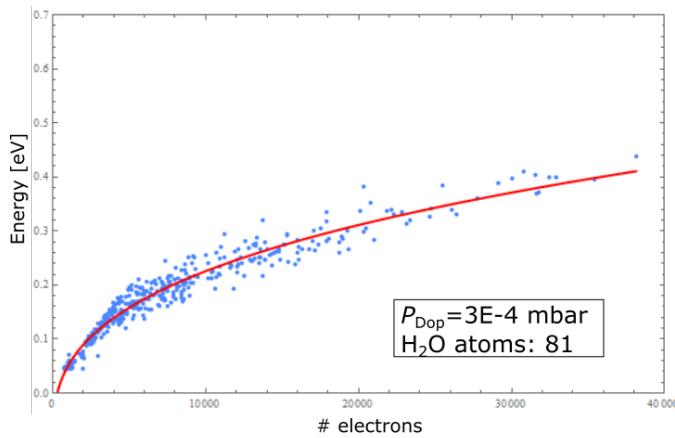


Figure 4.13: Plot of the E_{max} and $\#e-$ distribution for He doped with water at 0.00120 mbar, on red the fit for the point.

Fig. 4.13 shows the energy distribution for just one of water pressures. On blue are the points that represent the E_{max} and $\#e-$ for an single signal picture and on red the fit based on the Eq. 3.12. For the water doping pressures the distribution looks almost the same, just changing in general the signal rate as shown in Fig. 4.14. The fit function is used to find the B factor, obtaining for this example $B = 0.01509$, that gives a radii for the electron cloud of $R_{cloud} = 92.4\mu\text{m}$, with an exponent factor $k = 2/5$.

Fig ?? presents the rates for signal as the Mean number of electrons and max energy depending on the temperature of the nozzle. As shown, for the biggest droplet (points to the left) we got the largest signal rate at 10.6 K and 11 K and immediately for the smaller droplet the rate decrease drastically, same happens in the mean signals where the biggest droplets are the once that reach the higher counts. The measurements show that with decreasing nozzle temperature, therefore increasing droplet size, the frequency of single-shot signals increases, and higher kinetic energies can be detected.

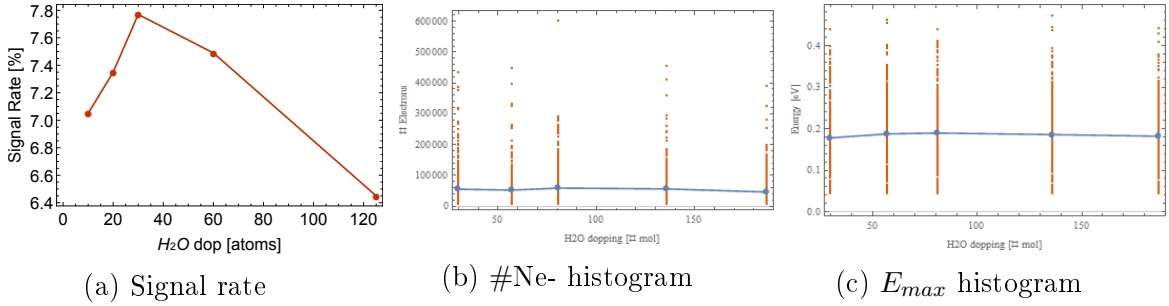


Figure 4.14: On left, the signal rate for the He-water doping, B. and C. are the histogram of the point for the main number of electrons and energies respectively

As we show, under the correct doping levels and He cluster sized, water molecules are a great dopant for Helium clusters under MIR laser pulses. The nanoplasma reach high energy states as well as a huge radius for the electronic cloud, reaching mean of electrons detected up to 70000. The mean values in the energy or electrons does not depend on the doping, as already described in the other experiments, once the ionization process ignites the plasma the final result does not present variations.

4.2.4 MIR. Helium-Water Intensity scan.

Similar to the experiment done in Heidelberg with the NIR laser pulse. A intensity scan was performed in order to see the effects of the laser system on the coulomb explosion. The laser system used at ELI-Alps is at 3200 nm wavelength and a rate of 100 KHz and a $\tau_{pulse} = 45$ ps pulse duration. Helium clusters at the same nozzle temperature $T_{nozzle} = 11$ K and backing pressure of $P_0 = 30$ mbar, were doped with Water at a fix doping level $P_{dop} = 1E - 4$ mbar pressure measured in the gas doping cell. At this nozzle temperature the Helium droplet have proximate $N = 244647$ atoms before going trough the oven chamber and its doped with H₂O_{dop}=56 atoms, given a final number of He number of $N = 215972$ remaining atoms. The VMI voltages where set to VMIx1 and the MCP and PHS to 1750V and 4000V respectively. The camera was stablish to exposure time of $t_{exp} = 34\mu s$. 100000 pictures were taken for 6 different laser power, at 2, 4, 6, 7, 8 and 9.5 W, measured before the laser beam enters to the detection chamber and its back focus by the mirror.

Having the laser power, the intensity can be calculated for each laser power using the Xe cut off calibration. The legends in Fig.4.17 shows the different laser intensities calculated for each of the laser power used in the experiment. Fig 4.17 shows the signal rate and the energy distribution for the coulomb explosion, the signal rate

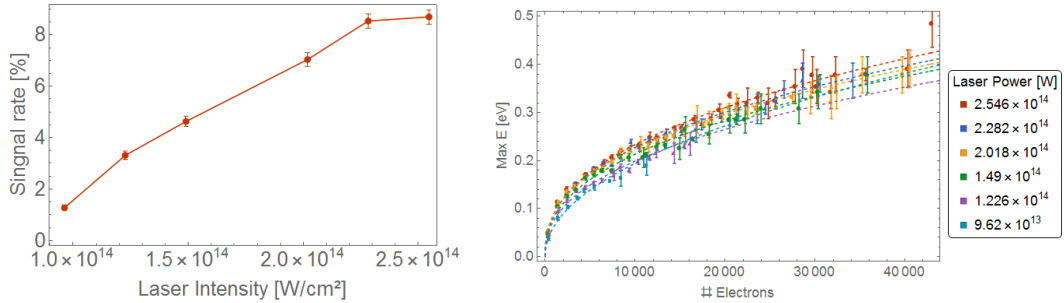


Figure 4.15: On the left, Signal rate for the He-Water laser intensity scan. On the right, the binned energy distribution for the maximum Energy respect to the number of electrons. In colors are the different laser power transformed to focused intensities.

is taken as the percentage of pictures with relevant signal in the data set, once the pictures are identified the radius and internal brightness is find, similar to the results above. Each of the color points in energy distribution plot are the binned data in number of electrons every 1000, the error bars correspond to the standard derivation in the distribution. The points with the lower power, have high error due the signal rate at this intensities is extremely low to have good statistics. The dashed lines are the corresponding fits to each of the intensities taken, the lines for the two lower intensities are not plotted due the low statistics on them. The fitted line was done according to Eq. 3.12 as usual, the fits actually preserve the same tendency where the k factor was keep constant to $2/5$, and the B-coefficient was calculates in order to find the density of the electronic cloud. For example, at the highest power $P=9.5$ W, $B=0.0101$, giving an estimated for the density of $\rho = \mu\text{m}^{-3}$ and a radius of $R = 8\mu\text{m}$. The signal rate shows that the laser intensity plays a fundamental role in the ignition of the process, at lower intensity, less probable to find signal. But at the same time we can identify that after the intensity go up to $2E14\text{W}/\text{cm}^2$ the process starts to keep in a constant rate, that suggest there exist an intensity threshold to overcome so the plasma formation will not be affected by the extra intensity radiated. this could be attribute to the ionization process, As known certain energy need to be transfer to the dopant to ionized, but once the a intensity is reach all dopant will be completely ionized, so there is no need to use powerful beams.

Fig. 4.16 show two plot corresponding to the Mean of energy and number of electrons for each data set at it corresponding intensities and also the histograms with the respectively distributions. On Bottom, the mean values of #e- and E_{max} , shows a disposal similar to the signal rate, the more intense the laser pulse the more energy and electrons can be found. The means values start to rise in a fast way on left but once it reach the 3 best intensities the divergence decrease and changes are

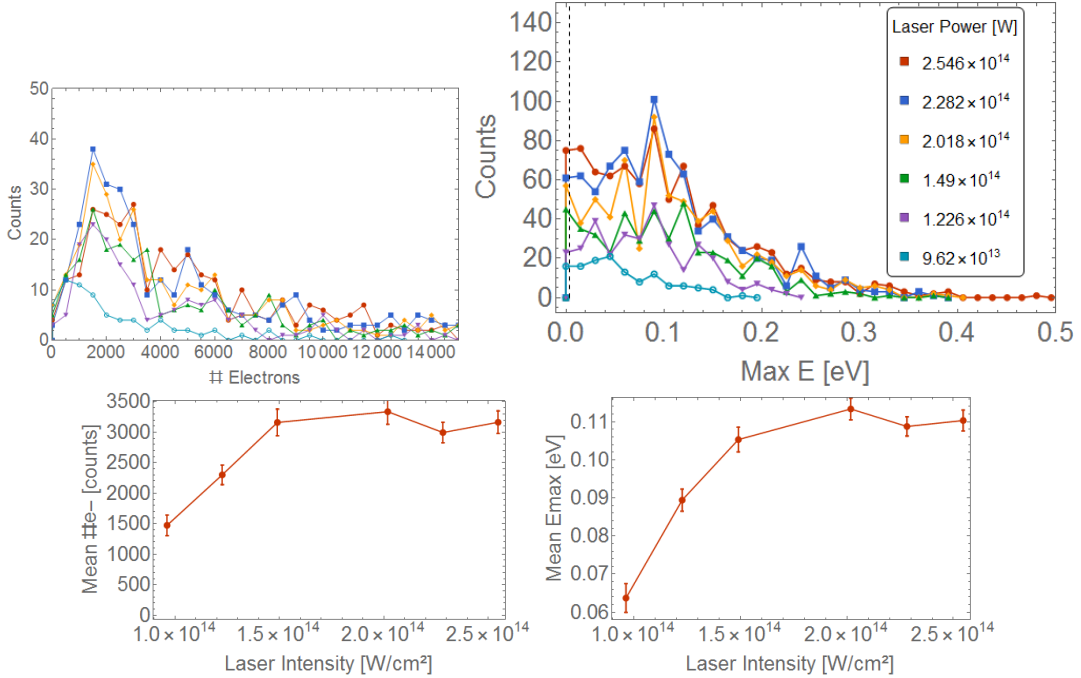


Figure 4.16: On the top, Histograms for number of electro (left) and maximal energy (right) for the difrent pulses. On bottom, The mean $\#e$ - and energyy from the energy distribution for each pulses

less noticeable. On bottom, on the histogram a clear distribution is present. On the bottom left, we can deduce that exist a predominant range of energies, it is clearly mark that for all intensities most of the electrons reach a max energy between $0.1 \rightarrow 0.2$ eV, decreasing the counts drastic after 0.25 eV, it's important to take into account that for the smallest bloop signals, the lower energetic points are not taking into account because the radius finder can't spot signals with less than 6 pixels of radius. Furthermore, on the right histogram, most of the data is distributes in the peak near to 2000e-, having stiff rise from zero to 100 and a slower decrease after 4000e-, the counts for bigger electronic clouds decrease drastic for bigger numbers. A second trend that can be sift is that the peak count decrease with intensities, as shown, although most of the peaks lay close to the same number, the counts, the dark blue line correspond to the higher intensity which have the higher counts, the higher the intensity the higher the counts, until reach the red line and light blue line. This counts depends directly from the signal rate , but in the Mean Values we can spot that the Energies and the number of electrons does shift their distribution to bigger values with the intensities, it means that this high power allowed to reach bigger nanoplasmas that will denote in high energy numbers too.

Pulse duration [fs]	Power[mW]	Laser intensity [W/Cm ²]
65	8.8	1.5E14
120	9.7	8E13
200	9.8	5E13
250	9.2	3.9E13

4.2.5 MIR. Helium Pulse duration dependency

One of the advantage of the laser system in ELI-Alps, is the possibility to change the laser pulse duration. In this data set, we present the result for the energy distribution of helium cluster doped with Xenon under different pulse duration. Helium clusters at the same nozzle temperature $T_{nozzle} = 10.5$ K and backing pressure of $P_0 = 30$ mbar, were doped with Xenon at a fix doping level $P_{dop} = 2.4E - 4$ mbar pressure measured in the gas doping cell. At this nozzle temperature the Helium forms big clusters, with approximated $N = 3150000$ atoms before going through the oven chamber and its doped with $Xe_{dop}=75$ atoms. The VMI voltages where set to VMIx1 and the MCP and PHS to 1600V and 4000V respectively. The camera was stablish to a exposure time of $t_{exp} = 34\mu s$. A first averaged mode signal was taken as a guide to the eye and after 100000 pictures were taken at 4 different pulse duration, at 65, 120, 200 and 250 fs, measured by the ELI-laser personal supporting us in the experiment, using FROG technique. In the beginning of the experiment, we notice that the laser pulse have a dependence with the laser power, longer pulses results in a weaker power. Table ?? resume the laser power obtained for each of the pulse duration. Fortunately the intensities didn't defer much and the intensities obtained are farther that the threshold to start the coulomb explosion as seen in the intensity scan above.

Fig. ?? shows the signal rate and the Binned energy distribution for all the different pulses. As shown, the signal rate have a mark dependence on the pulse duration, showing on left a big signal rate of almost 20% and decreasing constantly until the longer pulses decrease down to 10%. This behavior is suspected because, as already mentioned, even the output power of the laser tends to remain continuous and once we stretch the pulse, the energy gets redistributed, so the laser field interacting in the ionization process is weaker, hence, the coulomb explosion ignition probability decrease. At the same time, on the energy distribution plot an interesting results are exhibited. As usual all point represent the #e- and E_{max} of a single picture and the dashed line is the corresponding fit for each laser pulse following Eq. 3.12, letting the exponent and B-factor variable. In general all plasmas behave in similar way, the fit lines goes almost parallel to each other and display the same B-factor of 0.000179 that leads to a Radius for the electronic cloud of almost 500 μm with a factor of 2/5.

This similarity in the B-factor could represent that the energy distribution actually doesn't seen affected by the laser pulse duration.

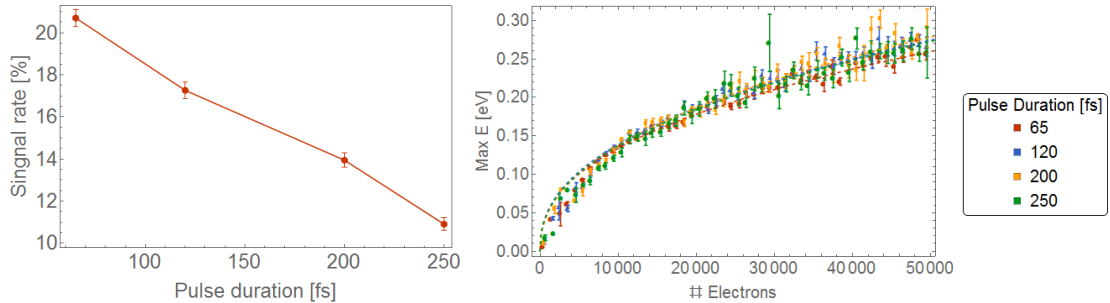


Figure 4.17: On the left, Signal rate for the He-Xe pulse duration scan. On the right, the binned energy distribution for the maximum Energy respect to the number of electrons. In colors are the different pulses and the errors bar is the standard derivation for the binned data every 1000 electrons and the dashes line are the fitted parameters.

In fig 4.18 we show the histograms as well as the Mean number of electrons and E_{max} with dependency on the pulse duration. On top, the histograms shows a clear peak for the shorter duration while in the longest the distribution get broader. It means, that the smaller droplets are easily ignited on the shorter pulses, so we see the peak close to 100000 electrons, and on contrast, the longer pulses are more sensible to coulomb explode the bigger droplets. This also can be seen in the lower figures where the mean values rises with the pulse, in the energy and in the number of electrons. This result is surprising, especially if we compare it with Fig. 4.16, in the Intensity dependence.

As mentioned, the longer the pulse the weaker is its intensity. In fig 4.18 we showed that the mean values in the Intensity scan decrease with the power in contrast to the pulse dependence where the mean values increases negligible the intensity. Although, it is a non-intuitive results, it can be explained if we take into account that for longer pulses we have more cycles in the pulse. In consequence, even the initial ionization probability is lower for the first cycles, the electrons created on them will have more time to interact with the laser field, acquiring more energy and incrementing the electronic cascade that will start the coulomb explosion.

4.2.6 MIR. Helium-Xenon-Calcium doping scan

In this experiment Helium clusters where doped with Xenon and Calcium atoms simultaneously. The Helium clusters were created at the same nozzle temperature $T_{nozzle} = 10.6$ K and a backing pressure of $P_0 = 30$ mbar. Xenon where introduce at 5 different pressures measured in the gas doping cell and Calcium was evaporated

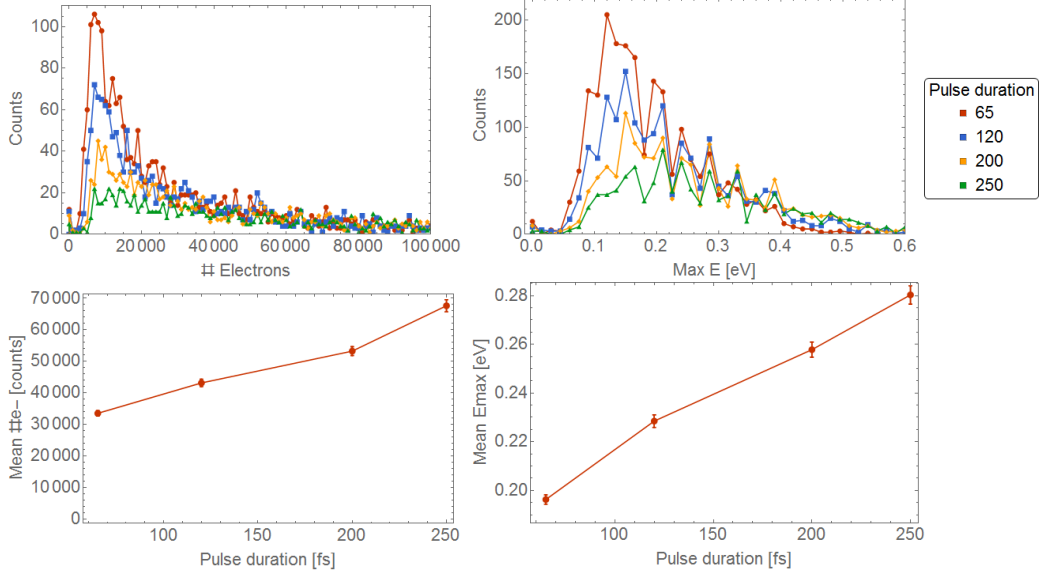


Figure 4.18: On the top, Histograms for number of electro (left) and maximal energy (right) for the different pulses. On bottom, The mean $\#e$ - and energy from the energy distribution for each pulses

Xe_{dop}	0 atoms	30	90	180	350
Ca_{dop}					
5 atoms	241500	239100	234300		
7	239000	236600	231800		
15	226300	223900	219100		
22	213400	211300	207080		
31	195500		189450	182550	172120
45	170700		165150	159700	
62	137000		132050	127322	$\langle N \rangle_{He_{atoms}}$

in the oven at 7 different temperatures. Table ?? shows the sorted parameters used and their associate cluster size. The cells in the index (up and left) represent the number of atom for the Xenon and calcium for each data set while the inner cell shows their correlates mean He cluster size in atoms, The spaces in black are data set that were not taken. The VMI voltages where set to VMIx1 and the MCP and PHS to 1600V and 4000V respectively. The camera was stablish to exposure time of $t_{exp} = 34\mu s$ and single shot was ensure. The laser power where monitored constantly guarantee an average power of 10.7 W at pulses duration around 45 fs.

In Fig ?? we present the binned energy distribution and its respective histograms for $\#e$ - and E_{max} . All the different doping are plotted in the same diagram in order to show that the initial doping doesn't change radically the energy distribution. As usual, the points are the individual pictures bloop analyzed and binned, the dash lines are the fit for the corresponding Eq. 3.12 with variable factor founded on 2/5

and a average B-factor of $B = 0.0048$, leading to electronic cloud radii of $R = 18\mu\text{m}$. In this cases, we will not focus on the energy distribution because as shown, not big difference in the final electronic cloud is present. Further, the histograms we can show that the E_{max} distribution is quite similar for all doping as well. There is a defined peak close to 0.1 eV Boltzmann distribution likewise with a slow slop up to 0.4 eV. Furthermore, the number of electrons present a peak close to 2000 electrons with the slop decreasing up to 8000 where the counts reduce below 10. A second result to take into account, mentioned in the past chapters, is that the histogram share a peak electrons but the counts are reduce because of the signal rate as expected, so the dopant level does not play a big role in all state of the nanoplasma, But as we will see next, it does act in the signal rate and mean values.

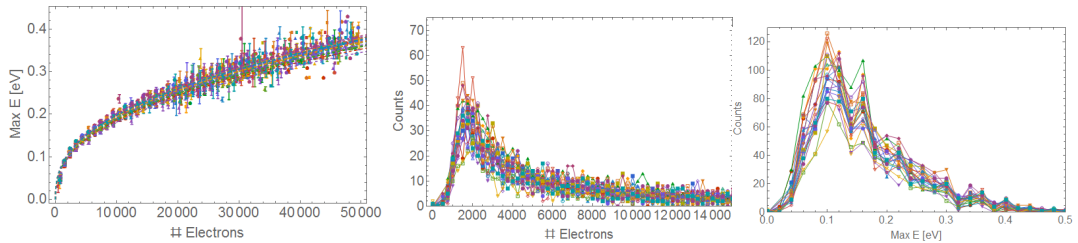


Figure 4.19: On The left, the binned energy distribution in function of the number of electrons for all the different doping levels in Xe and Ca, in color points the binned data and in dashed lines the corresponding fit function. In the center, the histogram for the Number of electrons for all doping levels. On the right, the histogram as well for the Max energies fount for all the doping. The doping have a joined behaviors, the counts derivate a few but is related to the signal rate as shown next.

Fig 4.20 shows an interpolation for the signal rate. The green scale shows the percentage of signal in the data set for each doping level. On bottom the number of Xenon atoms and on left the number of calcium atoms. The white points represent the points where the measurement were done. The data points with higher dopant are also included in the interpolated but not plotted. The dashed color line are cuts at a constant dopant numbers, for different constant Xe+Ca at 40, 50, 65, 85, 100, 120 and 150 atoms. The lines where choose in order that each line lay between 3 data points, so the interpolation could be accurate enough. On the right of fig 4.20, the cuts are plotted depending on the Xe atoms. This means that the right side of each line represent the doping with the maximum Xe atoms at the Xe+Ca constant, once we go from right to left, we replace each Xe atom for one Ca atom until we replace all Xe atom. Each line have a maximum of 40 points, because it was the max Ca doping measured.

An important result can de derive from Fig 4.20, as shown in the cut lines at

constant total doping, we found a increment in the signal as the Ca doping replace the Xe. In all line, from right to left, the signal rate goes up when a few atoms of Ca are added despite the amount of Xe. It demonstrate a better efficiency in the doping for Xe-Ca combination compared to only Xe or only Ca. This tendency can be spot not just on the big crest in the interpolation between 70 to 120 Xe atoms and 15 to 25 Ca atoms, but also in each of the cuts, where the peaks are clearly display and the signal rate increase faster for these extra Ca atoms added, but once we reach a saturation maxima, the extra Ca atoms added makes the signal rate again decrees but in a slower way in most of the cases.

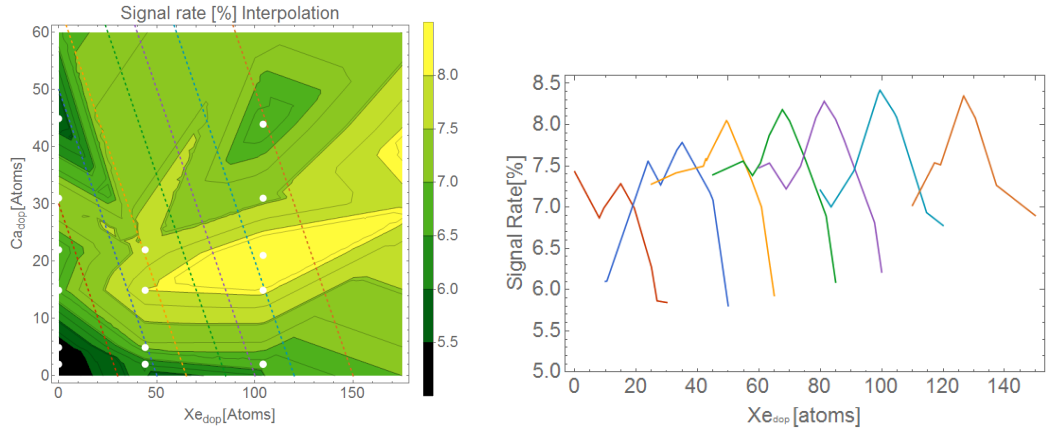


Figure 4.20: Interpolation and Cuts for the Signal Rates at different. The Green graph is the interpolation of all the different doping levels with Xe and Ca. On white points, the actual measurements and in dashes colored lines, the cuts at constant doping level. On the right, the plot of signal rate depending on Xe doping for the corresponding cuts at the same color.

The same interpolation was done for the histograms for the number of electrons and maximum energy, Fig 4.21 and Fig. ?? shows the interpolation and cuts for constant dopant respectively. Fig 4.21 show one clear peak at low doping where the maximum number of electrons appears, then for higher doping the counts starts to decreases and even a small depletion is shown in the range of Xe=100 Ca=20 atoms. On the right, the cut at constant dopant is show, the color from left to right represent the same cut done in the corresponding interpolation, and it's necessary to read it at the same way. Where the right side of each line represents just Xe doping and each number to the left mean replacing one Xe atom for one Ca atom. As show, the exist also a recurrent peak efficiency in the nanoplasma ignition, meaning that at this peak the larger cluster are ionized, similar as shown on the Pulse duration scan.

Equally important. In the E_{max} interpolation, a clear peak is also shown at $Xe =$

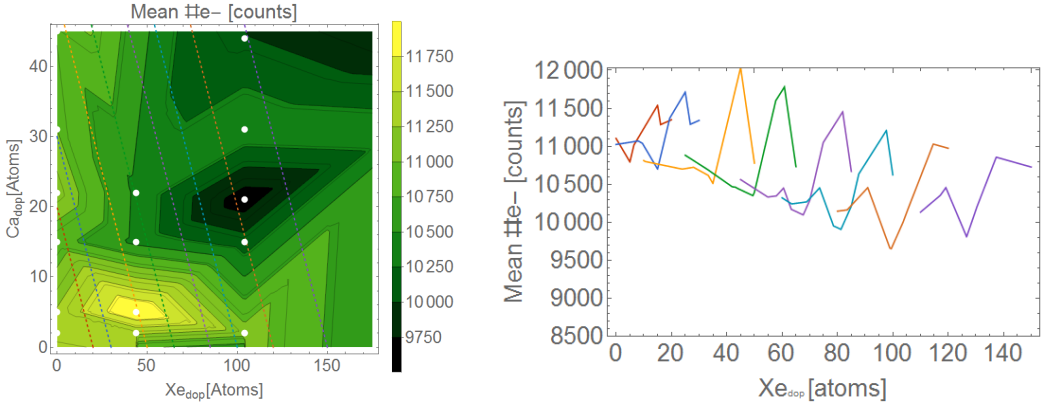


Figure 4.21: Interpolation and Cuts for the Mean values at different doping of the number of electrons. The Green graph is the interpolation of all the different doping with Xe and Ca. On white points, the actual measurements and in dashes colored lines, the cuts at constant doping level. On the right, the plot on Xe doping dependence for the cut with the same color.

50 and Ca=7 atom, where the highest energy is present and a slow drop start for heavier doping. At larger number of dopant the interpolation is less effective due the lack of measurement, so for smaller droplets at heavy doping the cluster starts to deform and deplete it so the nanoplasma explosion is not possible. This can be found in interpolation cuts, where the highly doped lines have a more constant performance and no real change is shown, but once we get close to the optimum doping (Yellow line), the replacement of Xe atom for Ca atoms becomes drastic effective, with a peak founded close to 0.2 eV. This measurement can be compare directly to the water doping scan where we show that once the ignition of the cluster starts, adding more water atoms does not creates changes in the process. Here, Xe doping results in a similar behavior, the points with just Xe atoms (Right edge of each colored line) have a relative constant mean energy, but once we introduce the Ca, dynamics start to appears, given a peak close to the Mean electrons interpolation. For the heavily doped clusters, on the blue, orange and purple cuts in the right, we see that the peaks are not present any more due the cluster destruction when to many atoms are added.

If we compare the three interpolation, in a similar way we have analyzed the histogram in the last sections, we notice that the signal rate have a peak close to Xe=100 and Ca=20, but the Mean number of electrons and energy appears at lower doping. This means that at the most efficient rate, we are not igniting the biggest droplets but on contrary, they are being exploded closer to the zero doping.

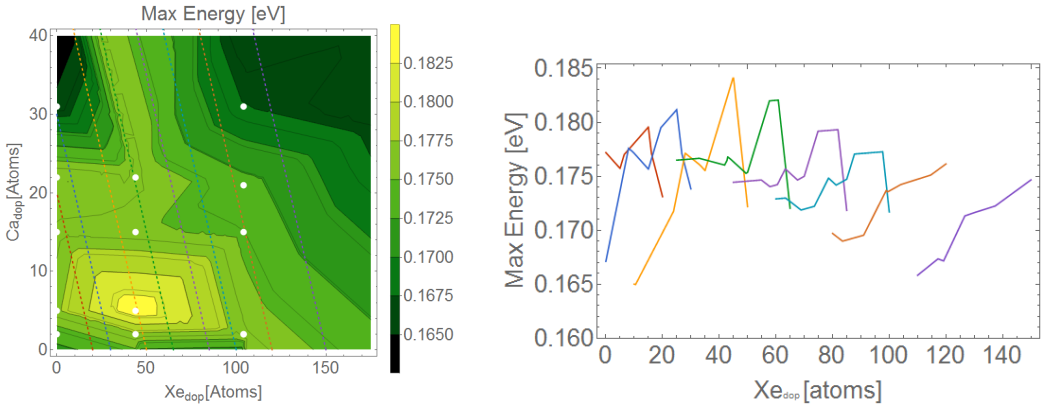


Figure 4.22: Interpolation and Cuts for the Mean values at different doping for the Maximum energy measured. The Green graph is the interpolation of all the different doping with Xe and Ca. On white points, the actual measurements and in dashes colored lines, the cuts at constant doping level. On the right, the plot on Xe doping for the cut with the same color.

4.3 Neon nanoplasma under Mid-Infrared

In the next section we present the results for the second beam time at ELI-Alps where we examines the nanoplasma formation for Neon clusters under Mid-Infrared laser pulses. The laser for this experiment was the same system used in Helium droplets. Neon cluster were created via a supersonic expansion with a conical nozzle with aperture $d=15 \mu\text{m}$ of diameter. In order to obtain different cluster sizes, we used several nozzle temperatures around 37 K to 42 K, with a constant backing pressure of 50 mbar. Neon 0.6 XXX were used to assure the purity of the clusters and to avoid any nozzle clog. Neon was doped with Xenon through the gas doping cell. We will present 3 different experiments; Neon clusters size, Laser Pulse duration scan and Xe doping dependence. The VMI voltages keeps the same rate and the MCP and PHS voltages will be specified in each section. The pressures in the detection chamber oscillated during the experiments around 6E-8 mbar with the chopper open (Cluster beam in).

Neon cluster formation presents a technical challenge due its solidification curve, at this backing pressure, small changes on the nozzle temperature leads to solidification of the gas, so we need to be careful at temperatures lower than 37 K. Another difference between Neon and Helium, is that the Neon clusters after the supersonic expansion are in a solid state. Same as performed with the Helium cluster, we use the Hagen scale to estimate the cluster sizes. Despite the difference and changes in the parameters, we perform the experiments without further problems.

Fig 4.23 show a compilation of the raw VMI signals of Neon plasma. In general

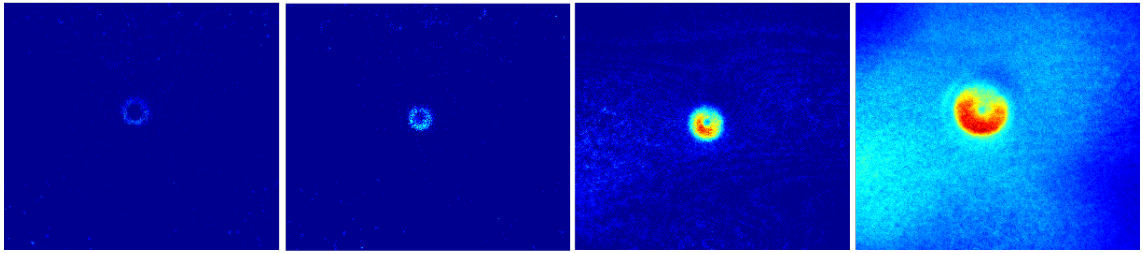


Figure 4.23: Sample signals for the Neon nanoplasma.

all pictures have a similar distributions to the helium clusters. Fig. a and b are the most common signals, with very small bloops and weak intensity, specially at temperatures upper than 39 K. Fig 4.23 c represent a small rate of the images upper 39 K, where the bloops get bigger and higher intensities are present. The anisotropic brightness in the two last samples, are due a blind spot in the upper-center of the phosphorscreen developed because the large amount of signals collected during the days. Fortunately it is a systematic error and for future experiments we will just need to replace the detector. Additionally Fig 4.23 d are the signals for biggest droplets at 37 K, the bloops start to be anisotropic and saturating the camera. Although, this signals was not a significant percentage of the results, they did appear regularly. One explanation for its irregular outline is given if we assume big clusters with irregular shapes, because the Neon clusters are solid, the bigger clusters will not condensate uniformly and in consequence they will create anomalies on the signal. Another explanation could be because of the large density of electron in big nanoplasma, they start to interact and create an unusual signal. Subsequently, this big droplets will be analyzed independently.

4.3.1 MIR. Neon-Xenon doping scan

In this experiment Small Neon clusters where doped with Xenon at different doping levels. The Neon clusters were created at the same nozzle temperature $T_{nozzle} = 39$ K and at a backing pressure of $P_0 = 50$ mbar. Xenon where introduce at 7 different pressures measured in the oven chamber. The VMI voltages were set to VMIx1 and the MCP and PHS to 1700 V and 4000 V respectively. The camera was stablish to an exposure time of $t_{exp} = 34 \mu\text{s}$ and the laser power were set to an average power of 10 W.

Fig 4.24, shows the signal rate for the different pressures and the energy distribution for all doping levels. As notice on the left of the plot, the nanoplasma signal rate increase rapidly with the doping, until the best doping at 5E-5 mbar and keep

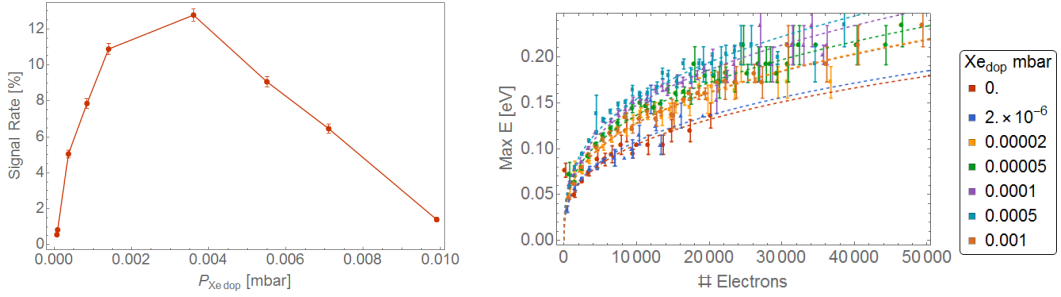


Figure 4.24: On the left, Signal rate for the Ne-Xe doping scan. On the right, the binned energy distribution for the maximum Energy respect to the number of electrons. In colors are the different doping pressures and the errors bar is the standard derivation for the binned data every 1000 electrons and the dashes line are the fitted parameters.

constant for higher doping. This agrees to our previous results showing there exist a minimum doping level to have the most efficient plasma creation, and stronger doping does not help to have more signal. On contrary, for the highest doping levels we denote a small reduction in the signal rate showing that at this level, the clusters starts to be destroyed, and the signal rate goes down. For the Energy distribution, each colored point is the binning of the individual signal transformed to number of electrons and Energy, the dashed lines are the fits to the data according Eq 3.13 with k and B factor set free. As seen in the plot, the fit functions are quite similar to each other, sharing a comparable distribution. Table XXX shows the exponent, B-factor and the corresponding density and radius for the electronic cloud found from the fit. This function agrees perfectly to or spherical cloud model, same as it happened on the NIR experiments. This relation proof that the Islam Model applied to the electron in a nanoplasma explosion could be accurate.

Fig. 4.25 shows the histogram and the mean values for the Max energy and number of electrons. On the top, the histogram show a close distribution with peaks close to 0.1 eV and a drastic decrease up to 0.2 eV, showing as well, the recurrent off value in the min energy required by the plasma that is close to zero but no zero. On the electrons histogram, a broader distribution is shown with a systematic peak at 3000 electrons, it means that the mean signal found, correspond to small clusters, even though massive signals up to 30000 electrons can be found. On one hand, The mean values shows a constant increment in the energy for the first pressures, going in agreement with the signal rate, in other words, adding more dopant to the Neon allows to achieve higher energies, but after reaching the doping limit pressure, a decrease in the mean energy appears. On the other hand, for the mean number of electrons, we see that for the first doping, the mean value keeps quite constants, but once we go upper the 5E-5 mbar, the mean decrease but the signal rate keeps high.

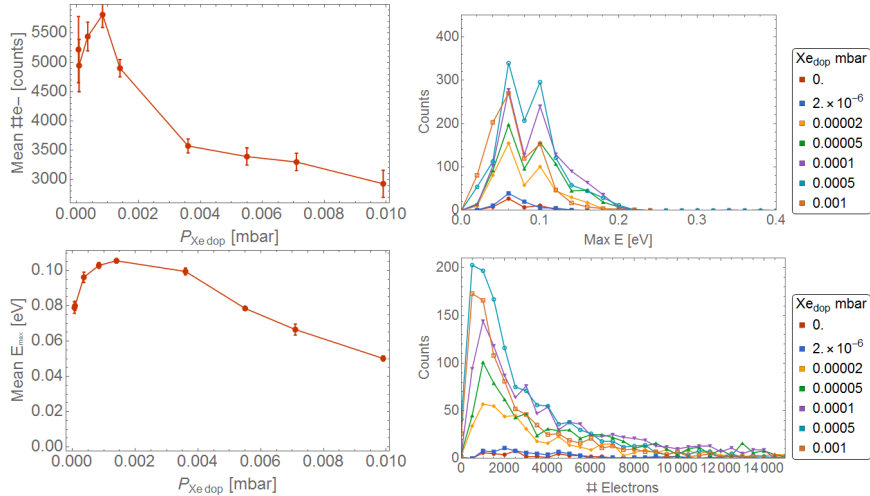


Figure 4.25: On the top, Histograms for number of electro (left) and maximal energy (right) for the different Xenon doping levels. On bottom, the mean $\#e$ - and energy from the energy distribution for each pressure

This results shows that the doping increase the efficiency to ignite the nanoplasma, but at large doping level the mean value of electrons decrease, meaning that we are igniting small droplets. In short, is more efficient to ignite bigger droplets than small ones, because according to the data, the small ones need a larger amount of doping to be ignited while the large cluster just need a few atoms.

4.3.2 MIR. Neon cluster size scan

In order to understand the nano plasma explosion in Neon cluster, this experiment was done on different Neon cluster at a fix doping level with Xenon. The Neon clusters were created at 5 nozzle temperature 39, 40, 41, 42 and 44 K with a backing pressure of $P_0 = 50$ mbar. Xenon where introduce at a fix pressures measured in the doping cell of 0.00036 mbar. The VMI voltages where set to VMIx1 and the MCP and PHS to 1800 V and 4100 V respectively. The camera was stablish to exposure time of $t_{\text{exp}} = 34 \mu\text{s}$ with the single shoot measurement scheme. The laser power were set to an average power of 11 W.

Fig 4.26 shows the signal rate and the energy distribution for the different nozzle temperatures. On the left, the signal rate shows an expected result where the bigger droplets present the higher rates and it decrease with the cluster size (high temperatures). We can compare this result with Fig. 4.5 where it have the same behaviour. The reason for this tendency is not clear, but if we assume the interaction dopant-cluster, small cluster could have a high probability of losing the ionized electrons in the beginning of the pulse, so the ignition process is less efficient, while

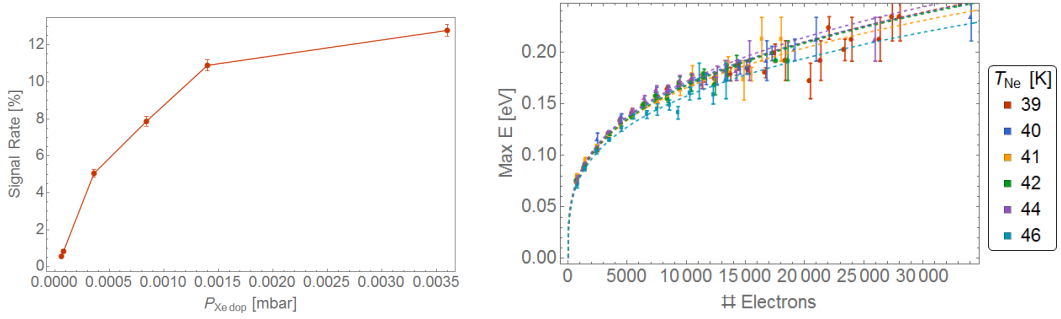


Figure 4.26: On the left, Signal rate for neon at different nozzle temperatures. On the right, the binned energy distribution for the maximum Energy respect to the number of electrons. In colors are the different doping pressures and the errors bar is the standard derivation for the binned data every 1000 electrons and the dashes line are the fitted parameters.

for the bigger clusters, the ionized electron have more atoms to interact, so the losses are less, and in consequence the bigger clusters are more efficient to create the nanoplasma. For the Energy distribution there is no surprise neither, the data point and signal presents the same energy distribution as shown in the doping scan, The fit function was once again done based on Eq. 3.13 and give a exponent of 2/3 following the spherical model. For the B factor, was in average $B = 0.09$ given a density of $62 \mu\text{m}^{-3}$ and a electronic cloud radius of $7 \mu\text{m}$.

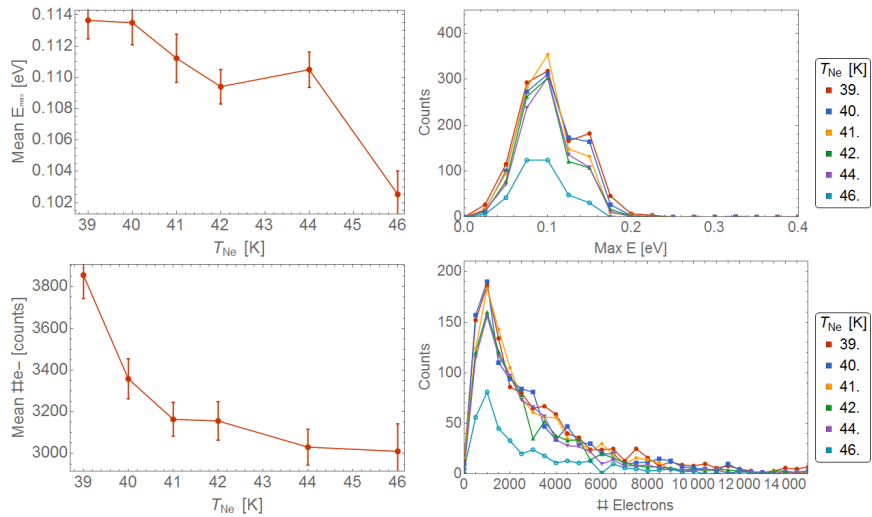


Figure 4.27: On the top, Histograms for number of electro (left) and maximal energy (right) for the different Neon nozzle temperatures. On bottom, The mean #e- and energy from the energy distribution for each pressure

The mean values show in Fig. 4.27 also have a trivial behaviour, congruent to the signal rate, both, mean number of electrons and Max energy, show a decrease with the cluster size. This trend is also present in Fig. 4.6, but for smaller droplets.

Pulse duration [fs]	Power[W]	Laser intensity [W/Cm ²]
48	10.5	2E14
55	11	1.7E14
64	11	1.5E14
71	10.4	1.3E14
94	8.6	1E14

Table 4.4: Neon pulse scan intensity table.

The Histogram on the right, have a clear broaden distribution and it have a smaller off set in the zero again. The energy count present a peak around 0.05 eV and almost none signal is present over 2 eV. Furthermore, The number of electrons have a similar trend with a peak around 3000 electrons, analogous to the histogram in the Xe doping scan.

4.3.3 MIR. Neon pulse scan

The last measurement done in Eli Alps- was a laser pulse duration scan. Neon cluster at a fix doping level with Xenon at a nozzle temperature 39 K and a backing pressure of $P_0 = 50$ mbar were shoot by the MIR laser pulse at 5 different pulse duration of, 48, 55, 64 71, and 94 fs. Xenon where introduce at a fix pressures measured in the doping cell at 0.0002 mbar. The VMI voltages were set to VMIx1 and the MCP and PHS to 1700 V and 4000 V respectively. The camera was stablish to exposure time of 34 μ s with the single shoot measurement scheme. As in section 4.2.5 the pulse duration have a recurrent effect in the laser power, Table 4.4 shows the different powers and consecutive the laser intensities at each data set was taken, as shown all sets are comparable.

Fig. 4.28 present the signal rate and the energy distribution for the different pulse duration. Here the signal rates shows the same tendency that sec 4.2, The pulse duration plays an important role in the nanoplasma ignition, and the probability to create nanoplasma decrease constantly with the pulse, in this case, almost having no signal for pulses longer than 100 fs. The Energy distribution on the other hand, also shows a similitude to the helium results, The Max energy and number of electrons keep a mark distribution around the fit function, the dashed lines correspond to the fit function with a exponent of 2/3 and a B- factor of 0.0004.

Surprisingly in Fig 4.29 the mean values for the electron numbers and energy also shown a strong relation to the pulse duration. As table 4.4 reefers, the intensity that the laser gave were almost the same, so the variations in the mean values confirm that at longer pulses the rates to ionize bigger droplets increase. So as shown, we can

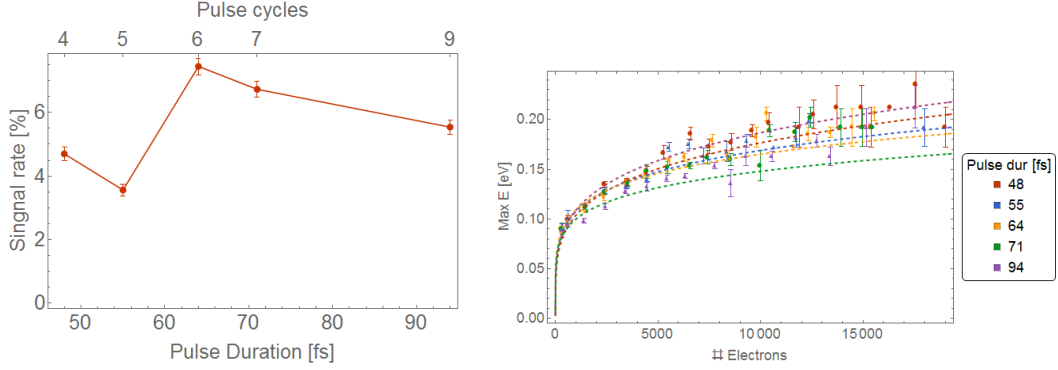


Figure 4.28: On the left, Signal rate for neon at different pulse duration. On the right, the binned energy distribution for the maximum Energy respect to the number of electrons. In colors are the different doping pressures and the errors bar is the standard derivation for the binned data every 1000 electrons and the dashes line are the fitted parameters.

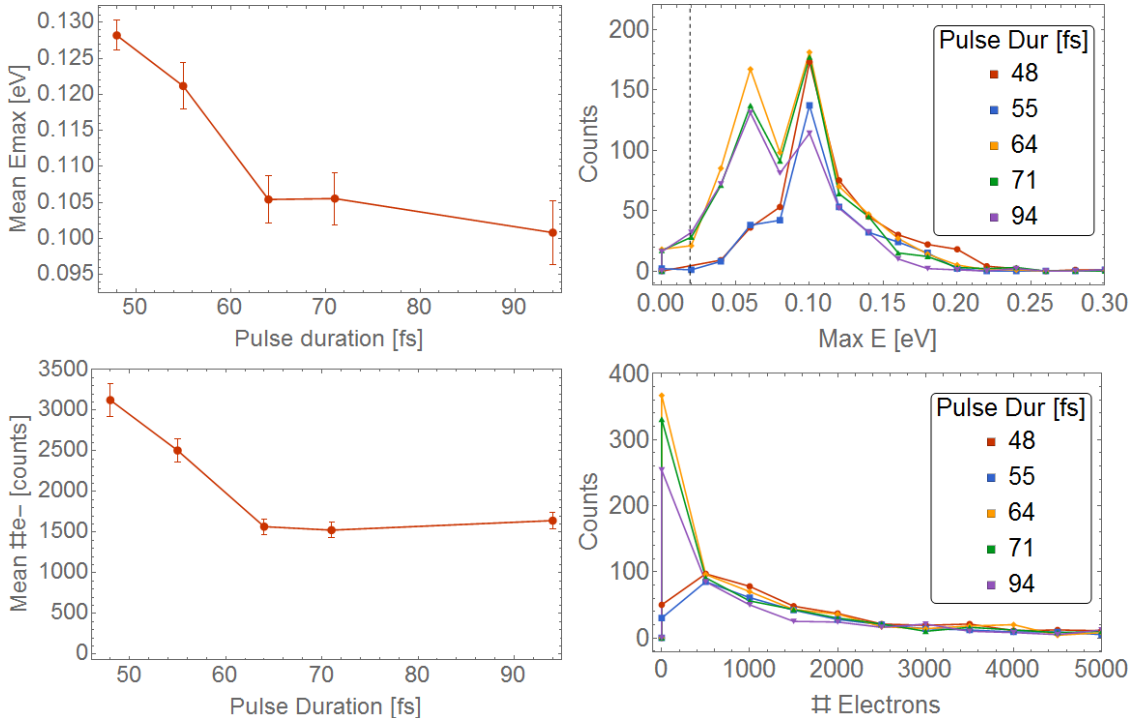


Figure 4.29: MIR Neon pulse duration. On the top, mean values (Left) and Histogram (right) for the max energy. At the Bottom mean values (Left) and Histogram (right) for the number of electrons at different pulse duration.

see the same effect regardless the cluster element and doping level. For understand this result we need to picture how the stretch of a pulse will derive in more cycles in it. The first cycles will be determinant for the Ionization of the dopant, the electrons create in the beginning of the pulse will have more time to interact with the laser field, and in consequence they will acquire more energy and time to interact with

the cluster. Once we stretch the pulse, the electrons produced in this first cycle will see more cycles, and the ionization of the cluster will be more efficient.

List of Figures

1.1	Helium phase diagram	10
1.2	Scheme for a nozzle expansion	11
1.3	Waan der Wall He-He potential	11
1.4	helium isentropic diagram	12
1.5	Phase diagram for Expansion regimens	13
1.6	Expansion droplets Regimens	14
1.7	Helium creation, doping and evaporation sketch	16
1.8	Neon phase-Isentropic diagrams	17
1.9	Relaxation processes for photoionization	20
1.10	Ionization regimes	21
1.11	Ponderomotive 3 steps	24
1.12	Cluster potential regimes	26
1.13	sketch of the Coulomb explosion for a doped cluster due the excitation of a pulsed laser field. At the beginning of the process the laser ionized the droplet, until some femtoseconds (up to 500fs) after, the system collapse and result into a coulomb explosion.	27
1.14	Representation of particle trajectories A, B and C of the ionization volume to the detector plane, which, in spite of initially different velocity the finish on the same point of the detector plane. Withdrawn from [21]	29
1.15	At the top of the graphic some basic functions f_k in different colors, which can be used for the Inverse-Abel transform in the Basex method. On the bottom, the corresponding Abel-transformed functions Fk. Taken from [21]	30
2.1	Sketch of the vacuum chambers, including the main parts of the setup	32
2.2	Cut of the Oven design, including part of the rod and the crucible.	34
2.3	MCP sketch cut	36
2.4	TOF cup	37
3.1	VMI raw images example	40

3.2	Trigger Scheme	41
3.3	Correlation signals example	42
3.4	energy calibration of the VMI spectrometer with SIMION. Electrons with discrete kinetic energy are emitted perpendicular to the spectrometer axis.	43
3.5	(a) Photoelectron image of potassium excited and ionized by linear polarized 404nm light, (b) Abel inverted image and (c) corresponding photoelectron spectrum, not yet calibrated on the energy	44
3.6	Abel inverse transform example	46
3.7	Difference of mean pixel values to determine the radius of the central feature in the VMI images	47
3.8	Fit-Abel transform agreement	48
3.9	Example signal finder	48
3.10	Islam Model fit	51
4.1	He-Xe dop, raw image	53
4.2	Xenon ion charge calibration for NIR	54
4.3	NIR Helium, signal rate and energy distribution	55
4.4	NIR Helium. Histograms for Energy and electrons)	56
4.5	NIR He, Signal rate and Energy Distribution	58
4.6	NIR droplet size scan	59
4.7	MIR TOF spectra He	60
4.8	He-Xe droplet size distribution	61
4.9	He-Xe, signal rate droplet size	62
4.10	MIR He droplet scan histograms	63
4.11	He-Ar Dop distribution	63
4.12	MIR He-Ar doping, signal rate and histograms	64
4.13	He_h2O energydistribution	65
4.14	MIR He-water doping, signal rate and histograms	66
4.15	MIR He intensity scan	67
4.16	MIR He pulse scan. Mean values and Histograms	68
4.17	MIR He pulse scan. Signal rate and Energy distribution	70
4.18	MIR He pulse scan. Mean values and Histograms	71
4.19	MIR He-Xe-Ca doping	72
4.20	MIR He-Xe-Ca doping Signal rate	73
4.21	MIR He-Xe-Ca doping Mean Num Electrons	74
4.22	MIR He-Xe-Ca doping Mean Max energy	75
4.23	MIR Neon raw samples	76

4.24 MIR Ne-Xe doping scan. Signal rate and Energy distribution	77
4.25 MIR Neon Doping scan. Mean values and Histograms	78
4.26 MIR Ne-Xe cluster Size scan. Signal rate and Energy distribution . .	79
4.27 MIR Neon Size scan. Mean values and Histograms	79
4.28 MIR Ne Pulse duration scan. Signal rate and Energy distribution . .	81
4.29 MIR Neon pulse duration. Mean values and Histograms	81

List of Tables

3.1	trigger Channel delays	41
4.1	NIR laser power to intensities	54
4.2	NIR Helium Cluster Size	57
4.3	cluster size reference	61
4.4	Neon pulse scan intensity table.	80

5 Bibliography

- [1] *Helium.* <http://ltl.tkk.fi/research/theory/helium.html>
- [2] BECKER, U. (Hrsg.) ; SHIRLEY, D. A. (Hrsg.): *VUV and Soft X-Ray Photoionization.* <http://dx.doi.org/10.1007/978-1-4613-0315-2>
- [3] A. BETHE, H. ; E. SALPETER, E. : *The Quantum Mechanics of One- and Two-Electron Atoms.* Bd. 35. <http://dx.doi.org/10.1007/978-3-662-12869-5>.
<http://dx.doi.org/10.1007/978-3-662-12869-5>
- [4] ATKINS, K. R.: *Liquid Helium.* Cambridge University Press. – ISBN 978-1-107-63890-7. – Google-Books-ID: gzmNAwAAQBAJ
- [5] AUGST, S. ; MEYERHOFER, D. D. ; STRICKLAND, D. ; CHIN, S. L.: Laser ionization of noble gases by Coulomb-barrier suppression. 8, Nr. 4, 858–867. <http://dx.doi.org/10.1364/JOSAB.8.000858>. – DOI 10.1364/JOSAB.8.000858. – ISSN 1520-8540
- [6] BERKOWITZ, J. : *Photoabsorption, photoionization, and photoelectron spectroscopy.* Academic Press. – ISBN 978-0-12-091650-4. – Google-Books-ID: POeHAAAAIAAJ
- [7] BLANCO, M. ; V. SHEVADE, A. ; A. RYAN, M. : Quantum Mechanics and First-Principles Molecular Dynamics Selection of Polymer Sensing Materials. http://dx.doi.org/10.1007/978-0-387-73715-7_3. – DOI 10.1007/978-0-387-73715-7₃, S.71 – – 92
- [8] BÜNERMANN, O. ; STIENKEMEIER, F. : Modeling the formation of alkali clusters attached to helium nanodroplets and the abundance of high-spin states. 61, Nr. 3, 645–655. <http://dx.doi.org/10.1140/epjd/e2011-10466-0>. – DOI 10.1140/epjd/e2011-10466-0. – ISSN 1434-6079
- [9] BUCHENAU, H. ; KNUTH, E. L. ; NORTHBY, J. ; TOENNIES, J. P. ; WINKLER, C. : Mass spectra and time-of-flight distributions of helium cluster beams. 92, Nr. 11, 6875–6889. <http://dx.doi.org/10.1063/1.458275>. – DOI 10.1063/1.458275. – ISSN 0021-9606, 1089–7690

- [10] CHRISTEN, W. ; RADEMANN, K. ; EVEN, U. : Supersonic Beams at High Particle Densities: Model Description beyond the Ideal Gas Approximation †. 114, Nr. 42, 11189–11201. <http://dx.doi.org/10.1021/jp102855m>. – DOI 10.1021/jp102855m. – ISSN 1089–5639, 1520–5215
- [11] CONNERADE, J. P.: *Highly Excited Atoms*. Cambridge University Press. – ISBN 978–0–521–43232–0. – Google-Books-ID: VgpkXDfkqYEC
- [12] DALY, N. R.: Scintillation Type Mass Spectrometer Ion Detector. 31, Nr. 3, 264–267. <http://dx.doi.org/10.1063/1.1716953>. – DOI 10.1063/1.1716953. – ISSN 0034–6748
- [13] DELFT, D. van ; KES, P. : The discovery of superconductivity. 63, Nr. 9, 38–43. <http://dx.doi.org/10.1063/1.3490499>. – DOI 10.1063/1.3490499. – ISSN 0031–9228
- [14] DELHUIILLE, R. ; MIFFRE, A. ; LAVALLETTE, E. ; BÜCHNER, M. ; RIZZO, C. ; TRÉNEC, G. ; VIGUÉ, J. ; LOESCH, H. J. ; GAUYACQ, J. P.: Optimization of a Langmuir–Taylor detector for lithium. 73, Nr. 6, 2249–2258. <http://dx.doi.org/10.1063/1.1472467>. – DOI 10.1063/1.1472467. – ISSN 0034–6748
- [15] DITMIRE, T. ; DONNELLY, T. ; RUBENCHIK, A. M. ; FALCONE, R. W. ; PERRY, M. D.: Interaction of intense laser pulses with atomic clusters. 53, Nr. 5, 3379–3402. <http://dx.doi.org/10.1103/PhysRevA.53.3379>. – DOI 10.1103/PhysRevA.53.3379
- [16] DRESCHER, M. ; HENTSCHEL, M. ; KIENBERGER, R. ; UBERACKER, M. ; YAKOVLEV, V. ; SCRINZI, A. ; WESTERWALBESLOH, T. ; KLEINEBERG, U. ; HEINZMANN, U. ; KRAUSZ, F. : Time-resolved atomic inner-shell spectroscopy. 419, Nr. 6909, 803. <http://dx.doi.org/10.1038/nature01143>. – DOI 10.1038/nature01143. – ISSN 1476–4687
- [17] EINSTEIN, A. : Über einen die Erzeugung und Verwandlung des Lichtes betreffenden heuristischen Gesichtspunkt. 322, Nr. 6, 132–148. <http://dx.doi.org/10.1002/andp.19053220607>. – DOI 10.1002/andp.19053220607. – ISSN 1521–3889
- [18] ENSS, C. ; HUNKLINGER, S. : *Low-Temperature Physics*. Springer-Verlag //www.springer.com/de/book/9783540231646. – ISBN 978–3–540–23164–6
- [19] EPPINK, A. T. J. B. ; PARKER, D. H.: Velocity map imaging of ions and electrons using electrostatic lenses: Application in photoelectron and photofragment

ion imaging of molecular oxygen. 68, Nr. 9, 3477–3484. <http://dx.doi.org/10.1063/1.1148310>. – DOI 10.1063/1.1148310. – ISSN 0034–6748

- [20] ERK, B. : *Nobel cluster gas expansion driven by a ultra-short high intensity infrared laser*
- [21] FECHNER, L. : *Aufbau eines Velocity-Map-Imaging-Spektrometers und winkelaufgeloste Spektroskopie an Rubidium-dotierten Helium-Nanotropfchen.* http://hacol13.physik.uni-freiburg.de/fp/Versuche/FP2/FP2-21-VMI/Diplomarbeit_Lutz_Fechner.pdf
- [22] FENNEL, T. ; MEIWES-BROER, K.-H. ; TIGGESBÄUMKER, J. ; REINHARD, P.-G. ; DINH, P. M. ; SURAUD, E. : Laser-driven nonlinear cluster dynamics. 82, Nr. 2, 1793–1842. <http://dx.doi.org/10.1103/RevModPhys.82.1793>. – DOI 10.1103/RevModPhys.82.1793
- [23] FERMI, E. : Quantum Theory of Radiation. 4, Nr. 1, 87–132. <http://dx.doi.org/10.1103/RevModPhys.4.87>. – DOI 10.1103/RevModPhys.4.87
- [24] GAVEAU, M.-A. ; BRIANT, M. ; VALLET, V. ; M. MESTDAGH, J. ; P. VISTICOT, J. : Reaction Between Barium and N₂O on Large Neon Clusters. http://dx.doi.org/10.1007/978-3-642-56800-8_57. – DOI 10.1007/978-3-642-56800-8_57. – ISBN 978 – 3 – 642 – 63150 – 4, S.827 – 838
- [25] GOUGH, T. E. ; MENGEL, M. ; ROWNTREE, P. A. ; SCOLES, G. : Infrared spectroscopy at the surface of clusters: SF₆ on Ar. 83, Nr. 10, 4958–4961. <http://dx.doi.org/10.1063/1.449757>. – DOI 10.1063/1.449757. – ISSN 0021–9606
- [26] GREBENEV, S. ; TOENNIES, J. P. ; VILESOV, A. F. : Superfluidity Within a Small Helium-4 Cluster: The Microscopic Andronikashvili Experiment. 279, Nr. 5359, 2083–2086. <http://dx.doi.org/10.1126/science.279.5359.2083>. – DOI 10.1126/science.279.5359.2083. – ISSN 0036–8075, 1095–9203
- [27] GRIFFITHS, D. J.: *Introduction to electrodynamics*. Fourth edition. Pearson. – ISBN 978–0–321–85656–2
- [28] GRÜNER, B. : *Femtosekundenspektroskopie an dotierten Heliumnanotröpfchen: Dissipative Vibrationsdynamik und Charakterisierung eines Nanoplasmas*
- [29] HAGENA, O. F. ; OBERT, W. : Cluster Formation in Expanding Supersonic Jets: Effect of Pressure, Temperature, Nozzle Size, and Test Gas. 56, Nr. 5, 1793–1802.

<http://dx.doi.org/10.1063/1.1677455>. – DOI 10.1063/1.1677455. – ISSN 0021–9606

- [30] HAGENA, O. F. ; OBERT, W. : Cluster Formation in Expanding Supersonic Jets: Effect of Pressure, Temperature, Nozzle Size, and Test Gas. 56, Nr. 5, 1793–1802. <http://dx.doi.org/10.1063/1.1677455>. – DOI 10.1063/1.1677455. – ISSN 0021–9606
- [31] HALPERIN, W. P. ; RASMUSSEN, F. B. ; ARCHIE, C. N. ; RICHARDSON, R. C.: Properties of melting 3He: Specific heat, entropy, latent heat, and temperature. 31, Nr. 5, 617–698. <http://dx.doi.org/10.1007/BF00116046>. – DOI 10.1007/BF00116046. – ISSN 1573–7357
- [32] HARMS, J. ; TOENNIES, J. P. ; DALFOVO, F. : Density of superfluid helium droplets. 58, Nr. 6, 3341–3350. <http://dx.doi.org/10.1103/PhysRevB.58.3341>. – DOI 10.1103/PhysRevB.58.3341
- [33] HAUGHT, A. F. ; POLK, D. H.: Formation and Heating of Laser Irradiated Solid Particle Plasmas. 13, Nr. 11, 2825–2841. <http://dx.doi.org/10.1063/1.1692869>. – DOI 10.1063/1.1692869. – ISSN 0031–9171
- [34] HEIDENREICH, A. ; GRÜNER, B. ; SCHOMAS, D. ; STIENKEMEIER, F. ; KRISHNAN, S. R. ; MUDRICH, M. : Charging dynamics of dopants in helium nanoplasmatics. <http://dx.doi.org/10.1080/09500340.2017.1281454>. – DOI 10.1080/09500340.2017.1281454
- [35] ISLAM, M. R. ; SAALMANN, U. ; ROST, J. M.: Kinetic energy of ions after Coulomb explosion of clusters induced by an intense laser pulse. 73, Nr. 4, 041201. <http://dx.doi.org/10.1103/PhysRevA.73.041201>. – DOI 10.1103/PhysRevA.73.041201
- [36] KAMENEV, A. : Introduction to the Keldysh Formalism.
- [37] KAPITZA, P. : Viscosity of Liquid Helium below the -Point. 141, Nr. 3558, 74. <http://dx.doi.org/10.1038/141074a0>. – DOI 10.1038/141074a0. – ISSN 1476–4687
- [38] KARNAKOV, B. M. ; MUR, V. D. ; POPRUZHENKO, S. V. ; POPOV, V. S.: Strong field ionization by ultrashort laser pulses: Application of the Keldysh theory. 374, Nr. 2, 386–390. <http://dx.doi.org/10.1016/j.physleta.2009.10.058>. – DOI 10.1016/j.physleta.2009.10.058. – ISSN 0375–9601
- [39] KELDYSH, L. V.: Ionization in the field of a strong electromagnetic wave. 20, 1307. <https://ci.nii.ac.jp/naid/10006486551/>

- [40] KNUTH, E. L. ; HENNE, U. : Average size and size distribution of large droplets produced in a free-jet expansion of a liquid. 110, Nr. 5, 2664–2668. <http://dx.doi.org/10.1063/1.477988>. – DOI 10.1063/1.477988. – ISSN 0021–9606, 1089–7690
- [41] KRISHNAN, S. R. ; FECHNER, L. ; KREMER, M. ; SHARMA, V. ; FISCHER, B. ; CAMUS, N. ; JHA, J. ; KRISHNAMURTHY, M. ; PFEIFER, T. ; MOSHAMMER, R. ; ULLRICH, J. ; STIENKEMEIER, F. ; MUDRICH, M. : Ignition of Doped Helium Nanodroplets in Intense Few-Cycle Laser Pulses. In: YAMANOUCHI, K. (Hrsg.) ; KATSUMI, M. (Hrsg.): *Multiphoton Processes and Attosecond Physics*, Springer Berlin Heidelberg (Springer Proceedings in Physics). – ISBN 978–3–642–28948–4, S. 385–390
- [42] KRISHNAN, S. R.: Doped helium nanodroplets in intense few-cycle infrared pulses. http://inis.iaea.org/Search/search.aspx?orig_q=RN:43095633
- [43] LAST, I. ; JORTNER, J. : Quasiresonance ionization of large multicharged clusters in a strong laser field. 60, Nr. 3, 2215–2221. <http://dx.doi.org/10.1103/PhysRevA.60.2215>. – DOI 10.1103/PhysRevA.60.2215
- [44] LEWERENZ, M. ; SCHILLING, B. ; TOENNIES, J. P.: Successive capture and coagulation of atoms and molecules to small clusters in large liquid helium clusters. 102, Nr. 20, 8191–8207. <http://dx.doi.org/10.1063/1.469231>. – DOI 10.1063/1.469231. – ISSN 0021–9606
- [45] LEWIS, W. K. ; HARRUFF-MILLER, B. A. ; LEATHERMAN, P. ; GORD, M. A. ; BUNKER, C. E.: Helium droplet calorimetry of strongly bound species: Carbon clusters from C₂ to C₁₂. 85, Nr. 9, 094102. <http://dx.doi.org/10.1063/1.4895670>. – DOI 10.1063/1.4895670. – ISSN 0034–6748, 1089–7623
- [46] MADISON, K. W. ; PATEL, P. K. ; ALLEN, M. ; PRICE, D. ; FITZPATRICK, R. ; DITMIRE, T. : Role of laser-pulse duration in the neutron yield of deuterium cluster targets. 70, Nr. 5. <http://dx.doi.org/10.1103/PhysRevA.70.053201>. – DOI 10.1103/PhysRevA.70.053201. – ISSN 1050–2947, 1094–1622
- [47] MAINFRAY, G. : MULTIPHOTON IONIZATION OF ATOMS.
- [48] MÖBIUS, E. ; GALVIN, A. B. ; KISTLER, L. M. ; KUCHAREK, H. ; POPECKI, M. A.: Time-of-flight mass spectrographs—From ions to neutral atoms. 121, Nr. 12, 11,647–11,666. <http://dx.doi.org/10.1002/2016JA022553>. – DOI 10.1002/2016JA022553. – ISSN 2169–9402

- [49] MEIJA, J. ; COPLEN, T. B. ; BERGLUND, M. ; BRAND, W. A. ; DE, B. P. ; GRÖNING, M. ; HOLDEN, N. E. ; IRRGEHER, J. ; LOSS, R. D. ; WALCZYK, T. ; PROHASKA, T. : Atomic weights of the elements 2013 (IUPAC Technical Report). 88, Nr. 3, 265–291. <http://dx.doi.org/10.1515/pac-2015-0305>. – DOI 10.1515/pac-2015-0305. – ISSN 0033-4545
- [50] MIKABERIDZE, A. : *Atomic and molecular clusters in intense laser pulses.* https://www.pks.mpg.de/mpi-doc/rostgruppe/dissertation/mikaberidze_dissertation.pdf
- [51] MOUROU, G. A. ; TAJIMA, T. ; BULANOV, S. V.: Optics in the relativistic regime. 78, Nr. 2, 309–371. <http://dx.doi.org/10.1103/RevModPhys.78.309>. – DOI 10.1103/RevModPhys.78.309
- [52] NAUTA, K. ; MILLER, R. E.: Nonequilibrium Self-Assembly of Long Chains of Polar Molecules in Superfluid Helium. 283, Nr. 5409, 1895–1897. <http://dx.doi.org/10.1126/science.283.5409.1895>. – DOI 10.1126/science.283.5409.1895. – ISSN 0036-8075, 1095–9203
- [53] PIETROWSKI, R. von ; RUTZEN, M. ; HAEFTEN, K. von ; KAKAR, S. ; MÖLLER, T. : Fluorescence excitation spectroscopy of Xenon doped Neon clusters: Size and site effects, and cluster melting. 40, S. 22–24. <http://dx.doi.org/10.1007/s004600050149>. – DOI 10.1007/s004600050149
- [54] POPRUZHENKO, S. V.: Keldysh theory of strong field ionization: history, applications, difficulties and perspectives. 47, Nr. 20, 204001. <http://dx.doi.org/10.1088/0953-4075/47/20/204001>. – DOI 10.1088/0953-4075/47/20/204001. – ISSN 0953-4075
- [55] PROTOPAPAS, M. ; KEITEL, C. H. ; KNIGHT, P. L.: Atomic physics with super-high intensity lasers. 60, Nr. 4, 389–486. <http://dx.doi.org/10.1088/0034-4885/60/4/001>. – DOI 10.1088/0034-4885/60/4/001. – ISSN 0034-4885, 1361–6633
- [56] RAFIPOOR, A. J. M.: *Two-Color Photoionization Experiments with Ultrashort Light Pulses on Small Atomic Systems*
- [57] RAY, A. ; SIKDAR, A. K. ; DE, A. : Quasifision timescale: Zeptosecond versus attosecond. 86, 00038. <http://dx.doi.org/10.1051/epjconf/20158600038>. – DOI 10.1051/epjconf/20158600038. – ISSN 2100–014X

- [58] RENDLER, N. : *EINZELSCHUSS ELEKTRONEN-IMAGING VON HELIUM-NANOPLASMEN IN INTENSIVEN NAHINFRAROT LASERFELDERN*
- [59] RHODES, C. K.: Multiphoton Ionization of Atoms. 229, Nr. 4720, 1345–1351. <http://dx.doi.org/10.1126/science.229.4720.1345>. – DOI 10.1126/science.229.4720.1345. – ISSN 0036–8075, 1095–9203
- [60] SAALMANN, U. ; SIEDSCHLAG, C. ; ROST, J. M.: Mechanisms of cluster ionization in strong laser pulses. 39, Nr. 4, R39–R77. <http://dx.doi.org/10.1088/0953-4075/39/4/R01>. – DOI 10.1088/0953–4075/39/4/R01. – ISSN 0953–4075, 1361–6455
- [61] SCHMIDT, V. : *Electron Spectrometry of Atoms using Synchrotron Radiation*. Cambridge University Press. – ISBN 978–0–521–55053–6
- [62] SCHOMAS, D. ; RENDLER, N. ; KRULL, J. ; RICHTER, R. ; MUDRICH, M. : A compact design for velocity-map imaging of energetic electrons and ions. 147, Nr. 1. <http://dx.doi.org/10.1063/1.4984076>. – DOI 10.1063/1.4984076. – ISSN 0021–9606
- [63] STEBBINGS, S. L. ; SÜSSMANN, F. ; YANG, Y.-Y. ; SCRINZI, A. ; DURACH, M. ; RUSINA, A. ; STOCKMAN, M. I. ; KLING, M. F.: Generation of isolated attosecond extreme ultraviolet pulses employing nanoplasmonic field enhancement: optimization of coupled ellipsoids. 13, Nr. 7, 073010. <http://dx.doi.org/10.1088/1367-2630/13/7/073010>. – DOI 10.1088/1367–2630/13/7/073010. – ISSN 1367–2630
- [64] STIENKEMEIER, F. ; LEHMANN, K. K.: Spectroscopy and dynamics in helium nanodroplets. 39, Nr. 8, R127–R166. <http://dx.doi.org/10.1088/0953-4075/39/8/R01>. – DOI 10.1088/0953–4075/39/8/R01. – ISSN 0953–4075, 1361–6455
- [65] STRINGARI, S. ; TREINER, J. : Systematics of liquid helium clusters. 87, Nr. 8, 5021–5027. <http://dx.doi.org/10.1063/1.452818>. – DOI 10.1063/1.452818. – ISSN 0021–9606
- [66] SWENSON, C. A.: The Liquid-Solid Transformation in Helium near Absolute Zero. 79, Nr. 4, 626–631. <http://dx.doi.org/10.1103/PhysRev.79.626>. – DOI 10.1103/PhysRev.79.626
- [67] TCHAPLYGUINE, M. ; LUNDWALL, M. ; GISSELBRECHT, M. ; ÖHRWALL, G. ; EIFEL, R. ; SORENSEN, S. ; SVENSSON, S. ; MÄRTENSSON, N. ; BJÖRNHEOLM, O. : Variable surface composition and radial interface formation in self-assembled free,

- mixed ArXe clusters. 69, Nr. 3, 031201. <http://dx.doi.org/10.1103/PhysRevA.69.031201>. – DOI 10.1103/PhysRevA.69.031201
- [68] THIRÉ, N. ; MAKSIMENKA, R. ; KISS, B. ; FERCHAUD, C. ; GITZINGER, G. ; PINOTEAU, T. ; JOUSSELIN, H. ; JAROSCH, S. ; BIZOUARD, P. ; PIETRO, V. D. ; CORMIER, E. ; OSVAY, K. ; FORGET, N. : Highly stable, 15 W, few-cycle, 65 mrad CEP-noise mid-IR OPCPA for statistical physics. 26, Nr. 21, 26907–26915. <http://dx.doi.org/10.1364/OE.26.026907>. – DOI 10.1364/OE.26.026907. – ISSN 1094-4087
- [69] TOENNIES, J. P. ; VILESOV, A. F.: Spectroscopy of Atoms and Molecules in Liquid Helium. 49, Nr. 1, 1–41. <http://dx.doi.org/10.1146/annurev.physchem.49.1.1>. – DOI 10.1146/annurev.physchem.49.1.1
- [70] TOENNIES, J. P. ; VILESOV, A. F.: Superfluid Helium Droplets: A Uniquely Cold Nanomatrix for Molecules and Molecular Complexes. 43, Nr. 20, 2622–2648. <http://dx.doi.org/10.1002/anie.200300611>. – DOI 10.1002/anie.200300611. – ISSN 1521-3773
- [71] UIBERACKER, M. ; UPHUES, T. ; SCHULTZE, M. ; VERHOEF, A. J. ; YAKOVLEV, V. ; KLING, M. F. ; RAUSCHENBERGER, J. ; KABACHNIK, N. M. ; SCHRÖDER, H. ; LEZIUS, M. ; KOMPA, K. L. ; MULLER, H.-G. ; VRACKING, M. J. J. ; HENDEL, S. ; KLEINEBERG, U. ; HEINZMANN, U. ; DRESCHER, M. ; KRAUSZ, F. : Attosecond real-time observation of electron tunnelling in atoms. 446, Nr. 7136, 627–632. <http://dx.doi.org/10.1038/nature05648>. – DOI 10.1038/nature05648. – ISSN 1476-4687
- [72] WABNITZ, H. ; BITTNER, L. ; CASTRO, A. R. B. ; DÖHRMANN, R. ; GÜRTLER, P. ; LAARMANN, T. ; LAASCH, W. ; SCHULZ, J. ; SWIDERSKI, A. ; HAEFTEN, K. von MÖLLER, T. ; FAATZ, B. ; FATEEV, A. ; FELDHAUS, J. ; GERTH, C. ; HAHN, U. ; SALDIN, E. ; SCHNEIDMILLER, E. ; SYTCHEV, K. ; TIEDTKE, K. ; TREUSCH, R. ; YURKOV, M. : Multiple ionization of atom clusters by intense soft X-rays from a free-electron laser. 420, Nr. 6915, 482–485. <http://dx.doi.org/10.1038/nature01197>. – DOI 10.1038/nature01197. – ISSN 1476–4687
- [73] WEINBERGER, P. : The discovery of thermodynamics. 93, Nr. 20, 2576–2612. <http://dx.doi.org/10.1080/14786435.2013.784402>. – DOI 10.1080/14786435.2013.784402. – ISSN 1478-6435
- [74] WHITTLE, E. ; DOWS, D. A. ; PIMENTEL, G. C.: Matrix Isolation Method for the

Experimental Study of Unstable Species. 22, Nr. 11, 1943–1943. <http://dx.doi.org/10.1063/1.1739957>. – DOI 10.1063/1.1739957. – ISSN 0021–9606, 1089–7690

- [75] WILEY, W. C. ; MCLAREN, I. H.: Time-of-Flight Mass Spectrometer with Improved Resolution. 26, Nr. 12, 1150–1157. <http://dx.doi.org/10.1063/1.1715212>. – DOI 10.1063/1.1715212. – ISSN 0034–6748
- [76] WITUSCHEK, A. ; VANGEROW, J. von ; GRZESIAK, J. ; STIENKEMEIER, F. ; MUDRICH, M. : A simple photoionization scheme for characterizing electron and ion spectrometers. 87, Nr. 8, 083105. <http://dx.doi.org/10.1063/1.4960401>. – DOI 10.1063/1.4960401. – ISSN 0034–6748, 1089–7623
- [77] YOUNG, D. A.: PHASE DIAGRAMS OF THE ELEMENTS.
- [78] ZEWAIL, A. H.: Femtochemistry: Atomic-Scale Dynamics of the Chemical Bond. 104, Nr. 24, 5660–5694. <http://dx.doi.org/10.1021/jp001460h>. – DOI 10.1021/jp001460h. – ISSN 1089–5639
- [79] ZHAO, K. ; ZHANG, Q. ; CHINI, M. ; WU, Y. ; WANG, X. ; CHANG, Z. : Tailoring a 67 attosecond pulse through advantageous phase-mismatch. 37, Nr. 18, 3891–3893. <http://dx.doi.org/10.1364/OL.37.003891>. – DOI 10.1364/OL.37.003891. – ISSN 1539–4794

Danksagung

An dieser Stelle Danke

Erklärung

Ort, Datum

Unterschrift